Slow sub-gap energy states as the origin of hysteresis in perovskite solar cells

Device modeling using Sentaurus

by

Rik van Heerden

to obtain the degree of Master of Science
at the Delft University of Technology,
to be defended publicly on Thursday September 17, 2020 at 14:00.

Student number:	4487826	
Project duration:	December 1, 2019 – September 17, 2020	
Thesis committee:	Dr. O. Isabella,	TU Delft, Associate Professor & Supervisor
	Dr. S.W.H. Eijt,	TU Delft, Assistant Professor & Supervisor
	Dr. ir. T.J. Savenije,	TU Delft, Associate professor
	Prof. dr. M. Zeman,	TU Delft, Professor
	Dr. P.A. Procel Moya,	TU Delft, Postdoc & Daily supervisor

An electronic version of this thesis is available at http://repository.tudelft.nl/.

TU Delft

Preface

This thesis projects marks the end of my time as a master student Applied Physics. I would like to thank my daily supervisor Dr. Paul Procel Moya for his guidance during my thesis project, all the fruitful discussions we had and his availability at any time to answer my questions. Further, I want to thank Dr. Olindo Isabella for giving me the opportunity to carry out this interesting research on perovskite solar cells under his supervision. I also want to thank Dr. Stephan Eijt for his guidance during the start of this project. Finally, I want to thank Dr. ir. Tom Savenije, Prof. dr. Miro Zeman for forming part of my examination committee.

Rik van Heerden
Delft, September 2020

Abstract

Solar cells can play a key role in the transition towards a sustainable future. This transition is one of the major challenges our society faces during the coming decades. Development of high-efficiency photovoltaic solutions at reasonable costs will help accelerating the transformation of our energy system. In this respect, perovskite solar cells are very promising due to their outstanding opto-electronical properties and low-cost fabrication. Obtaining a complete understanding of the device physics and charge transfer mechanisms inside perovskites is crucial for further device improvements.

This thesis focuses on the notorious hysteresis in the current-voltage characteristics of perovskite solar cells. So far, this remarkable phenomenon has usually been explained using ion migration, despite the lack of clear experimental evidence. We implement a simulation platform of perovskite solar cells to analyse the charge transfer mechanisms among energy states including those with energy within the forbidden bandgap. We evaluate transient behaviour and identify the limiting physical mechanisms.

To explain anomalous hysteresis in perovskite solar cells we use a novel approach in which charge accumulates near the material interfaces due to defects with relatively low capture cross-sections. Defects in lead halide perovskites create shallow sub-gap energy states, that act as charge carrier traps. Near the interfaces, this leads to accumulation of trapped charge carriers, effectively screening the electric field inside the perovskite layer. This reduces the device performance. A slow release of trapped charge due to low capture cross-sections results in hysteresis in the current-voltage curve at commonly used scan rates.

TCAD Sentaurus is used as a platform to simulate J-V scans of a planar non-inverted architecture based on the archetypal perovskite $MAPbI_3$, with TiO_2 as electron transport layer and spiro-OMeTAD as hole transport layer. This thesis presents a systematic study of different trap distributions, both in the spatial and energetic domain. The capture cross-sections, densities, energy levels and locations of traps are varied and also the effect of scan rate is analysed. This work analyses both tail state defects and deep defects, based on reported values in literature.

It is found that defects near the ETL/perovskite interface potentially cause anomalous hysteresis in the current-voltage curve. These defects have their transition energy around 0.25 eV and are possibly attributed to iodine interstitials.

Acronyms

CBE conduction band edge.
CPD contact potential difference.

DFT density-functional theory.
DLCP drive-level capacitance profiling.
DLTS deep level transient spectroscopy.
DOS density of states.
DSSC dye-sensitized solar cells.

EPBT energy payback time.
ETL electron transport layer.
ETM electron transport material.

HI Hysteresis Index.
HTL hole transport layer.
HTM hole transport material.

PCE power conversion efficiency.
PL photoluminescence.
PSC perovskite solar cell.
PV photovoltaic.

SCLS space-charge limited current.
SRH Shockley-Read-Hall.

TAS thermal admittance spectroscopy.
TCAD Technology Computer-Aided Design.
TCO transparent conductive oxide.
TMM transfer-matrix method.
TSC thermally stimulated current.

VBE valence band edge.

Contents

1 Introduction

The sun provides us with more than enough energy to meet the world's energy needs. It is the most important source of renewable energy. Turning solar energy into electricity in an efficient and cost-effective way will therefore be among the many interesting challenges we face in the energy transition. In this thesis we study the physics behind metal halide perovskites, a promising class of materials for solar cell application because of their outstanding opto-electronic properties. They are characterised by their low-cost and easy fabrication, high absorption coefficient, long carrier diffusion length and low non-radiative carrier recombination [1, 2]. Also the bandgap can be tuned from the near-infrared to the visible region of the electromagnetic spectrum by changing its compounds [3]. This makes them very suitable for use in multi-junction devices.

The goal of this thesis is to obtain a better understanding of the charge transfer mechanisms inside metal halide perovskites. Development of perovskite solar has rapidly evolved during the last years. The first cells were unstable and had low efficiencies, yet the current record cell has an efficiency exceeding 25 % [4]. The material properties of perovskites offer advantages to simplify the manufacture of high-performance devices such as flexible, transparent or all-perovskite tandem cell modules; also integration of perovskite cells in tandem cells with silicon and CIGS modules appears very promising [1]. It is most likely that there will be multiple attempts to commercialize perovskite photovoltaics (PVs) during the coming years [5]. Nevertheless, material improvements in terms of high efficiency and stability are essential before the commercialization of perovskite solar cells.

It is crucial to fully understand the charge transfer mechanisms inside perovskites and their interaction with the electrodes. Similar to other solar cell materials, simulation tools play an important role in understanding the inner physics and finding critical mechanisms to the conversion energy performance of solar cells. Perovskite solar cell (PSC)s are notorious for their hysteresis in the current-voltage curves. The exact mechanism of the effect is not completely understood yet. Using the comprehensive semiconductor modeling software Sentaurus, we develop a novel approach based on crystal defects to study the effect.

1.1. Brief history of solar cells

The working principle of solar cells is based on the photovoltaic (PV) effect, which is the generation of a potential difference upon illumination of a material. This effect was first demonstrated by Becquerel in 1839 [6]. It took more than 40 years until Charles Fritts invented the first working solar cell in 1883. His device consisted of selenium, coated with a thin layer of gold, and had a very low efficiency. The photovoltaic effect is closely related to the photoelectric effect: electrons can be emitted from a metal or semiconductor when light shines on the material. In 1905 Albert Einstein was the first one to explain this effect [7]. Instead of using the wave theory of light, he described light as composed of discrete wave packets (quanta) with an energy $E = h\nu$ where h is Planck's constant and ν is the frequency of the light. In 1921 Einstein won the Nobel prize for his theories explaining the photoelectric effect.

In 1918 Jan Czochralski invented a new method used for growing high quality crystals, known as the Czochralski process [8]. His technique is still very important for the production of high quality silicon solar cells. The development of practical silicon solar cell itself took a big leap in 1954 from the work of

Bell Labs. Daryl Chapin, Calvin Fuller, and Gerald Pearson created the first solar cell with an efficiency of 6 %, enough to power small everyday live equipment [9].

From the middle of the twentieth century, when people started using solar energy as an alternative energy source for space applications, solar cells have experienced rapid developments. Because of the rising oil prices during the oil crisis in the 1970s, demand for terrestrial solar power increased as well. In the late 1970s and 1980s many companies started to develop PV modules and systems [6]. In 1980 the first thin film solar cell exceeding 10 % efficiency was developed and in 1985 crystalline silicon solar cells were created with efficiencies over 20 %. The first megawatt PV power plant was built in 1982 in Hesperia, California [10]. In 1991 the first high-efficiency dye-sensitized solar cell was developed with an efficiency of 7.1 % [11]. It took until 2006 before the first perovskite solar cell was developed, emerging from the field of dye-sensitized solar cells.

The demand of solar cells has also been stimulated over the years by a strong reduction of the production costs [12]. Figure 1.1 shows the so called price learning curve of photovoltaics by technology. According to Swanson's law a doubling of cumulative production goes with an approximate cost reduction of 20 % [13]. From the fitted lines in Figure 1.1 we see that the learning rate over the past 10 to 15 years is even higher for both crystalline and thin film technology with a price drop of over 30 % for every doubling of the cumulative production.

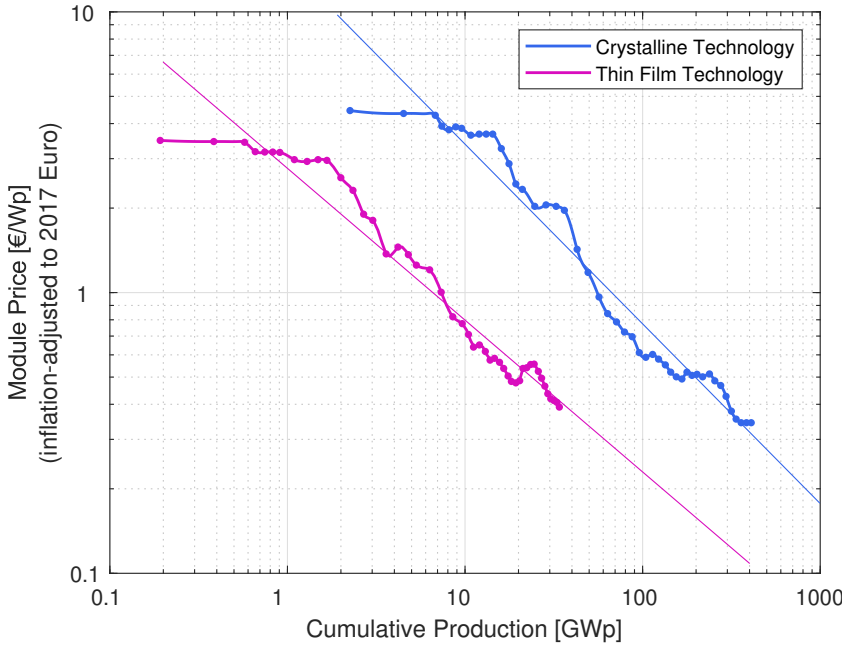

Figure 1.1: Learning curve (or experience curve) for photovoltaic technology. Each data point shows the module price and estimated cumulative production in a quarter of a year, from Q1 2006 up to Q4 2017. Data obtained from Fraunhofer ISE [12].

Currently the PV market is dominated by silicon-wafer based technology, that accounted for about 95 % of the total production in 2017 [12]. Thin-film technologies based on CdTe, CIGS and a-Si accounted for the remaining market share.

1.2. Solar cell characterization

The performance of solar cells can be characterized using I-V (or J-V) measurements. For perovskite solar cells this is done by sweeping the voltage over a fixed voltage range, consecutively in the backward direction (from high to low voltage) and the forward direction (from low to high voltage) [14]. We call these scans the *reverse scan* and *forward scan* respectively.

Figure 1.2 illustrates how the external parameters can be determined from the I-V characteristic of an illuminated cell. The short circuit current I_{sc} is the current that flows when the electrodes of the cell are short circuited ($V = 0$). The open circuit voltage V_{oc} is the voltage at which no current flows ($I = 0$). The fill factor (FF) is the ratio between the maximum power that can be generated with the solar cell and the product $V_{oc}I_{sc}$ (see Figure 1.2).

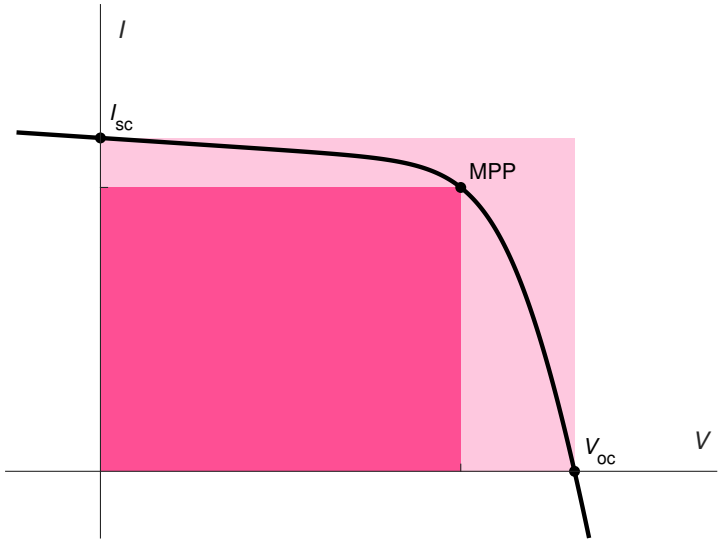

Figure 1.2: An example I-V curve to illustrate the meaning of the output parameters. The operational point at which the maximum power is generated is indicated with 'MPP' (maximum power point). The fill factor equals the ratio between the darker and lighter shaded areas.

1.2.1. Power conversion efficiency

Ideally one would like to convert all electromagnetic energy of the illuminating sunlight to electrical energy. This is not possible, because a fraction of the light is not absorbed (optical losses) and inside the device energy is lost as heat. The power conversion efficiency (PCE) is used as a measure of the performance of a solar cell and is defined as the ratio of power output (electricity) to power input (sunlight). Figure 1.3 shows the rapid development of efficiencies for different solar cell technologies, including perovskite cells. For reference, the ultimate efficiency of an ideal single p-n junction solar cell is 33.1 % for the AM1.5 spectrum (a standard spectrum at the Earth's surface) [15]. This is known as the Shockley-Queisser limit [16]. Higher efficiencies can be achieved with novel techniques like multi-junction solar cells and spectral conversion [6].

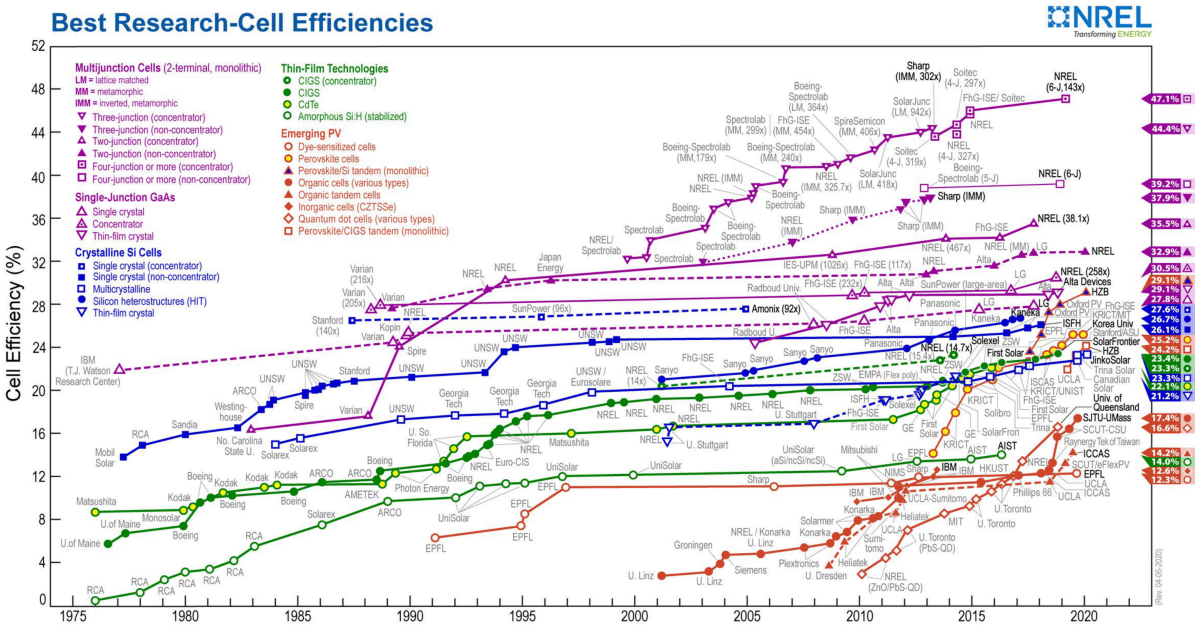

Figure 1.3: Chart of the highest confirmed conversion efficiencies for research cells for different photovoltaic technologies. Adapted from NREL [4].

1.3. Sustainable development

Energy has always played an important role in the fulfillment of human needs. In modern society, electrical energy is essential for heating, lighting, preparation of food and many more. A lot of devices depend on it. According to the IEA World Energy Outlook the total energy demand rises 1 % per year until 2040 and electricity demand will rise even faster [17]. But growing demand is not the only problem. We are at the start of the energy transition: a transformation of the present energy system, that is based on fossil fuels, into one based on renewable energy sources. Nowadays most of the world's energy is produced by burning oil, natural gas and coal. About 80 % of the total primary energy supply are fossil fuels [18]. We deplete these resources much faster than they can be generated by nature and eventually we will need alternative energy sources [19]. Another problem of the current system is related to the emission of greenhouse gas CO_2 by burning fossil fuels. A vast majority of climate-scientists agree that global warming trends are extremely likely to be caused by greenhouse gas emissions from human activities [20].

In a broader sense the energy transition is part of a move towards increased sustainability. The most frequently used definition of sustainable development is adopted from the 1987 Brundtland Report:

Sustainable development is development that meets the needs of the present without compromising the ability of future generations to meet their own needs.

Developing new renewable energy solutions and improving existing solutions is an important step in establishing a sustainable society. Solar energy is a very important inexhaustible source of renewable energy and is available almost everywhere. In their latest 5-year forecast the International Energy Agency (IEA) states that renewable power capacity will expand by 1200 GW, which is a growth of 50% [18]. Solar PV accounts for almost 60 % of this growth, which emphasizes the importance of the technology. In the main scenario of this forecast the total solar PV capacity reaches almost 1.2 TW in 2024. Faster cost reductions and supportive government policies could result in an even more optimistic forecast. As the world's population is expected to continue growing till the end of the current century to 11 billion people [21], the need for efficient use of space is also growing. Developing new photovoltaic materials with low production costs and high efficiencies, like perovskites, will be important to realize the transition towards a sustainable energy system.

1.4. Perovskite solar cells

To understand the working principles and issues of perovskite solar cells (PSCs), some basic knowledge about its structure is required. Here we briefly cover the most important aspects. Subsequently, the obstacles to commercialization of these solar cells are briefly discussed. Finally, we discuss how perovskite solar cells are constructed and mention some of the most popular materials that are used.

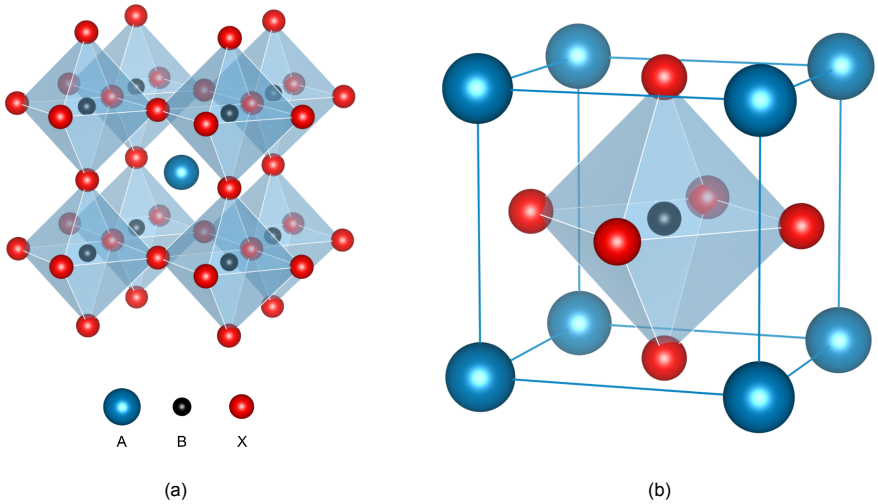

Figure 1.4: Schematic representations of the crystal structure of a perovskite crystal with the cations A and B and anion X indicated. Sketch (a) shows the structure of a cubic perovskite and (b) shows a cubic unit cell. In many perovskites the symmetry is lower, giving tetragonal or orthorombic structures.

Perovskites are materials with an orthorhombic crystal structure identical to the classical mineral calcium titanate ($CaTiO_3$) (see Figure 1.4). They are named after the Russian mineralogist Lev A. Perovski. Any perovskite follows the general chemical formula ABX_3, where A and B are cations of different size and X is an anion. Cation A is the larger one of the two cations and for solar cell applications it is typically organic. Methylammonium ($CH_3NH_3^+$) and formamidinium ($CH(NH_2)_2^+$), abbreviated as MA and FA respectively, are frequently used. Also inorganic elements can be used as cation A, like caesium (Cs) and rubidium (Rb). Cation B is usually lead (Pb) and the X anion is a halide: iodine (I), bromine (Br) or chlorine (Cl). The most widely studied compound is methylammonium lead iodide. It is often abbreviated to $MAPbI_3$ or just MAPI.

Perovskite-based solar cells have substantially developed since Kojima et al. reported the first working cell in 2006 [22]. This cell was based on dye-sensitized solar cells (DSSC) and had an efficiency of 2.2 %. A dye-sensitized solar cell, also known as a Grätzel cell, is a photoelectrochemical system that contains titanium dioxide (TiO_2) nanoparticles, organic dye particles, an electrolyte and platinum contacts. The dye particles (dye sensitizer) act as light absorbers and are mixed with the TiO_2 nanoparticles. When a photon is absorbed by the sensitizer, an electron is excited from the ground state to an exited state. The excited electron is then injected to the conduction band of the TiO_2 nanoparticles and diffuses through the TiO_2 to the transparent conductive oxide (TCO) back contact. Finally it will reach the front contact via the external electric circuit. An electrolyte between the front contact and the dye completes the circuit. The first perovskite-sensitized TiO_2 solar cells from Kojima et al. used $CH_3NH_3PbBr_3$ as a sensitizer with a liquid electrolyte. In 2009 they reported $CH_3NH_3PbI_3$ cells with an even higher efficiency of 3.8 % [23]. Efficiencies have increased rapidly ever since (see Figure 1.3).

1.4.1. Device architectures

Perovskite compounds are used in two types of solar cells: thin-film solar cells and multi-junction solar cells. In thin-film perovskite solar cells the perovskite compound is used as the only absorber layer. Multi-junction solar cells (or tandem cells) consist of multiple absorber materials, so that the solar-spectrum can be utilized more efficiently [6]. This thesis focuses on thin-film perovskite solar cells only.

A typical perovskite solar cell consists of a perovskite absorption layer, enclosed between two charge transport buffer layers, an electron transport layer (ETL) and a hole transport layer (HTL). The perovskite layer is usually between 100 and 500 nm thick; the optimal thickness is a compromise between maximum absorption and efficient carrier extraction. The transport layers have two functions: tuning energy alignment through the device and protecting the perovskite against humidity and oxygen. The right energy alignment is essential for charge carrier separation, about which a more detailed description can be found in chapter 2.

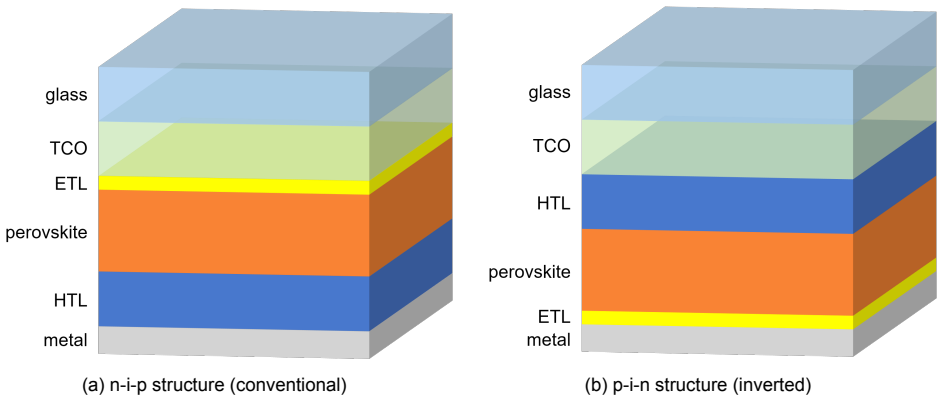

(a) n-i-p structure (conventional) (b) p-i-n structure (inverted)

Figure 1.5: Device architecture of a conventional and inverted device. The relative thickness of the layers shown here are typical, although there is much variation among different architectures.

There are two distinct PSC designs, namely conventional (n-i-p) and inverted (p-i-n) structures. The abbreviations n-i-p and p-i-n refer to the order in which the p-type (HTM), intrinsic (perovskite) and n-type (ETM) layers are deposited. Figure 1.5 shows a schematic representation of both structures. Scientific groups are still exploring different configurations and there is no clear advantage yet of one over the other [24].

Furthermore, planar and mesoscopic/mesoporous structures can be distinguished. Mesoscopic designs contain a mesoporous medium (usually TiO_2) that interpenetrates the perovskite film, in contrast to planar structures that consist of clearly separated layers. The purpose of a mesoporous layer is to enhance carrier extraction by reducing the distance that electrons have to travel to reach the transport layer. The structural design of perovskite solar cell has evolved rapidly over the years, from a dye-sensitized cell to mesoscopic designs and finally planar designs. Nowadays both mesoscopic and planar designs are being used.

1.4.2. Charge transfer mechanisms

Figure 1.6 shows a simplified band diagram of a perovskite solar cell. A band diagram shows the key electron energy levels inside the device (see also Neamen [25]). When a photon is absorbed in the perovskite layer, its energy is used to excite an electron from the valence band to the conduction band. Electrons and holes[1] are separated by the built-in electric field and flow in opposite directions. They are extracted from the perovskite layer into the ETL and HTL respectively and eventually collected at the terminals. The resulting current can deliver power to a load.

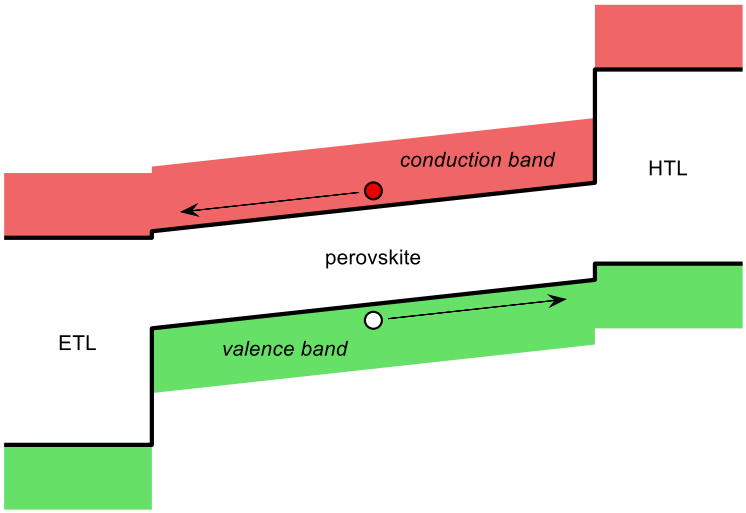

Figure 1.6: Simplified band diagram of a perovskite solar cell in thermal equilibrium.

Motion of carriers that is caused by an electric field is called drift. This is not the only process that can induce a current in the semiconductor. Carriers also flow on average from regions where the carrier density is high to regions of low concentration. This process is called diffusion. Drift and diffusion compete with recombination (processes by which an electron loses energy, see chapter 2) in the bulk material and recombination of charge carriers at the interfaces between the different layers. Next to this, defect states in the bandgap play an important role in semiconductor devices. Such electronic states affect recombination and the absorption characteristics (see section 2.3 and 2.5). The accumulation of charge in defects also has an impact on the electric field inside the semiconductor material. The latter is very important in our model for hysteresis, as we will seen in section 4.1.

[1] The concept of holes is discussed in section 2.1.2.

In the last century there was a lot of interest in research about charge transfer mechanisms of semiconductors, because of the rapid emergence of new semiconductor technologies. This is reflected in the number of papers about semiconductors: more than 250,000 have been published in the past 40 years [26]. Most studies were devoted to silicon, but under certain assumptions the same physical description applies to other semiconductor materials (like perovskite) as well. However, there is still debate about the charge transfer mechanisms that describe its characteristics [27–30].

1.4.3. Transport layers

A good electron transport layer has a high electron mobility and well matched conduction band edge energies with the perovskite layer (see also Figure 1.6). It should act as a barrier for holes, while electrons can easily go through. Similarly, a hole transport layer needs to block electrons and let holes through, so a high hole mobility and well matched valence band edge energies with the perovskite layer are required. Both layers can not only improve the power conversion efficiency, but also enhance the device stability [2]. Typical thicknesses for the ETL lie between 20 and 50 nm. The HTL typically has a thickness between 30 and 200 nm.

Both inorganic and organic materials can be used for the carrier selective transport layers. Mesoporous designs use metal oxides such as TiO_2, Al_2O_3 or ZrO_2 as electron transport material. Metal oxides can be used for planar configurations as well by depositing them in compact form. Organic materials like C_{60} and its derivatives (e.g. $PC_{61}BM$, $PC_{71}BM$, ICBA) are also commonly used as electron transport materials (ETMs) [2]. Popular inorganic hole transport materials (HTMs) are copper iodide (CuI), copper thiocyanate (CuSCN), nickel oxide (NiO_x), vanadium pentoxide (V_2O_5), molybdenum oxide (MoO_3) and tungsten trioxide (WO_3) [2]. Widely used organic HTMs, with which high efficiencies were achieved, are Spiro-OMeTAD, P3HT, PEDOT:PSS and PTAA [2].

A metal contact on the back and a TCO layer on the front complete the device. The metal contact is either made of gold (Au), silver (Ag) or aluminium (Al) [2]. Also carbon electrodes are considered a good candidate [31]. The TCO layer must be a good conductor and transmit light very well. Indium-doped tin oxide (ITO) and fluorine-doped tin oxide (FTO) are frequently used as TCO and in some cases aluminium-doped zinc oxide (AZO) is used [2]. The metal contact is usually between 50 and 100 nm thick. The optimal thickness of the TCO is a trade-off between efficient light transmission and low sheet resistance and also depends on the material itself. It is usually between 50 nm and a few hundred nanometers thick, depending on which material is used and the doping concentration.

1.4.4. Processing techniques

Deposition of the perovskite films is done by means of solution processing and/or vacuum deposition [2]. Spin-coating is one of the most common solution processing methods. In spin-coating, a precursor solution is applied on the center of the substrate, which is then rotated at a high speed to spread the solution. This is followed by annealing the samples at 90 °C. In vacuum deposition the precursors are deposited as a vapour in a vacuum atmosphere.

In the near future, scalable deposition techniques are required for mass production of large-area perovskite solar cells. Preferred methods are tape casting, screen printing, inkjet printing, slot-die coating [32].

1.4.5. Issues

The main obstacle to commercialization of perovskite solar cell is that they generally undergo (rapid) degradation on exposure to moisture and ultraviolet radiation [33, 34]. Depending on their composition, also thermal degradation and exposure to oxygen can be an issue. Better results are achieved using mixed cation and mixed halide perovskites. For instance $FA_{0.83}Cs_{0.17}Pb(I_{0.6}Br_{0.4})_3$ and $FA_{0.9}Cs_{0.1}PbI_3$ showed enhanced photo-stability and thermal stability [35]. To overcome these stability issues, perovskite modules may require more expensive encapsulation. Next to this, ionic migration could affect the long-term stability as well [36]. As far as we are aware, the longest lifetimes reported for perovskite solar cells are about a year [37, 38]. This is much shorter than the expected lifetime of 25 years for commercially available solar panels. On the other hand, perovskite solar modules have the shortest energy payback time (EPBT) among existing PV technologies according to a study by Gong et al. [39].

Another issue is that replacement of lead as a major constituent of perovskites turns out to be difficult. The use of lead raises toxicity issues during device fabrication, deployment and disposal. Tin (Sn) has been considered the most likely substitute to lead and forms similar compounds with

more ideal bandgaps [1]. However, tin-based perovskites generally suffer from rapid degradation in the presence of air. This is mainly due to the instability of Sn_2^+, which is easily oxidized to Sn_4^+ [40]. Besides, also Sn-based perovskites are known to have negative impact on health and environment [41]. The current perovskite technology can only be deployed in a completely safe way with use of encapsulation that is resistant to extreme conditions. Therefore it remains interesting to look for other alternatives to lead, like bismuth [42].

1.5. Hysteresis

Current-voltage (J-V) measurements of perovskite solar cells strongly depend on the history of the device. Measured J-V curves can be drastically different depending on the preconditions, the scan direction and scan rate [43]. This phenomenon is known as *hysteresis* in the current-voltage curve. Anomalous hysteresis has been observed and reported by many research groups, but the underlying processes are not yet completely understood. It has been suggested to originate from trapping and de-trapping of charge carriers, (slow) ion-migration or ferroelectric behaviour of the perovskite [44, 45]. So far, there is no theoretical study of the origin of hysteresis due to defects, most likely because of the inherent complexity and numerical stability of such solutions. This thesis presents a novel study of the hysteresis phenomena from the theory of defects in semiconductors.

Figure 1.7 shows the typical dependence on scan rate and scan direction. Devices exhibit negligible hysteresis for both very slow and very fast scan rates. At intermediate scan rates, usually in the commonly used range of $1\,\mathrm{mV\,s^{-1}}$ to $100\,\mathrm{mV\,s^{-1}}$, severe hysteresis is observed [45]. At much higher scan rates another type of hysteresis appears. This is caused by capacitive effects, a very common phenomenon for semiconductor junctions. Also pre-exposure to light (light-soaking) can change device performance [29]. The magnitude of the hysteretic effect depends on light and voltage bias conditions prior to the measurement, the scan direction and the scan rate used to measure the J-V curve [44].

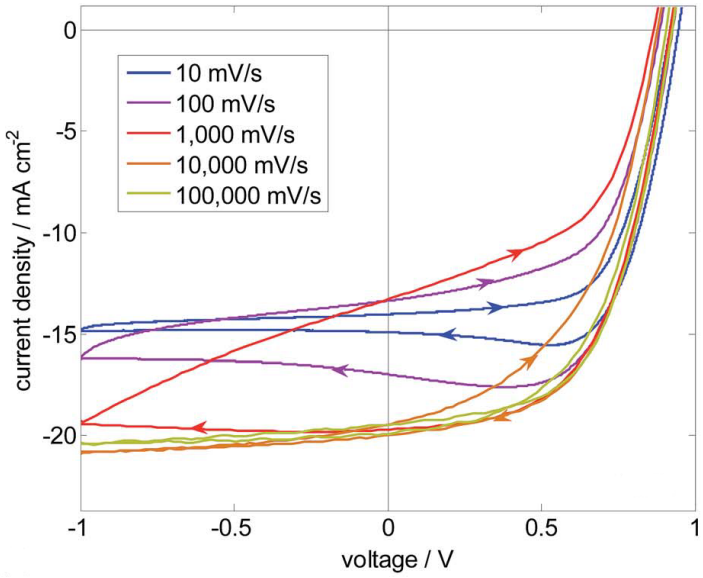

Figure 1.7: Current–voltage curves of a real perovskite solar cell with pronounced hysteresis for a series of scan rates. The scan direction is indicated with arrows. Reproduced from Tress et al. [45].

Hysteresis complicates device characterizations because the power conversion efficiency is usually under- or overestimated depending on the scan direction. Understanding the nature behind hysteresis can provide useful insights for further progress and performance improvements.

1.6. TCAD simulations

The physical processes in perovskite solar cells are often too complex to be understood entirely by simple explanations or described by analytical expressions. Numerical simulations offer the opportunity to analyse and compare the effects of underlying physics. Device modeling has been widely used in industry to analyse fabricated cells and to predict the effect of modifications to their design and materials [46]. For example, Yue et al. [47] used simulations to optimize the thickness of different layers in PSCs, Neukom et al. [27] used simulations to obtain a deeper understanding of the physical processes in perovskite material and Liu et al. [48] provides a better quantitative understanding of the surface recombination velocity with the use of numerical simulations. Simulations can also be used to analyse different cell structures (see for example Wang et al. [49]).

During this project we want to study current-voltage hysteresis in perovskites using simulations based on the drift-diffusion model (see section 2.1). Other studies used additional models for ion diffusion to explain hysteresis. We instead use a novel approach that is entirely based on conventional semiconductor theory.

Technology Computer-Aided Design (also known as TCAD) will be an important tool for this project. TCAD refers to the use of numerical computer simulations to develop and optimize the fabrication and operation of semiconductor devices. TCAD tools solve partial differential equations, such as diffusion and transport equations inside the semiconductor device. Because of their accuracy and self-consistent models, TCAD simulations are used widely in the semiconductor industry, where they substitute costly and time-consuming tests with complex semiconductor devices. There are many TCAD packages available; the modeling software Sentaurus (Synopsis) and Atlas (Silvaco) have become widely used in the photovoltaic industry [46]. In order to use these software packages, the physical models need adjustments to the specific demands for solar cells. We will use Sentaurus TCAD to model perovskite solar cells. This is a complex toolbox that contains almost all relevant physical models (e.g. drift-diffusion model, SRH recombination, bandgap lowering).

1.7. Project description and outline

The focus of this thesis project is to implement a simulation platform of perovskite solar cells and to analyse charge transfer mechanisms among energy states including defect states in the bandgap. We will evaluate transient behaviour of the system in frequency/time and voltage domain and evaluate and identify the limiting physical mechanisms. In this project, based on rigorous TCAD simulations, we will address the following scientific questions:

i) Can we emulate transient behaviour in perovskite solar cells using a drift-diffusion model? What are the advantages and limitations of the model?

ii) What is the driving force behind the current-voltage hysteresis?

iii) How can the performance of perovskite solar cells be improved?

Chapter 2 introduces the fundamental semiconductor theory and gives a more thorough theoretical background on perovskite solar cell. Chapter 3 treats the methodology of modeling perovskite solar cells. Chapter 4 describes the physical processes underlying hysteresis and in chapter 5 we explore which defects play an important role in the origin of hysteresis. In chapter 6 a realistic model based on slow defects is discussed and its response upon variation of defect distributions, capture cross-sections and scan rate is discussed. We provide a broader discussion about the origin of hysteresis in chapter 7. The conclusions of this study are presented in chapter 8.

2

Theoretical background

This chapter describes the theory used as foundation of perovskite solar cell modeling. It covers the most important concepts of semiconductor physics, including the drift diffusion model (section 2.1), defect states and their dynamics (section 2.2) and recombination processes (section 2.3). We describe the working principle of perovskite solar cells (section 2.4) and give an overview of defects in PSCs (section 2.5). Time-dependent hysteresis in PSCs is described (section 2.6) and a discussion about the possible origins is provided (section 2.7). The chapter is concluded with the introduction of the Hysteresis Index, which is an important figure of merit for quantifying hysteresis.

2.1. Drift-diffusion model

Electrons in a semiconductor are described by the theory of quantum mechanics. The use of a fully quantum-mechanical description of semiconductors for simulations and computations is not feasible because of the enormous amount of interacting particles inside a semiconductor material. Instead, it is common to use a semi-classical model to describe and explain the physics of semiconductor devices. In this approach, it is assumed that the movement of electrons in the conduction band (and holes in the valence band) can be described using Newton's laws and that properties of the particles, such as their effective mass, are determined by the quantum theory of solids. This work only briefly explains the involved concepts. More detailed descriptions of semiconductor physics theory can be found in Sze and Ng [26] and Neamen [25].

2.1.1. Fermi-Dirac statistics

Electrons of isolated atoms occupy atomic orbitals, each of which has a discrete energy level. When multiple atoms are joined together in a crystal, the orbitals start to overlap. Because of Pauli's exclusion principle, no two electrons can occupy the same quantum states. The energy levels split and continuous bands of allowed energy states are formed. The occupation of these states is described by Fermi-Dirac statistics. The probability that a quantum state at energy E will be occupied by an electron is given by a probability function $f(E)$:

$$f(E) = \frac{1}{1 + \exp\left(\frac{E - E_F}{kT}\right)} \tag{2.1}$$

with k the Boltzmann constant and T the temperature. The energy E_F is called the Fermi level. In thermal equilibrium the Fermi level is constant throughout the entire system. Combining Fermi-Dirac statistics with the density of states (DOS), the number of states that are available at each level of energy per unit volume, gives us the number of electrons at each energy. In semiconductors the energy bands are almost entirely filled up to the *valence band*. The empty band above the valence band is known as the *conduction band*. In between these bands there is a forbidden energy range that electrons cannot populate. This forbidden energy range, which is on the order of a few eV, is called the *bandgap*. The lowest energy level of the conduction band is called the conduction band edge (CBE) and the highest energy level of the valence band is known as the valence band edge (VBE). They are denoted by E_C and E_V respectively.

2.1.2. Concept of holes

Because the valence band is almost entirely filled by electrons, it is easier to describe it using the empty states instead. An electron moving from one state to another is equivalent to an empty state moving in the opposite direction. The net motion of electrons in a nearly full band can thus be described using the empty states, which we call *holes*. Although the concept of holes is very convenient for calculations, it may sometimes lead to confusion. It is important to keep in mind that the movement of a hole is equivalent to the movement of an electron in the opposite direction and vice versa. Moreover, holes usually have a different effective mass, mobility, etc. The subscripts n and p are used to indicate that a parameter corresponds to electrons or holes respectively.

2.1.3. Drift and diffusion

The basic semiconductor model is also known as the drift-diffusion model or drift-diffusion approximation. As the name suggest, two main transport mechanisms are considered: drift and diffusion. Drift is the movement of particles caused by an electric field, whereas a diffusion is due to density gradients. The drift-diffusion model can be expressed using the basic semiconductor equations, which can be separated into three classes: current-density equations, continuity equations and Poisson's equation [50].

The total current density in a semiconductor is the sum of the drift current and the diffusion current. For electrons and holes the current-density equations are respectively given by

$$\vec{\mathbf{J}}_n = -e\mu_n n\nabla\psi + eD_n\nabla n \tag{2.2}$$

$$\vec{\mathbf{J}}_p = -e\mu_p p\nabla\psi - eD_p\nabla p \tag{2.3}$$

where n is the electron concentration, p the hole concentration, μ the electron/hole mobility, D the diffusion coefficient and e the elementary charge. The mobility and diffusion coefficient are related to each other according to Einsteins relation:

$$\frac{D_n}{\mu_n} = \frac{D_p}{\mu_p} = \frac{kT}{e} \tag{2.4}$$

where k is the Boltzmann constant and T the temperature.

The second class of equations, known as the continuity equations, describe the balance of particle fluxes, generation and recombination within the device. They read

$$\frac{\partial n}{\partial t} = \frac{1}{e}\nabla\cdot\vec{\mathbf{J}}_n + G - R \tag{2.5}$$

$$\frac{\partial p}{\partial t} = -\frac{1}{e}\nabla\cdot\vec{\mathbf{J}}_p + G - R \tag{2.6}$$

Here G and R are the generation rate and recombination rate per unit volume. Both equations state that the time rate of change in electron (hole) concentration at a particular location is equal to the sum of the net inflow of electrons (holes) and the generation of electrons (holes) minus the recombination of electrons (holes).

To obtain the final equation, we use Gauss's law, which gives the relation between the distribution of charge and the electric field:

$$\nabla\cdot\vec{\mathbf{D}} = \rho \tag{2.7}$$

In dielectric matter, we can write $\vec{\mathbf{D}} = \epsilon\vec{\mathbf{E}}$ with ϵ the permitivitty of the semiconductor material. The charge density can be expressed in terms of the p, n, the donor density N^+_{don} and the acceptor density N^-_{acc}[1]. Using the defining relation of the electric potential $-\nabla\psi = \vec{\mathbf{D}}$, we finally arrive at Poisson's equation:

$$\nabla\cdot(\epsilon\nabla\psi) = -e\left(p - n + N^+_{\text{don}} - N^-_{\text{acc}}\right) \tag{2.8}$$

Together equations (2.2),(2.3),(2.5),(2.6) and (2.8) constitute the basic semiconductor equations. Additional models are required to compute the carrier mobility, generation and recombination.

[1] A description of donors and acceptors can be found in Sze and Ng [26].

2.1.4. Material interfaces

At the interface between two different materials, a heterojunction is formed. At such interfaces E_C and E_V are often not continuous (see for example the band diagram in Figure 1.6 in chapter 1). The jump across the interface is called band offset and can be described using the electron affinity rule. This rule reads that the band offsets equal:

$$\Delta E_C = E_{C,1} - E_{C,1} = e(\chi_1 - \chi_2) \tag{2.9}$$

$$\Delta E_V = E_{V,1} - E_{V,1} = \left(e\chi_1 + E_{G,1}\right) - \left(e\chi_2 + E_{G,2}\right) \tag{2.10}$$

where χ is the electron affinity and E_G the bandgap of the respective material.

At heterojunctions conventional transport equations can no longer be used because gradients are ill defined across the interface. Transport across the interface is instead described by thermionic emission and tunneling. More on this can be found in Sze and Ng [26] or Neamen [25].

2.1.5. Quasi Fermi-levels

When the device is not in equilibrium, the Fermi level is no longer defined. In that case we can use the conduction band quasi-Fermi level ($E_{F,n}$) and valence band quasi-Fermi level ($E_{F,p}$) instead. They are defined using the following relations:

$$n = N_C F_{1/2}\left(\frac{E_{F,n} - E_C}{kT}\right) \tag{2.11}$$

$$p = N_V F_{1/2}\left(\frac{E_V - E_{F,p}}{kT}\right) \tag{2.12}$$

where $F_{1/2}$ is the Fermi integral of order 1/2. N_C and N_V are the effective density of states of the conduction band and the valence band respectively. When the carrier densities are not too high, they can be very well approximated using Boltzmann statistics. Although in all our simulations we use Fermi-Dirac statistics because this is physically more correct, the formulas based on Boltzmann statistics are more insightful and worth stating here:

$$n = N_C \exp\left(\frac{E_{F,n} - E_C}{kT}\right) \tag{2.13}$$

$$p = N_V \exp\left(\frac{E_V - E_{F,p}}{kT}\right) \tag{2.14}$$

2.2. Defect states

Defects in the lattice introduce allowed energy states in the bandgap, so-called defect states. An electron (or hole) can be trapped in such a defect. Defects (or traps) may therefore lead to localized charge accumulation.

The electronic states associated with defects are typically divided into two broad categories: shallow and deep defects [51]. Shallow defects correspond to centers with extended electronic wave functions and their energy is close to either the valence or conduction band. These states usually arise because of disorder. Deep defects on the other hand, are strongly localized and lie deeper in the bandgap. Deep states act as recombination centers and generally decrease solar cell performance (see also section 2.3).

The occupation dynamics of defect states are described by the capture and emission of electrons. We consider the four process shown in Figure 2.1:

(1) Capture of an electron from the conduction band.

(2) Emission of an electron to the conduction band.

(3) Capture of an electron from the valence band.

(4) Emission of an electron to the valence band.

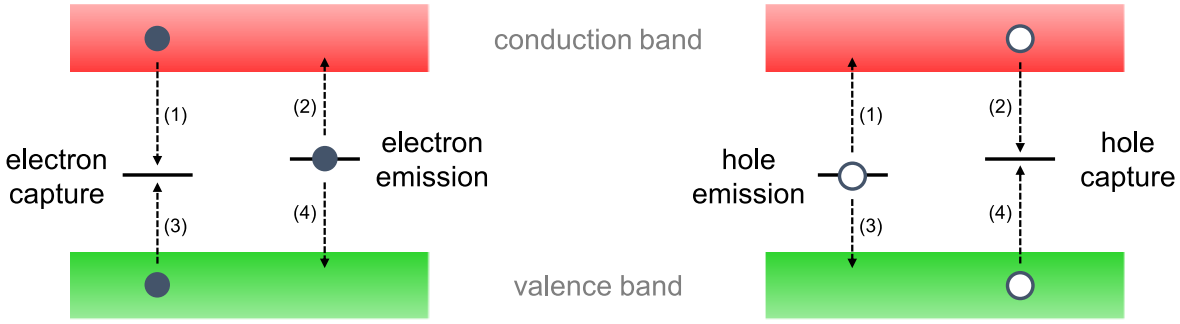

Figure 2.1: Illustration of the four processes involved in the occupation dynamics of defects, using the electron picture (left) and the hole picture (right).

The electron occupation f_t of a defect (0 if empty and 1 if occupied) changes because of these processes. This can be described using

$$\frac{\partial f_t}{\partial t} = (1 - f_t)c_C^n - f_t e_C^n + (1 - f_t)c_V^n - f_t e_V^n \tag{2.15}$$

where c_C^n denotes the electron capture rate from the conduction band of an empty defect and e_C^n denotes the electron emission rate to the conduction band of an occupied defect. The electron capture and emission rates from and to the valence band are denoted by c_V^n and c_V^n respectively.

Sometimes it is easier to describe these processes using holes instead: capture of an electron is the same as emission of a hole and vice versa. This is shown in the right side of Figure 2.1. One can easily switch between both pictures by substituting $c_{C/V}^p = e_{C/V}^n$ and $e_{C/V}^p = c_{C/V}^n$ where c_i^p and e_i^p are the hole capture and emission rates. Note that the hole occupation of a defect equals $1 - f_t$.

The electron capture rate c_C^n from the conduction band is modeled as

$$c_C^n = \sigma_n v_{th}^n n \tag{2.16}$$

with σ_n the electron capture cross-section, v_{th}^n the electron thermal velocity and n the electron density at the same location as the defect. Similarly, the capture of holes from the valence band is modeled as

$$c_V^p = \sigma_p v_{th}^p p \tag{2.17}$$

with σ_p the hole capture cross-section, v_{th}^p the hole thermal velocity and p the hole density at the same location as the defect.

In thermal equilibrium the capture rate c_C^n of electrons from the conduction band must be equal to the emission rate e_C^n of electrons to the conduction band. A relation between capture- and emission coefficients follows from the principle of detailed balance: in thermodynamic equilibrium, the rate of capturing electrons from a reservoir must be equal to the rate of emitting electrons to this reservoir. This reservoir can either be the conduction band electrons or the valence band electrons. The emission rates are related to the capture rates as follows:

$$\frac{e_C^n}{c_C^n} = \exp\left(\frac{E_{trap} - E_{F,n}}{kT}\right) \tag{2.18}$$

$$\frac{e_V^n}{c_V^n} = \exp\left(\frac{E_{trap} - E_{F,p}}{kT}\right) \tag{2.19}$$

with E_{trap} the defect energy and $E_{F,n}$ and $E_{F,p}$ the quasi-Fermi levels for electrons and holes respectively. In Appendix A we present a simplified derivation based on the work of Shockley and Read Jr [52].

2.3. Recombination

Electrons and holes can recombine through various recombination mechanisms. The most important are direct recombination, Shockley-Read-Hall recombination, Auger recombination.

2.3.1. Direct recombination

Direct recombination, also known as *band-to-band recombination*, is a process that mainly occurs in direct bandgap semiconductors . Because hybrid lead halide perovskites are considered direct bandgap semiconductors in most published literature, this process is also relevant for PSCs [53]. The recombination rate corresponding to this process is proportional to the concentration of electrons n and the concentration of holes p [26]:

$$R_{\text{direct}} = \beta\left(np - n_{\text{i}}^2\right) \tag{2.20}$$

Here β is the recombination coefficient. For lead-halide perovskites the recombination coefficient lies approximately in the range 10^{-11} to 10^{-9} cm^3 s^{-1} [54–56].

2.3.2. Shockley-Read-Hall recombination

In the Shockley-Read-Hall (SRH) recombination process, electrons and holes do not recombine directly from band to band. Instead recombination is facilitated by electronic defect states: an electron from the conduction band can be trapped by a defect and consequently recombine with a hole from the valence band. Any excess energy in this process is dissipated into the lattice, making it a non-radiative process [6]. The recombination rate is given by [26]:

$$R_{\text{SRH}} = \frac{\sigma_n \sigma_p v_{\text{th}} N_{\text{t}} \left(pn - n_i^2\right)}{\sigma_n \left(n + n_i \exp\left(\frac{E_{\text{trap}} - E_{\text{F},i}}{kT}\right)\right) + \sigma_p \left(p + n_i \exp\left(\frac{E_{\text{F},i} - E_{\text{trap}}}{kT}\right)\right)} \tag{2.21}$$

where σ_n and σ_p are the capture cross-sections for electrons and holes, v_{th} is the themal velocity, N_{t} the defect density, n_i the intrinsic carrier density, E_{trap} the defect energy and $E_{\text{F},i}$ is the Fermi level of an intrinsic semiconductor.

2.3.3. Auger recombination

Auger recombination is a three particle process. It is the direct recombination of an electron and a hole, accompanied by momentum and energy transfer from the recombining electron and hole to a third particle. If this third particle is an electron, it gets excited into the conduction band and then relaxes by transferring its energy to the lattice. Similarly, if the third particle is a hole, it gets excited into the valence band and relaxes again. The recombination rates for electron-electron-hole (R_{eeh}) and electron-hole-hole (R_{ehh}) processes strongly depend on the carrier concentrations and are given by

$$R_{\text{eeh}} = C_n n^2 p \tag{2.22}$$

$$R_{\text{ehh}} = C_p n p^2 \tag{2.23}$$

where C_n and C_p are the Auger coefficients. For $MAPbI_3$ the Auger coefficients are estimated to be approximately 10^{-28} cm^6 s^{-1} [57, 58]. The net rate of Auger recombination is modeled as

$$R_{\text{Aug}} = \left(C_n n + C_p p\right)\left(np - n_{\text{i}}^2\right) \tag{2.24}$$

2.4. Working principle of perovskite solar cells

Despite the fact that the underlying physical processes of PSCs are not yet entirely understood, the main working principles are very similar to other thin-film solar cells. Almost all of the light is absorbed in the perovskite layer, where electron-hole pairs are created by the absorption of a photon. Assisted by a built-in electric field, the electrons and holes are separated and extracted from the absorber layer at the ETL and HTL respectively.

2.4.1. Built-in electric field

The built-in electric field is a result of a work function difference between the perovskite layer and the ETL and between the perovskite and the HTL. The ETL has a lower work function than the perovskite. When the two materials are placed in contact, electrons diffuse from the ETL to the perovskite layer, leaving behind positively charged ions. The HTL has a higher work function than the perovskite. When those two materials are placed in contact, holes diffuse from the HTL into the perovskite layer, leaving negatively charged ions behind. The resulting charge distribution creates a built-in electric field in the perovskite layer. A more detailed description can be found in Sze and Ng [26] or Neamen [25].

2.4.2. Band diagrams

Figure 2.2a shows a band diagram of a perovskite solar cell in equilibrium without illumination. Ideally the perovskite absorber layer is an intrinsic semiconductor and the depletion region extends over the entire absorber layer, resulting in a uniform built-in electric field. In practice unintentional doping usually causes the absorber layer to be p-type or n-type [59–62]. As a consequence the electric field is not uniform and weaker on one side of the device.

The ETL and the perovskite must have a relatively small conduction band offset, such that electrons can be easily extracted. A large valence band offset is preferable as this prevents holes from reaching the ETL, where they could recombine with electrons before extraction from the device. Analogously, the HTL and the perovskite should have a relatively small valence band offset and a large conduction band offset.

Under illumination the Fermi level splits into E_{Fn} and E_{Fp}. The difference between these levels is a measure of the conversion efficiency from radiative energy to electrochemical energy. When a bias is applied, the built-in electric field is reduced and eventually the quasi-Fermi levels will be flat. The open circuit voltage V_{OC} is therefore limited by the work function of the carrier selective contacts layers. Figure 2.2b shows the band diagram in open circuit.

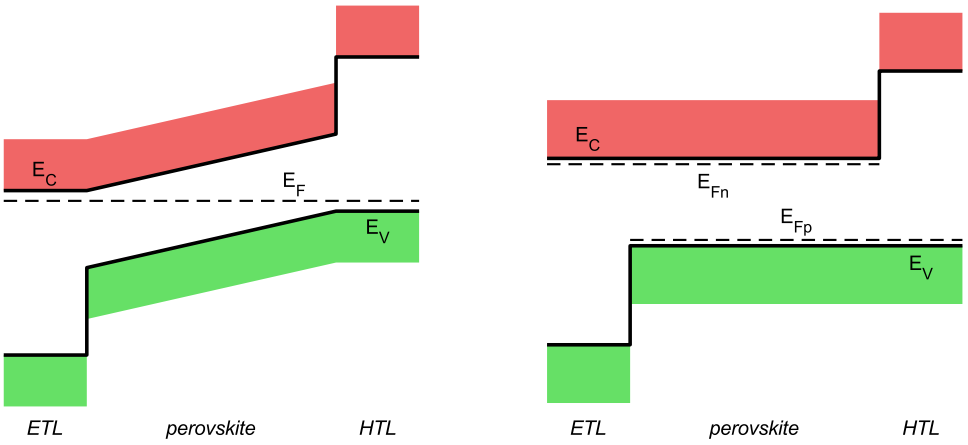

(a) Band diagram in the dark.

(b) Band diagram under illumination.

Figure 2.2: Simplified band diagrams of a PSC (a) in the dark with no applied bias and (b) under illumination in V_{OC}.

2.4.3. Absorption coefficient

Figure 2.3 shows the absorption coefficient of $MAPbI_3$ and several typical other PV materials. The high absorption coefficients of perovskite materials is a great advantage, because a thin perovskite layer suffices to absorb most of the light [63]. This means that the carriers only have to travel a short distance, which reduces the probability that they recombine before they are extracted. Another advantage of a thin absorber layer is that the built-in electric field is stronger, because the same potential drops over a shorter distance.

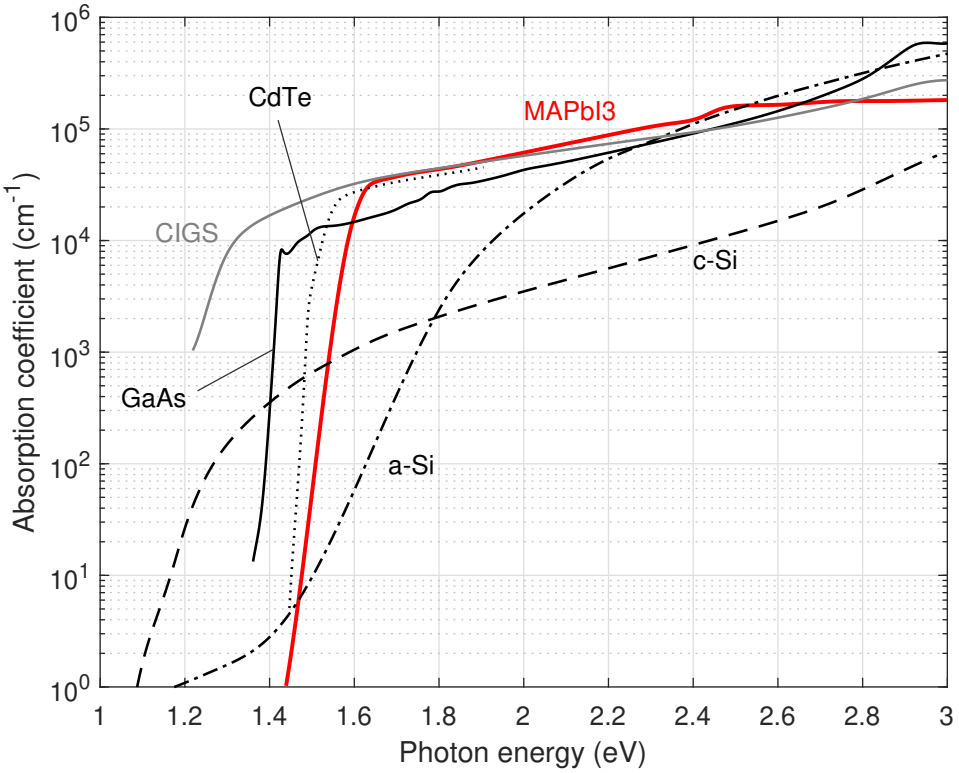

Figure 2.3: Effective absorption coefficient of a $MAPbI_3$ perovskite thin film (in red) compared with other typical PV absorber materials. Reproduced from De Wolf et al. [63].

2.5. Defect states in perovskite solar cells

In recent years a lot of experimental and theoretical evidence for defect states in perovskites has been found [64–67]. The excellent performance of PSCs is often attributed to low defect densities compared to other amorphous materials. Nevertheless, there is still much uncertain about the defect physics in perovskites, including their causes and nature.

Defects in crystalline semiconductors can be categorized as either interruptions to an otherwise perfect crystal lattice or as foreign atoms in the lattice (impurities). Figure 2.4 shows what these defects look like in a perovskite crystal.

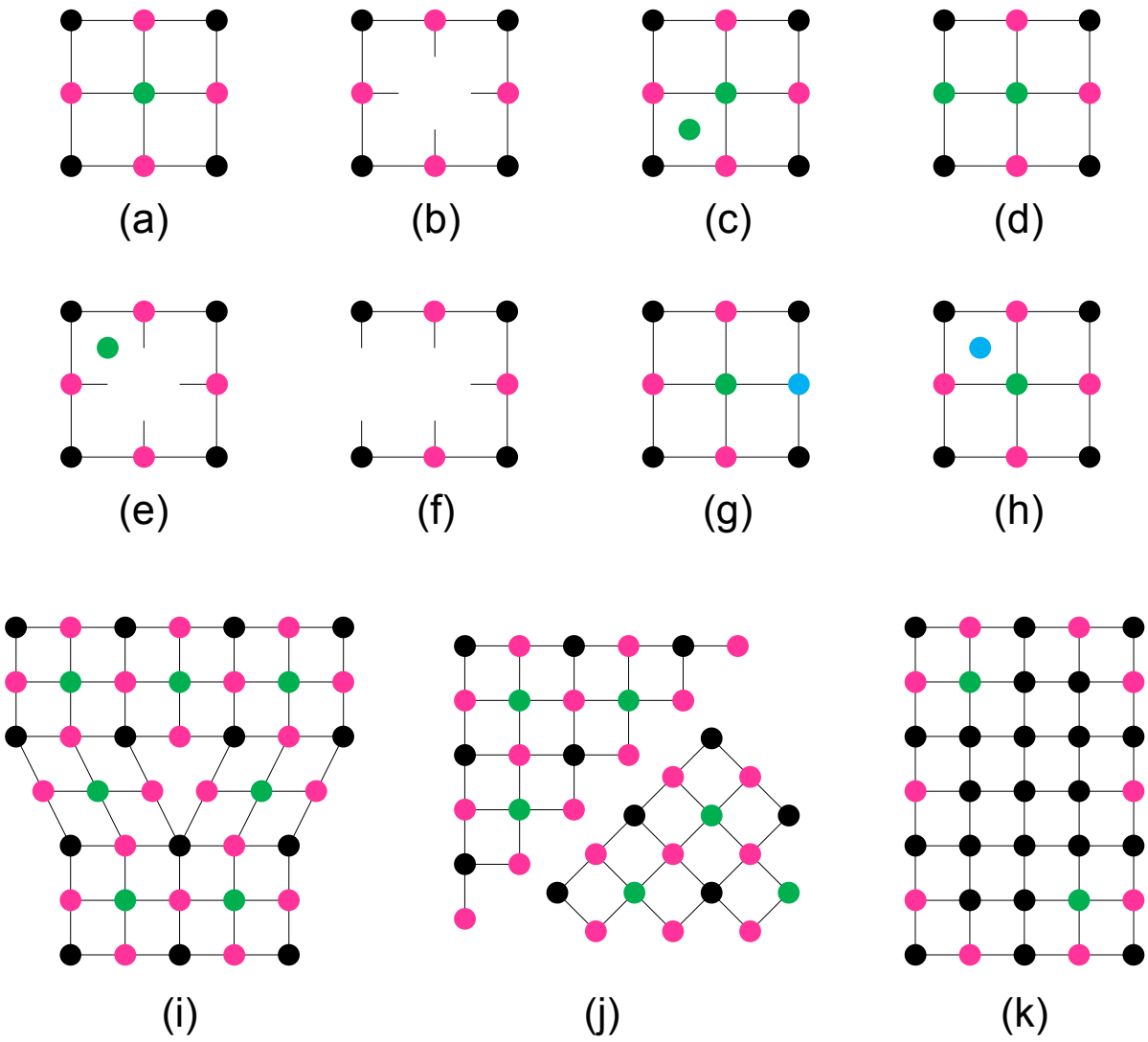

Figure 2.4: Illustration of point defects and higher-dimensional defects in a perovskite crystal lattice (green, black, and pink dots represent the A-, B-, and X-site ions respectively). (a) perfect lattice, (b) vacancy, (c) interstitial, (d) anti-site substitution, (e) Frenkel defect (simultaneous interstitial and vacancy of the same ion), (f) Schottky defect (anion and cation vacancies occurring together), (g) substitutional impurity (h) interstitial impurity, (i) edge dislocation, (j) grain boundary, (k) precipitate. Reproduced from Ball and Petrozza [68].

2.5.1. Measurement techniques

The energetic and spatial distribution of defects in PSCs have been primarily determined using thermal admittance spectroscopy (TAS), thermally stimulated current (TSC), deep level transient spectroscopy (DLTS) and space-charge limited current (SCLS) analysis [69]. The results vary a lot, most likely because of different fabrication procedures. Also ion migration complicates the various analyses. Below we briefly discuss some of these techniques in more detail. This should give a good impression of the complexity and resulting uncertainties of defect measurements.

A relatively popular technique for perovskites is thermal admittance spectroscopy (TAS) [51]. In admittance spectroscopy measurements the complex admittance $Y = G + j\omega C$ is measured, which is a function of the conductance G and the capacitance C. To this end, the solar cell is biased at a fixed DC operating condition and an AC signal with frequency ω is applied to the cell. The measured admittance mainly originates from charging and discharging defects at locations where their energy level is very close to the Fermi level. This is illustrated in Figure 2.5. Electronic defect states above the Fermi level are assumed to be empty and states below the Fermi level to be filled. When a small deviation of the potential is applied, the Fermi level changes slightly and consequently some defect states will release or capture charge carriers. The admittance depends on the applied frequency ω and temperature. Defect

states can only respond if the frequency is low enough and/or the temperature high enough (see also section 2.2). The frequency and temperature determine a cut-off energy (demarcation energy) E_ω and only defect states for which the defect energy E_t is smaller than E_ω are able to respond. The energetic distribution of defects can thus be measured by modulating the frequency and temperature.

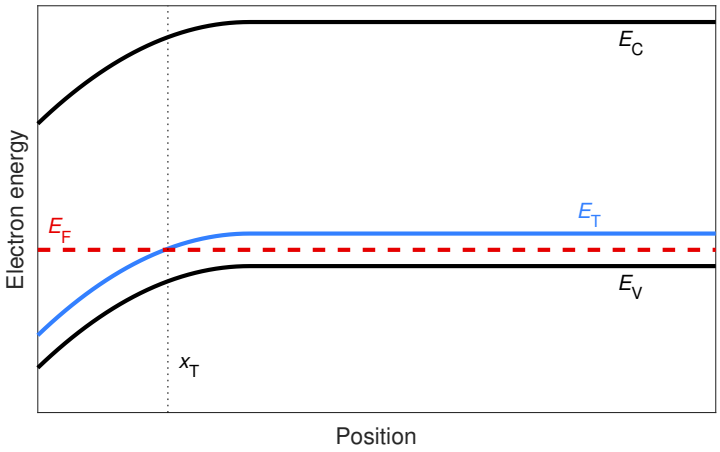

Figure 2.5: Schematic of band bending with one deep defect state at energy E_T. Localized defect states near x_T can change their occupation in response to a small change in the Fermi level caused by the applied AC voltage.

Drive-level capacitance profiling (DLCP) is an alternate capacitance-based technique similar to admittance spectroscopy. It can be used to measure spatial and the energetic distribution of defects in perovskite devices [70]. A detailed explanation of this technique can be found in the work of Heath et al. [71].

Another technique that can be used is thermally stimulated current (TSC) measurements. For this technique the sample is first cooled to a very low temperature. Then charge carriers are generated by illumination and the sample is held at a constant temperature for some time so that charge carriers will relax in the density of states and occupy defect states. Now the temperature is increased at a (slow) constant rate and as a result defect states gradually release the trapped carriers. At low temperatures only shallow defects will release carriers, but as temperature increases there will be enough thermal energy for deep defects to release carriers. The release of carriers induces a current which can be measured and related to the defect density.

2.5.2. Deep defects

Yin et al. showed using theoretical calculations that the dominant defects in $MAPbI_3$ are shallow defects [65, 72]. They calculated that defects with deep levels in the archetypal perovskite $MAPbI_3$ have high formation energies [65]. Based on this result they concluded that deep defects are unlikely to form and that perovskites only have shallow defects. This partially explains the long electron-hole diffusion length and high open circuit voltage in perovskite-based solar cells. Indeed very low defect densities of $3.3 \times 10^{10}\,\mathrm{cm}^{-3}$ are observed in $MAPbI_3$ single crystals [66]. However, based on first-principles calculations, Agiorgousis et al. showed that strong interactions between lead cations and iodide anions result in particular charge states with significantly lowered energy [73]. This would lead to the presence of deep defects within the band gap. Depending on the growing conditions, deep defects can be present in the material.

2.5.3. Interface defects

At the interface between different layers there usually is a mismatch between the lattices of the two layers. The density of deep defects close to the interfaces can therefore be orders of magnitude larger than in the bulk. In hybrid metal-halide perovskties almost all charge recombination centers are localized on the surfaces [74].

Using drive-level capacitance profiling, Ni et al. were able to resolve the spatial and energetic distribution of defect states in metal halide perovskite solar cells. Figure 2.6 shows the spatial profile of defects in polycrystalline films. They measured defect densities of $2.2 \times 10^{16}\,\mathrm{cm}^{-3}$ in the perovskite

layer near the ETL interface and 1.2×10^{17} cm^{-3} near the HTL interface [70]. The charge defect densities of all depths of the interfaces were one to two orders of magnitude greater than that of the film interior, with a minimal density of 9.2×10^{14} cm^{-3}. Also Baumann et al. measured much lower densities in the bulk. Using TSC measurements, they found defect states in $MAPbI_3$ solar cells with activation energies around 500 meV and a defect density of approximately 10^{15} cm^{-2} [64].

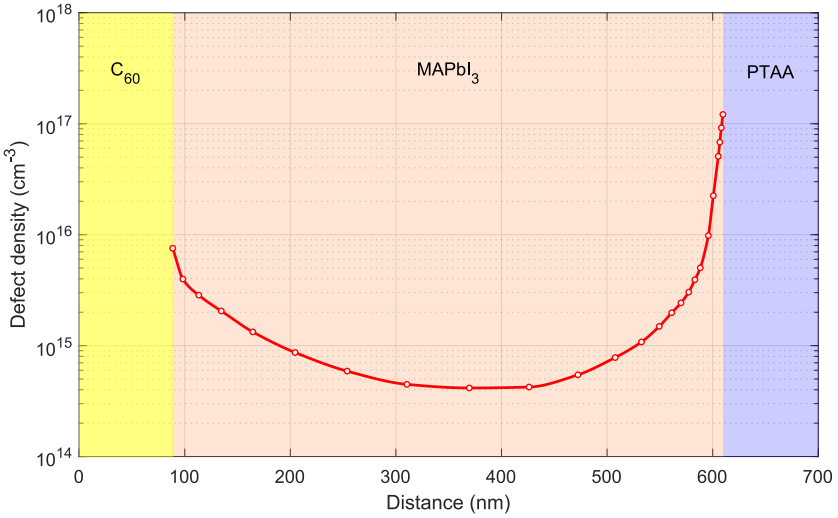

Figure 2.6: Spatial profile of defect density for a $MAPbI_3$ PSC with C_{60} as ETL and PTAA as HTL. Data is adapted from Ni et al. [70].

2.5.4. Passivation

By depositing a thin layer of a suitable material onto the perovskite interface, the number of defects can be reduced. This is called (chemical) surface passivation. For example various materials can be used to passivate the interface between ETL and perovskite, like self-assembled monolayers of organic molecules (SAMs) and fullerene/graphene derivatives [74].

2.5.5. Tail states

Amorphous materials do not have long-range structural order as in single-crystals. The structural disorder gives rise to localized electronic states inside the bandgap with energy levels just above the valence band edge and just below the conduction band edge (see Figure 2.7). These shallow states are known as band tails and show almost universal characteristics among different materials [75]. Band tail states are observed in a large variety of amorphous semiconductors and originate from structural disorder in the material [76–78]. The DOS of Urbach tails follows an exponential distribution with a characteristic energy W_V (valence band tail states) and W_C (conduction band tail states). The characteristic energy is a measure of the width of the band tails (see chapter 3 for a more detailed description).

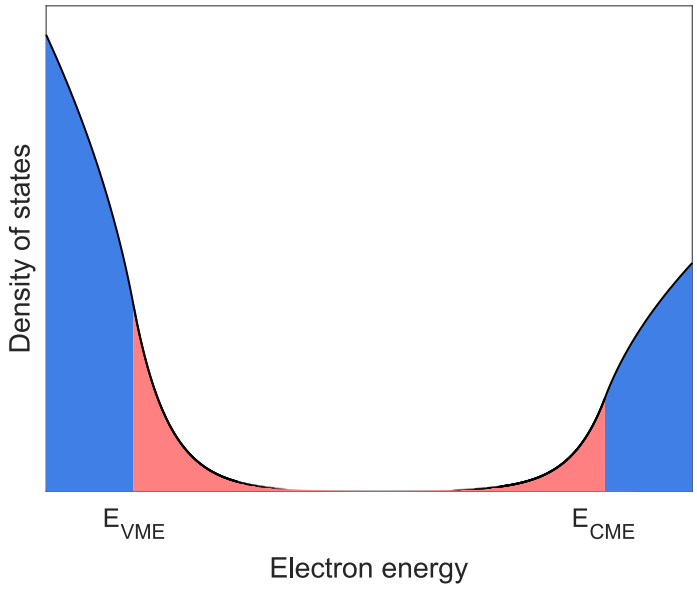

Figure 2.7: Illustration of the density of states for a perovskite material. The valence and conduction band are shown in blue and the tail states are red. E_{VME} and E_{CME} are the valence band mobility edge and the conduction band mobility edge respectively. Note that, for clarity, the characteristic energies are not to scale; tail states are actually very shallow.

Band tail states give rise to an exponential onset in the optical absorption edge [79, 80]:

$$\alpha(\hbar\omega) = \alpha_0 \exp\left(\frac{\hbar\omega - \hbar\omega_0}{E_U}\right) \tag{2.25}$$

Here α is the absorption coefficient, $\hbar\omega$ the photon energy and E_U the Urbach energy. In semilogarithmic plots of the absorption spectra the exponential onsets are clearly visible as straight lines. This is shown in Figure 2.8 for $MAPbI_3$ films at different temperatures. The Urbach energy E_U is typically several meV and can be easily determined from the slope of the exponential absorption curve.

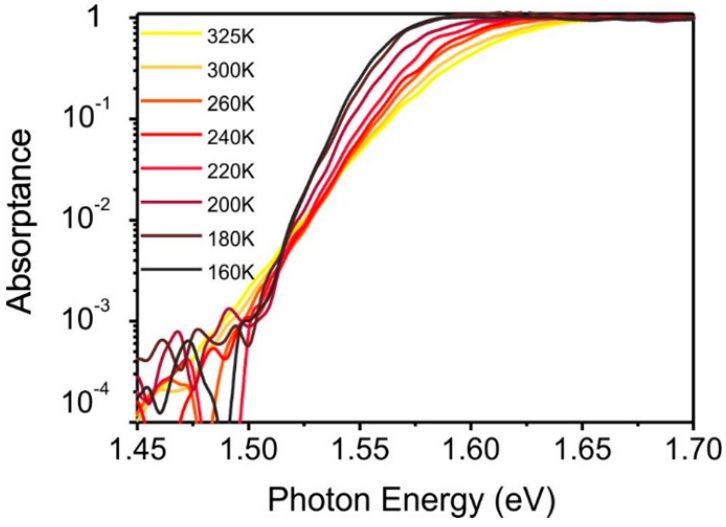

Figure 2.8: Absorption spectra of $MAPbI_3$ films. Adapted (in edited format) from Ledinsky et al. [81].

The Urbach energy is considered a good estimate for the characteristic energies W_V and W_C of the band tail states. Values of 15 meV, 14.8 meV, 16 meV for the Urbach energy of $MAPbI_3$ at room temperature have been reported [63, 81]. For $MAPbBr_3$ an Urbach energy of 23 meV is observed [82].

Based on low-temperature photoluminescence measurements and a Monte Carlo simulation, Wright et al. [67] concludes that $FAPbI_3$ has an exponential tail-state density with characterestic energy scale of 3 meV. This value is much smaller than the Urbach energies observed for $MAPbI_3$, which can be partly explained by the fact that these measurements were not performed at room temperature. Such a temperature-dependency would be in line with the results from Ledinsky et al. [81]. Unfortunately little is known about tail states in other perovskite materials.

2.6. Current-voltage hysteresis

Hysteresis in the J-V curve is a phenomenon that cannot easily be expressed in a single numerical value. Many different behaviours are observed. It manifests itself in reduced short-circuit current, open-circuit voltage, fill-factor or a combination of the three. Also an S-shaped kink is sometimes observed for the forward scan [45]. In general the performance of perovskite solar cells is less during a forward scan than during a reverse scan, but opposite behaviour has also been observed [83]. The former is known as normal hysteresis, whereas the latter is referred to as inverted hysteresis. Figure 2.9 shows examples of both behaviours. It can also occur that there are one or more crossing points between the reverse and forward J-V scans. This is known as mixed hysteresis.

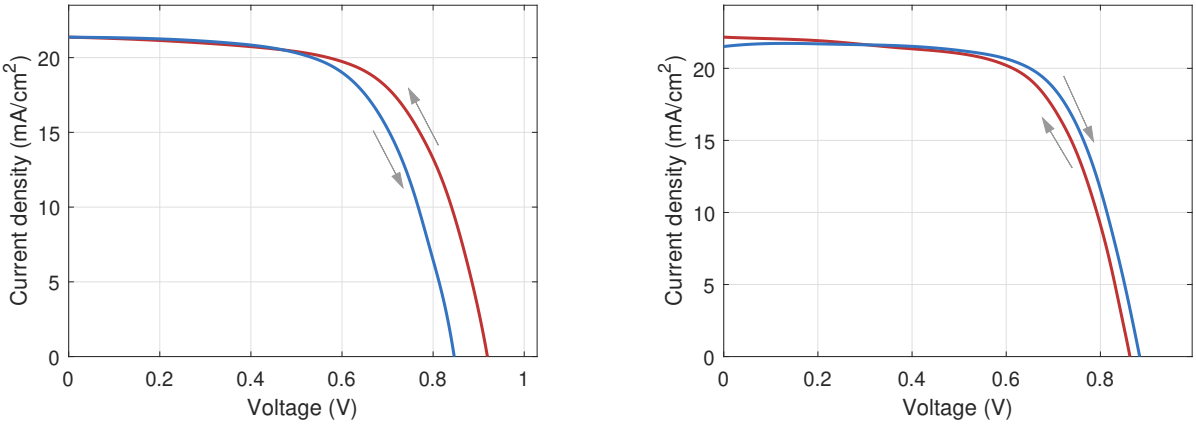

(a) Normal hysteresis.

(b) Inverted hysteresis.

Figure 2.9: J-V curves of mesoscopic PSCs. Data obtained from Rong et al. [83]. (a) Device showing normal hysteresis where the performance during reverse scan is better than during the forward scan. (b) Device showing inverted hysteresis where the reverse scan performs better than the forward scan.

2.6.1. Parameters affecting hysteresis

Hysteresis depends on various conditions, such as light soaking, voltage bias prior to the measurement and the scan rate [43]. Also the scan direction plays an important role. Forward-reverse and reverse-forward scans show qualitatively different behaviors [14].

Typically, devices with a normal (n-i-p) architecture display most hysteresis [84], whereas hysteresis is alliviated for inverted (p-i-n) architectures and mesoporous TiO_2-based devices. Also the crystal size of $MAPbI_3$ is found to influence current-voltage hysteresis, which becomes less severe as the crystal size increases [85].

Hysteresis is present at commonly used scan rates between 1 mV s^{-1} and 100 mV s^{-1} [45]. This is in strong contrast to other technologies. For example, hysteresis is also observed silicon solar cells, but this occurs at much higher scan rates between 15 V s^{-1} and 300 V s^{-1} [29]. For PSCs two trends are reported concerning the scan rate. Snaith et al. [29] observed that the magnitude of the hysteretic effect reduces with decreasing scan rate, getting more and more severe as the scan rate is slowed from 0.3 V s^{-1} to 0.011 V s^{-1}. On the contrary, Dualeh et al. [86] reported an opposite trend when the scan rate is reduces from 0.2 V s^{-1} to 0.01 V s^{-1}. More extensive research revealed that hysteresis first becomes more and more extreme with increasing scan rate, to diminish again when the scan rate is increased further [45]. For very high scan rates another type of hysteresis can be observed, related to displacements currents. Depending on the device architecture and fabrication processes, pronounced hysteresis occurs at different timescales [29, 87]. This also means that even supposedly hysteresis-free device can have hysteresis that is simply not observed at typical scanning rates.

2.7. Origin of hysteresis

There is still debate about the origin of hysteresis in the current-voltage curve. The rate-dependent hysteresis is most likely attributed to the perovskite material and not to any parasitic effects in the ETL or HTL, as the phenomenon is observed for a wide variety of device architectures with different ETLs and with or without HTL [45]. Several explanations have been proposed: ion migration, ferroelectric polarization, capacitive effects and charge trapping/de-trapping.

There is experimental evidence that the cause of hysteresis in the J-V curve lies in the formation of interfacial charge at the interfaces [88]. Weber et al. developed a time-resolved method based on Kelvin probe force microscopy to measure the local contact potential difference (CPD) as a function of time and position in a PSC with a conventional (n-i-p) architecture. They applied a voltage pulse of $-0.5\,\mathrm{V}$ for 750 ms to the FTO electrode while the gold electrode was grounded and measured the CPD. This simulates a forward scan (when the pulse is applied) and a backward scan (after the the pulse is turned off again). The static CPD map was then subtracted from the CPD maps at later times to analyse the transient charge distribution. Figure 2.10 shows the ΔCPD map after switching on the voltage pulse. Using Gauss's law one can quantify the charge at different positions from this map. The localized charges are indicated in Figure 2.10 with red (positive) and blue (negative) shaded areas.

The sharp potential step at the perovskite/ETL interface indicates a clear dipolar charge distribution with positive charges on the perovskite side and negative charges on the SnO_2/FTO side. The formation of this charge happens mainly within 10 ms, but it takes hundreds of millisecond to fully stabilize. After switching off the voltage pulse (not shown in Figure 2.10) these interfacial charges were stable for over 500 ms. All in all, these results show that the formation and release of interfacial charges is the dominating factor for hysteresis in the J-V curve.

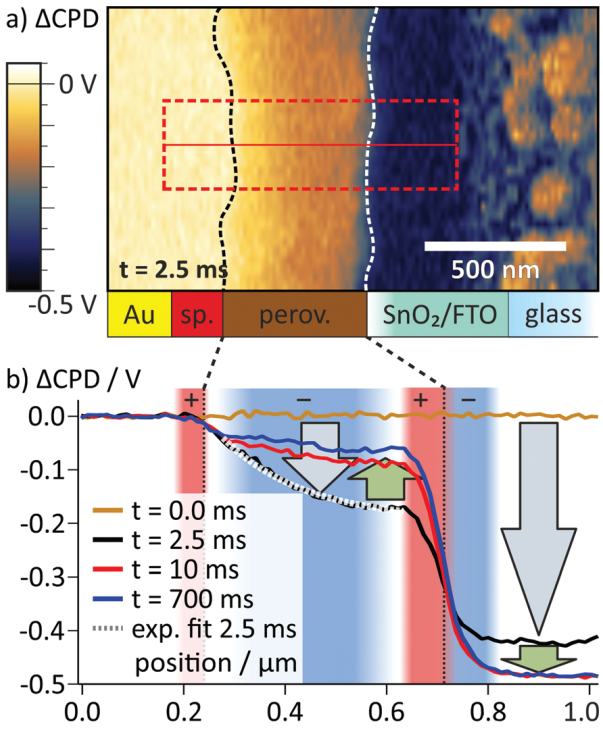

Figure 2.10: Cross-section of a PSC after switching on a voltage pulse of $-0.5\,\mathrm{V}$ to the FTO electrode. From left to right: gold (Au), Spiro-OmeTAD HTL (sp.), perovskite (perov.), SnO_2 ETL, FTO and glass. (a) ΔCPD map 2.5 ms after switching. (b) Averaged ΔCPD sections from the rectangular area marked in a at different times after turning on the voltage pulse. This image is adapted (in edited format) from Weber et al. [88].

2.7.1. Charge trapping/detrapping

Near the surface of the material perovskites can have large defect densities [70]. These defects could act as traps for electrons or holes. It was suggested that the defects fill under forward bias and that they are emptied under short-circuit conditions, resulting in a reduced charge-collection efficiency until they are filled again [28, 29]. Slow filling and emptying would then cause hysteresis in the J-V curve. Furthermore, it would be consistent with results from Dualeh et al., where a slow component in the current and voltage decay was observed [86]. If this is the relevant mechanism, the absence of hysteresis at very low and high scan rates is simply because the filling and/or emptying occurs at a much higher or slower rate than the scan rate. Because timescales for trapping and detrapping are likely to depend on the device architecture and fabrication process, this would also explain why most severe hysteresis is observed at different scan rates for different devices [29].

2.7.2. Ion migration

Ion migration has been proposed as a possible cause of hysteresis in perovskite solar cells. Excess ions may be present in the perovskite crystal as interstitial defects and move slowly through the layer [29]. Under short circuit conditions mobile ions accumulate at the interface, screening the applied potential and thus improving charge collection. Experiments have shown that perovskites indeed exhibit high ionic conductivity caused by the migration of halide-ions [89]. Density functional theory calculations on $CH_3NH_3PbI_3$ suggest that I^- anions and MA^+ cations diffuse via vacancy assisted migration with diffusion coefficients of $10^{-12}\,cm^2\,s^{-1}$ and $10^{-16}\,cm^2\,s^{-1}$ respectively [90]. Moreover, it has been observed that halide ions in $CH_3NH_3PbI_{3-x}Cl_x$ are not distributed homogeneously within the perovskite layer and that their spatial profile depends on the applied bias. Several modeling efforts have been successful to reproduce hysteresis using mobile ions [27, 30, 91].

2.7.3. Displacement currents

Both carrier (de)trapping and ion migration would give rise to displacement currents in semiconductor devices, possibly causing hysteresis in the J-V curve. An adjustment of the applied bias distorts the equilibrium and an additional flow of electrons will arise as a result of filling and/or emptying defects or ionic movements. Displacements currents occur in all semiconductor devices and can for example be observed in the junction capacitance or diffusion capacitance of a pn-junction. However, displacements currents cannot explain hysteresis adequately. A rough estimation based on the amount of charge that would cause the bump in the J-V curve shows that the capacitance at 1 V applied bias would have to be larger than $10\,mF\,cm^{-2}$, whereas the geometric capacitance is in the range of $\mu F\,cm^{-2}$ [45]. This would mean that there is an unrealistically high charge concentration of $10^{22}\,cm^{-3}$ for a 200 nm thick layer. Therefore, displacement currents can be ruled out as the origin of hysteresis at low scan rates.

2.7.4. Ferroelectric polarization

It has been proposed that ferroelectric polarization might play a role in perovskites. Ferroelectricity is a property of crystals that show spontaneous electric polarazition, which can be reversed in direction by an external electric field. Ion displacement or alignment of the dipole orientation of the organic cation could induce this in perovskites [68]. However, it has been shown using piezoelectric force microscopy that such effects only persist for short timescales [68] and the frequency response that is measured using impedance spectroscopy is considered uncharacteristic for well-known perovskite ferroelectrics [92]. Moreover, devices made of the inorganic $CsPbI_3$ perovsite, that cannot be a ferroelectric material, and the nonferroelectric semiconductor PbI_2 also display hysteresis [84, 93]. So ferroelectricity is probably not cause of hysteresis.

2.8. Evaluating hysteresis

To quantify the magnitude of the hysteresis effect it is useful to define a Hysteresis Index (HI). Several definitions were already proposed, based on the difference in current between the forward and reverse scan at a given bias (see e.g. Sanchez et al. [94], Kim and Park [85] and Rong et al. [83]) or the difference in maximum power output (see e.g. Calado et al. [95]). A disadvantage of these definitions is that the quantity depends on the chosen bias, which is usually chosen between $V_{OC}/2$ and $0.8V_{OC}$, making it more difficult to compare different samples. A better way to take into account the entire voltage sweep is by using an integral measure. We adopt the definition from Nemnes et al. [14]:

$$HI = \frac{\int_0^{V_{OC,\,RS}} J_{RS}(V)\,\mathrm{d}V - \int_0^{V_{OC,\,FS}} J_{FS}(V)\,\mathrm{d}V}{\int_0^{V_{OC,\,RS}} J_{RS}(V)\,\mathrm{d}V + \int_0^{V_{OC,\,FS}} J_{FS}(V)\,\mathrm{d}V} \tag{2.26}$$

It is clear that $-1 < HI < 1$, with positive values corresponding to normal hysteresis and negative values corresponding to inverted hysteresis. Larger values of $|HI|$ correspond to stronger hysteresis. Our definition differs slightly from the one used by Lee et al. [96] in the choice of the denominator. This choice ensures a more balanced evaluation of both normal and inverted hysteresis. Note that the hysteresis index has no direct physical meaning, but is mainly intended to easily compare different cases.

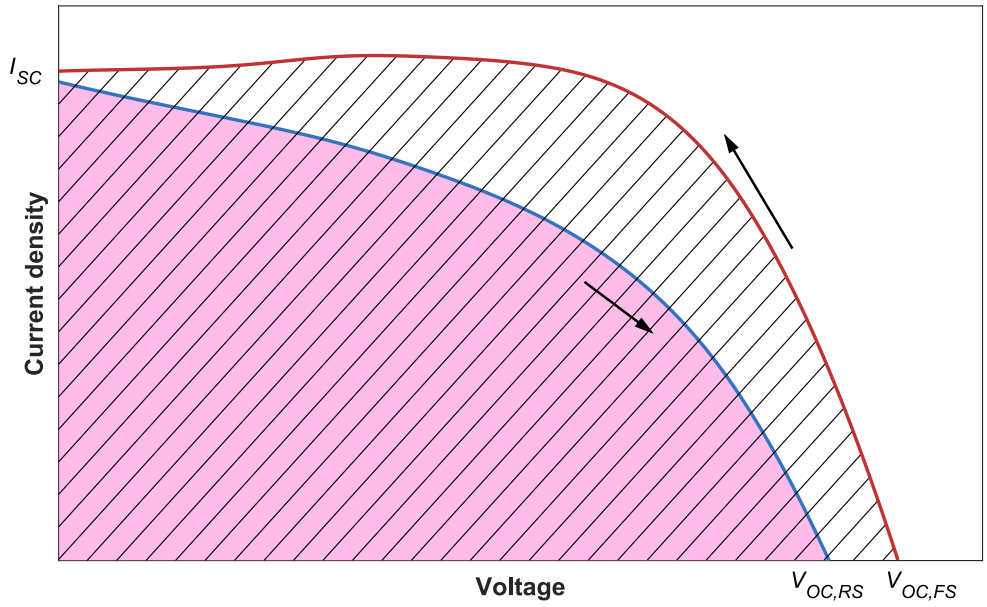

Figure 2.11: Illustration of the Hysteresis Index. The open circuit voltages for reverse scan and forward scan are indicated with $V_{OC,\,RS}$ and $V_{OC,\,FS}$ respectively. Also the short circuit current (I_{SC}) is indicated, although this slightly differs between both scans. The shaded areas (blue and hatched) represent the integrals in equation (2.26). The HI is defined as the fraction of the difference between the shaded areas and the sum of the shaded areas.

3

Methodology

This study consists of three parts: (i) exploring the defect properties that affect hysteresis, (ii) building an understanding of the phenomena that appear in the simulations, and (iii) developing and analysing a realistic model in accordance with experimental observations and DFT calculations.

The ultimate goal is to build a model to simulate any perovskite device as accurately as possible. However, such a task is challenging not only due to complexity of the models that demand high computational effort, but also because it is difficult to obtain values of parameters such as defect densities from experiments [95, 97]. Our device model is based on the results of extensive research carried out by different groups [98–111].

In a preliminary study we reproduced band diagrams and J-V curves from related simulation studies done by Wager [76], Yue et al. [47] and Neukom et al. [27]. This thesis describes the simulation of perovskite solar cells showing hysteresis due to slow defects.

As a starting point for our realistic model we use a planar n-i-p architecture consisting of relatively well known materials. This is easier to model than a mesoporous device. It also does not require a mechanism that describes the inter-band transfer between the TCO and HTL (necessary for p-i-n structures). The latter requires additional models, for example an interface hopping model [112]. This would introduce uncertainty in the results due to extra parameters and complicate our search for responsible defects. In chapter 2 we already mentioned that in general this also architecture displays the most severe hysteresis.

3.1. Simulation setup

The simulation model we use in this study is implemented in Synopsys Sentaurus (version 2015.6). Sentaurus is an industry-standard suite of TCAD tools that can be used to simulate the operation of semiconductor devices. The device structure is generated using Sentaurus Structure Editor (SDE). Sentaurus uses numerical discretization schemes to solve the mathematical models inside the device. This requires that the geometric space is subdivided into discrete geometric cells, which we call mesh generation. Sentaurus has an advanced built-in mesh generator that allows the user to generate a mesh that can be locally refined. We only have to refine the mesh close to interfaces, because generally in semiconductors the largest gradients (e.g. in the electron/hole density) occur close to interfaces.

The actual device simulation is performed in Sentaurus Device. This tool is capable of self-consistent optical, thermal and electrical simulations. It uses a Newton-like solver to solve the semiconductor equations introduced in section 2.1.3 with the appropriate boundary conditions. Generation and recombination are computed using additional models. We use the transfer-matrix method to compute the optical generation inside the device and multiple recombination models. Sentaurus device also computes thermionic emission and tunneling at material interfaces. To model the occupation dynamics of defects we use models that are already adapted in Sentaurus Device extended with new C++ functions to define a spatial density profile.

Transient time simulations are an essential part of our study to emulate the scan-rate dependent J-V curves. Implicit discretization methods are used to solve the time-dependent semiconductor equations. Next to this, we perform steady-state (or quasi-stationary) simulations. In a steady-state simulation the

device is assumed to be in equilibrium, i.e. at every point inside the device all quantities are constant over time. The steady-state solution is important, because it is the long-term response of the system.

Figure 3.1 shows the simulation workflow. The meshed geometry and parameter files are generated by Sentaurus Device Editor (SDE). Sentaurus Device (SDEVICE) performs the device simulations for this device structure. Sentaurus Visual (SVISUAL) is used to inspect the results of individual simulations and eventually MATLAB is used for more advanced analyses. It is quite common that simulation failures must be resolved manually by reconsidering the mesh, model parameters or numerical methods. We routinely use Sentaurus Visual to check if the models and mesh behave as expected.

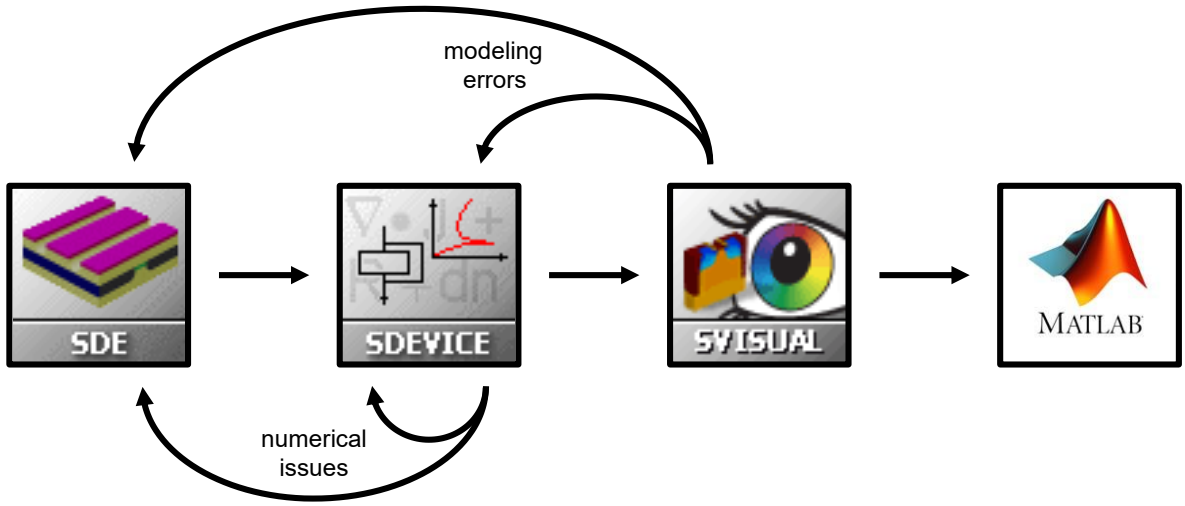

Figure 3.1: Schematic representation of the simulation workflow.

3.2. Device structure

Our device model is based on a typical n-i-p device architecture (see Figure 1.5a in chapter 1). The archetypal perovskite $MAPbI_3$ is used for the absorber layer, the ETL consists of compact TiO_2 and the HTL is made of spiro-OMeTAD. We use ITO as transparent conductive oxide instead of the more commonly used FTO, because of the lack of information of FTO parameters. Also, there is no indication that the TCO affects current-voltage hysteresis. The simulation parameters for ITO result from earlier simulation studies in our group and have been carefully verified before. All other simulation parameters are obtained from literature, whereby an attempt has been made to compare different sources. The values are summarized in table 3.1.

Table 3.1: Material and device parameters of the PSC. ϵ_r is the relative permittivity, E_G is the bandgap energy, χ is the electron affinity, N_C is the effective density of states of the conduction band, N_V is the effective density of states of the valence band, N_D the concentration of ionized donors, N_A is the concentration of ionized acceptors, μ_n is the electron mobility and μ_p is the hole mobility.

	ITO	TiO_2	$CH_3NH_3PbI_3$	spiro-OMeTAD
Thickness (nm)	300	50	400	200
ε_r	3.5	60 [98]	30 [99]	3 [100]
E_G (eV)	3.1	3.2 [103]	1.5 [101]	3.0 [102]
χ (eV)	4.7	4 [103]	3.9 [101]	2.2 [104]
N_C (cm^{-3})	4.1×10^{18}	1×10^{21} [103]	2×10^{18} [109]	1×10^{18} [103]
N_V (cm^{-3})	1.7×10^{19}	2×10^{20} [103]	2×10^{19} [109]	1×10^{20} [103]
N_D (cm^{-3})	1×10^{20}	5×10^{17} [105]	0	0
N_A (cm^{-3})	0	0	0	3×10^{18} [106]
μ_n ($cm^2\,V^{-1}\,s^{-1}$)	160	6×10^{-3} [103]	0.7 [107]	1×10^{-4} [108]
μ_p ($cm^2\,V^{-1}\,s^{-1}$)	40	6×10^{-3} [103]	0.4 [107]	1×10^{-4} [108]

Figure 3.2 shows the device structure and mesh of our simulated cells. We only made full 2D simulations to analyses specific cells where we did not vary parameters. To save computational time, one-dimensional simulations have been used for all other experiments. For the one-dimensional case we used the same layer stack, but assumed the top contact to be transparent. We observed a slightly reduced current for the 2D simulations in comparison with the 1D case, which can mainly be ascribed to the lateral resistance in the TCO. Nevertheless, no clear difference in hysteresis was observed at any point between 2D simulations and 1D simulations.

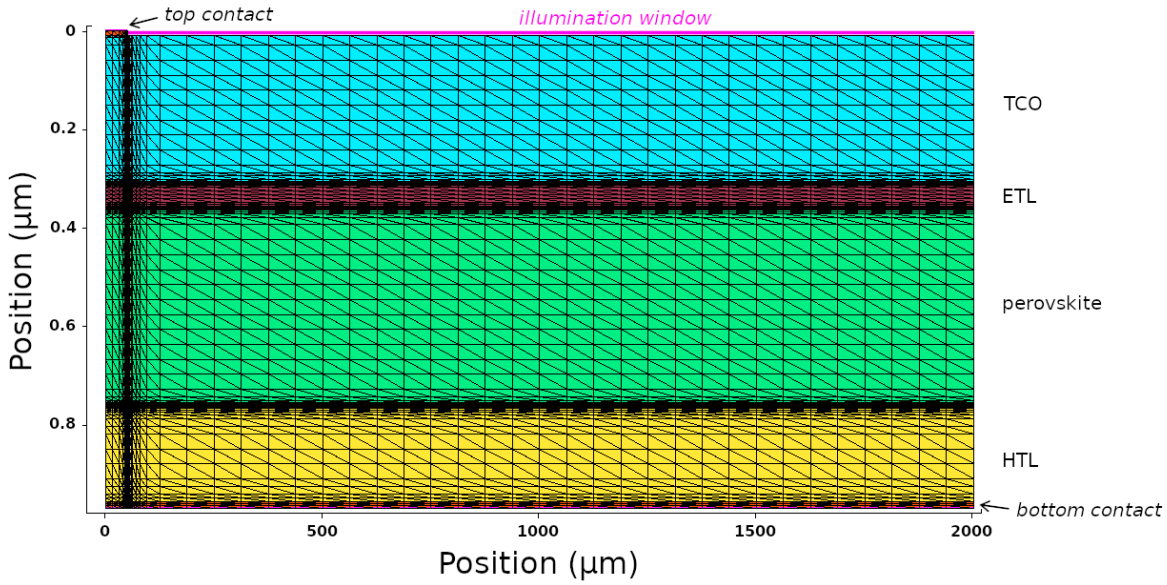

Figure 3.2: Device structure and mesh used for 2D simulations. Note that the axis have different scales: the layer stack is much thinner than it extents in perpendicular directions.

3.2.1. Validation of parameters

We have used preliminary simulations with various defect distributions to analyse the sensitivity of all parameters. We found that variations in the electron affinity, bandgap and Fermi level are most important. Similar architectures and parameters were previously successfully used by others (e.g. Minemoto and Murata [109], Liu et al. [103], Wu et al. [110] and Alnuaimi et al. [111]). So the simulation is based on realistic models and thus revealing realistic trends. In addition, we found reasonable agreement between the effective density of states and the density of states measured by Tao et al. [3]. Nevertheless, we have to be careful in treating quantitative results because our parameters have not been verified with real devices.

A wide range of values for carrier mobilities in perovskites is reported in literature. A literature overview of charge carrier mobilities can be found in [113]. The considerable variation in reported values could arise from differences in morphologies (thin film, mesoscopic, single crystal, etc.), fabrication processes and of course the composition of the material. However, it is more likely that the variations should be ascribed to systematic and statistical errors from different measurement techniques. For thin film MAPI (solution processed) values between 0.4 $cm^2\,V^{-1}\,s^{-1}$ and 71 $cm^2\,V^{-1}\,s^{-1}$ for the electron and hole mobility have been reported. For our simulations we use an estimation based on the work of Stranks et al., where the diffusion coefficient of MAPI is estimated from fits to photoluminescence decays. An estimate for the electron and hole mobilities is obtained with Einsteins relation.

3.3. Optical simulation

Various methods can be used to compute the optical generation in devices. In Sentaurus the transfer-matrix method, simple optical beam absorption, the raytracing method and finite-difference time-domain and beam propagation method are implemented [114]. We use the transfer-matrix method, which is commonly used for multi layer systems consisting of different thin films. For every wavelength in the input spectrum and every location inside the absorption needs to be computed. Assuming that every absorbed photon creates one electron-hole pair, this then gives the optical generation inside the device.

3.3.1. Transfer Matrix Method

The transfer-matrix method can be used to calculate the optical carrier generation rate for monochromatic plane waves penetrating a number of planar, parallel layers. We assume that each layers is homogeneous, isotropic and optically linear. An illumination window is used to confine the light that is incident on the surface. This is indicated in Figure 3.2 and covers the entire film except for the metal top contact.

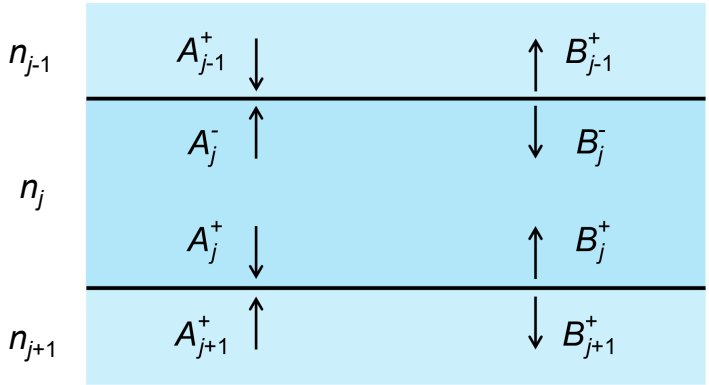

Figure 3.3: Schematic representation of the transfer matrix method. Each layer has an outgoing and incoming wave on the top interface (indicated with a − sign) and an outgoing and incoming wave on the bottom interface (indicated with a + sign). The amplitude of the outgoing wave is denoted by A and the amplitude of the incoming wave is denoted by B.

The outgoing and incoming waves on both sides of an interface are related by

$$\begin{pmatrix} B_j^+ \\ A_j^+ \end{pmatrix} = T_{j,j+1} \begin{pmatrix} A_{j+1}^- \\ B_{j+1}^- \end{pmatrix} \tag{3.1}$$

where $T_{j,j+1}$ is the transfer matrix that can be derived from the Fresnel equations and is given by

$$T_{j,j+1} = \frac{1}{2Z_j} \begin{pmatrix} Z_j + Z_{j+1} & Z_j - Z_{j+1} \\ Z_j - Z_{j+1} & Z_j + Z_{j+1} \end{pmatrix} \tag{3.2}$$

with the complex wave impedance $Z_j = n_j \cos\theta_j$ for TE polarized waves and $Z_j = n_j / \cos\theta_j$ for TM polarized waves. Here λ is the wavelength of the incident light, θ_j the complex counterpart of the angle of refraction, d_j the thickness and n_j the refractive index of layer j. Propagation through layer j is described by the transfer matrix

$$T_j(d_j) = \begin{pmatrix} \exp\left(2\pi i n_j \cos\theta_j \frac{d_j}{\lambda}\right) & 0 \\ 0 & \exp\left(-2\pi i n_j \cos\theta_j \frac{d_j}{\lambda}\right) \end{pmatrix} \tag{3.3}$$

This relates the waves on both ends of a layer:

$$\begin{pmatrix} A_j^- \\ B_j^- \end{pmatrix} = T_j(d_j) \begin{pmatrix} B_j^+ \\ A_j^+ \end{pmatrix} \tag{3.4}$$

The intensity of both the TM and TE wave in layer j at a distance x from the interface between layers j and $j+1$ is given by

$$I(x) = \frac{\Re(Z_j)}{\Re(Z_0)} \cdot \left\| T_j(x) \begin{pmatrix} A_j^- \\ B_j^- \end{pmatrix} \right\|^2 \tag{3.5}$$

The total intensity is then the sum of both the TM and TE part.

3.4. Modeling of defects

We consider two types of defects in our model: acceptor-like defects and donor-like defects. Acceptor-like defects are uncharged when they are empty and negatively charged when they are occupied by an electron. These defects are also known as electron traps. In contrast, donor-like defects or hole traps are uncharged when they contain an electron and are positively charged when they are empty.

Accurately modeling the effect of defects in semiconductor devices is a complex task. Reported measurement results across different laboratories have varied widely and do not agree in the observed activation energies and there is ambiguity in whether these defects are donor- or acceptor-like [68, 69].

Several different defect distributions are used in our simulations. First, we simulate cells where defects with a distinct defect energy are embedded in the perovskite layer to identify in which range of defect energies defects cause J-V hysteresis. Secondly, we study the band tail states (see section 3.4.1). Finally, we use a novel approach to model realistic defect distributions that successfully reproduces hysteresis in the J-V curve (see section 3.4.2).

3.4.1. Band tail states

We use an expression for the band tail states density based on a model by Wager [76]. To this end, a conduction band mobility edge E_{CME} is introduced, which distinguishes localized tail states from extended states in the conduction band by their energy. Note that the conduction band mobility edge is not equal to the conduction band edge E_{C}, which can be seen in Figure 2.7. Likewise, there is a valence band mobility edge E_{VME} that distinguishes the valence band from the valence band tail states.

The conduction band tail states are acceptor-like and their density (in $\mathrm{cm^{-3}\,eV^{-1}}$) is given by

$$g_{\mathrm{TC}} = N_{\mathrm{TC}} \exp\left(\frac{E - E_{\mathrm{CME}}}{W_{\mathrm{C}}}\right) \tag{3.6}$$

where N_{TC} is given by

$$N_{\mathrm{TC}} = \frac{1}{2\pi^2}\left(\frac{2m_e^*}{\hbar^2}\right)^{3/2}\sqrt{\frac{W_C}{2}} = 4.9 \times 10^{21} \cdot \sqrt{W_{\mathrm{C}}} \cdot \left(\frac{m_e^*}{m_0}\right)^{3/2} \tag{3.7}$$

Here W_{C} is the characteristic energy of the conduction band tail states in eV and m_e^*/m_0 is the unitless electron effective mass associated with electrons in the conduction band. Analogously, the valence band tail state are donor-like and their density (in $\mathrm{cm^{-3}\,eV^{-1}}$) is given by

$$g_{\mathrm{TV}} = N_{\mathrm{TV}} \exp\left(\frac{E_{\mathrm{VME}} - E}{W_{\mathrm{V}}}\right) = 4.9 \times 10^{21} \cdot \sqrt{W_{\mathrm{V}}} \cdot \left(\frac{m_e^*}{m_0}\right)^{3/2} \exp\left(\frac{E_{\mathrm{VME}} - E}{W_{\mathrm{V}}}\right) \tag{3.8}$$

3.4.2. Deep-level defects

We use a novel approach to model the spatial distribution of defects. This is based on the results from Ni et al. [70] that are described in section 2.5.2. These measurements show a clear decrease in defect density with distance from the interface. We model this using an exponential function, which seems a good approximation close to the interface. How far the interface defects extent into the bulk is parameterized with penetration depths δ_{ETL} and δ_{HTL}. The defect density per unit volume is given by

$$N_{\mathrm{t}} = N_{\mathrm{t,ETL}} \exp\left(\frac{x_{\mathrm{ETL}} - x}{\delta_{\mathrm{ETL}}}\right) + N_{\mathrm{t,bulk}} + N_{\mathrm{t,HTL}} \exp\left(\frac{x - x_{\mathrm{HTL}}}{\delta_{\mathrm{HTL}}}\right) \tag{3.9}$$

with $N_{\mathrm{t,ETL}}$ and $N_{\mathrm{t,HTL}}$ the defect densities at the ETL/perovskite and HTL/perovskite interfaces, x_{ETL} and x_{HTL} the positions of the respective interfaces and $N_{\mathrm{t,bulk}}$ the bulk defect density. In conformity with the measurements from Ni et al. [70], we assume that $N_{\mathrm{t,HTL}} = 10^{18}\,\mathrm{cm^{-3}}$ and $N_{\mathrm{t,bulk}} = 10^{15}\,\mathrm{cm^{-3}}$. Based on the outcomes in chapter 5, we assume a relatively high defect density near the ETL, namely $N_{\mathrm{t,ETL}} = 10^{19}\,\mathrm{cm^{-3}}$. Figure 3.4 shows the spatial profile that we use in our simulations.

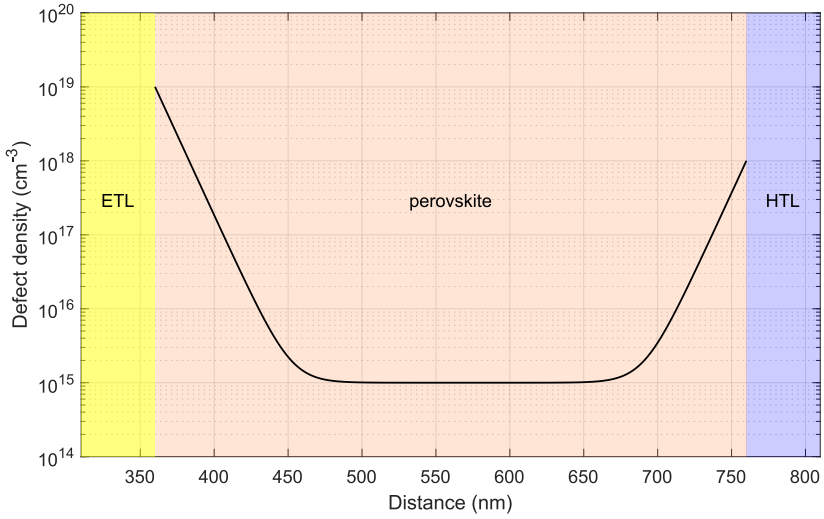

Figure 3.4: Spatial defect distribution used for simulations. The corresponding parameters are given in Table 3.2.

The energetic defect density profile is modeled using a Gaussian distribution:

$$N_t = N_{t,0} \exp\left(-\frac{(E - E_0)^2}{2E_S^2}\right) \tag{3.10}$$

Here $N_{t,0}$ is the maximum defect density, E_0 the average defect energy and E_S the standard deviation of the Gaussian distribution. Our literature review revealed evidence for the existence of defects with transition energies around 0.15-0.30 eV (see also section 6.5 in chapter 6) [115–117]. Based on this review and the outcomes from chapter 5, we assume that the defects are acceptor-like with $E_{t,0} = 0.25$ eV. The model parameters are summarized in table 3.2.

Figure 3.5 shows how our simplified model compares to a typical defect energy distribution measured by Duan et al. [115]. With only this Gaussian approximation we clearly fail to account for the deeper defects shown in Figure 3.5a. However, in chapter 5 we will show that their contribution to hysteresis is limited.

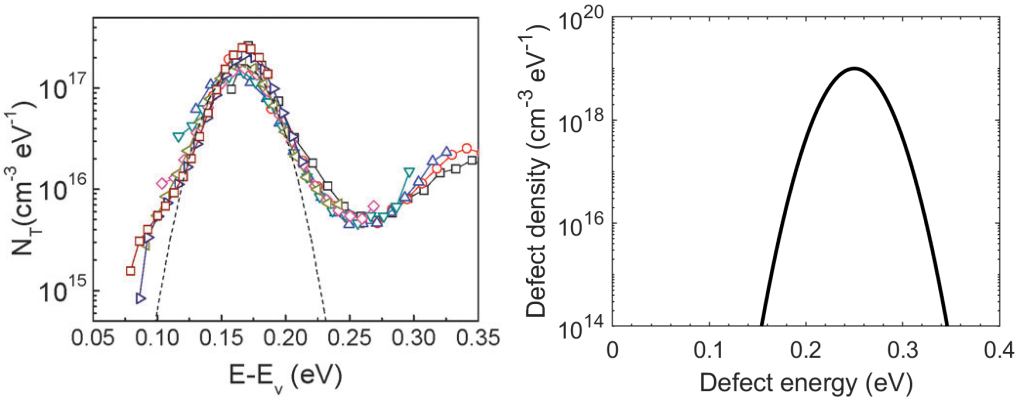

(a) Measurements. (b) Simulation input.

Figure 3.5: (a) Measured defect energy distribution of $MAPbI_3$ including a Gaussian fit to the data (shown as a dashed curve). Adapted from Duan et al. [115] with permission from The Royal Society of Chemistry. (b) Examplary defect energy distribution used for simulations. Shown is the distribution close to the ETL/perovskite interface for $N_{t,ETL} = 10^{19}$ cm^{-3} eV^{-1} and $E_S = 20$ meV.

Table 3.2: Default parameters used for the slow defects. Unless stated otherwise, these parameters are used for all simulations with our spatially resolved defect model.

Parameter	Value	Unit	Description
$E_{t,o}$	0.25	eV	Average defect energy of Gaussian distribution
E_S	20	meV	Standard deviation of Gaussian distribution
$N_{t,ETL}$	1×10^{19}	cm^{-3} eV^{-1}	Defect density at ETL/perovskite interface
$N_{t,HTL}$	1×10^{18}	cm^{-3} eV^{-1}	Defect density at HTL/perovskite interface
$N_{t,bulk}$	1×10^{15}	cm^{-3} eV^{-1}	Bulk defect density
δ_{ETL}	100	nm	ETL interface defect depth
δ_{HTL}	100	nm	HTL interface defect depth
σ_n	1×10^{-23}	cm^2 s^{-1}	Electron capture cross-section
σ_p	1×10^{-23}	cm^2 s^{-1}	Hole capture cross-section

3.4.3. Carrier trapping

Carrier trapping and detrapping by defects is modeled using the theory described in section 2.2. To study the effect of capture and emisison rates, the capture cross-sections are varied. The thermal velocity, which also appears in equations (2.16) and (2.17), is a material property and for modeling purposes its effect can be incorporated in the capture cross-section as well. There are no reported values of the thermal velocities in perovskites, so we use default values from Sentaurus.

3.5. Recombination

Next to trap-assisted recombination, Auger recombination and radiative recombination are implemented for the $MAPbI_3$ absorber layer (see section 2.3). The corresponding parameters are summarized in table 3.3.

Results from van Reenen et al. already revealed that trap-assisted recombination at the interface plays a key role in the emergence of current-voltage hysteresis [91]. Because we have not enough data to model all defects explicitly, we use the following SRH recombination model at interfaces to account for surface recombination:

$$R_{\text{SRH,surf}} = \frac{np - n_i^2}{\left(n + n_i \exp\left(\frac{E_{\text{trap}}}{kT}\right)\right)/s_p + \left(p + n_i \exp\left(\frac{-E_{\text{trap}}}{kT}\right)\right)/s_n} \tag{3.11}$$

with n_i the intrinsic carrier density, E_{trap} the defect energy and s_p and s_n the surface recombination velocities for holes and electrons respectively.

Table 3.3: Parameters used for carrier recombination models.

Parameter	Value	Unit	Description
β	1×10^{-10}	$\text{cm}^3\,\text{s}^{-1}$	Radiative recombination
C_n	1×10^{-28}	$\text{cm}^6\,\text{s}^{-1}$	Auger recombination (eeh)
C_p	1×10^{-28}	$\text{cm}^6\,\text{s}^{-1}$	Auger recombination (ehh)
s_n	1×10^{3}	$\text{cm}\,\text{s}^{-1}$	Surface recombination velocity for electrons
s_p	1×10^{3}	$\text{cm}\,\text{s}^{-1}$	Surface recombination velocity for holes

3.6. Transient simulations

All scans are performed from 1.1 V until −0.2 V. The reverse scan is immediately followed by the forward scan starts, without any delay.

3.7. Model validation

To validate that our simulations mimic real perovskite solar cells, we reproduced band diagrams and J-V curves without slow defects incorporated in the perovskite layer. Figure 3.6 shows the band diagram of the simulated PSC in the dark with no applied bias. The band diagram of the same cell under illumination in V_{OC} is shown in Figure 3.7. The device has an open circuit voltage $V_{\text{OC}} = 1.0\,\text{V}$, a short circuit current $J_{\text{SC}} = 19.0\,\text{A}\,\text{cm}^{-2}$ and a fill factor FF = 0.67. The band diagrams are as expected from the theoretical background (see section 2.4). The output parameters are comparable to those of PSCs showing hysteresis [29, 110].

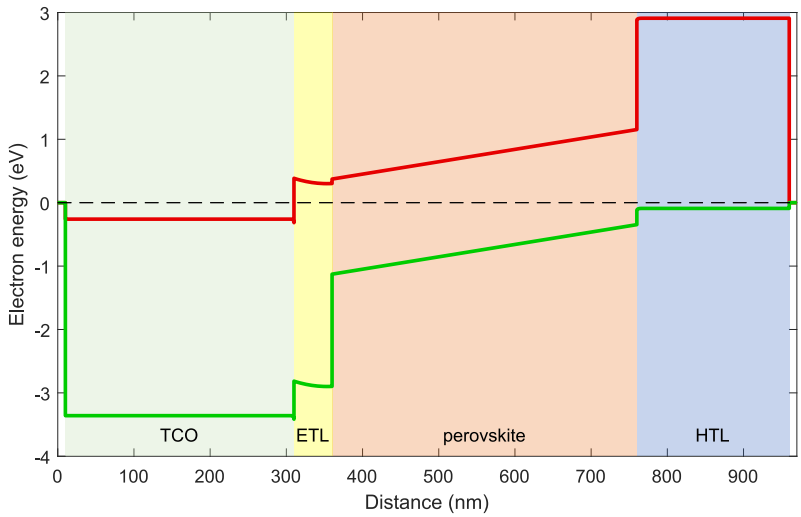

Figure 3.6: Band diagram of a perovskite solar cell in the dark with no applied bias. The red and green lines denote the conduction band edge and the valence band edge respectively. The Fermi-level is shown as a dashed line.

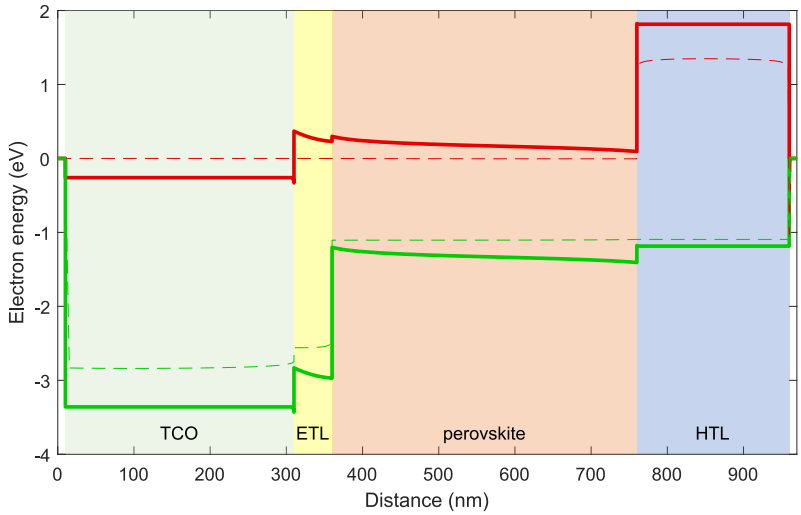

Figure 3.7: Band diagram of a perovskite solar cell under illumination in V_{OC}. The red and green lines denote the conduction band edge and the valence band edge respectively. The conduction and valence band quasi-Fermi levels are indicated by a red and green dashed line respectively.

4

Governing physical effects

In this chapter we describe the governing physical effects that explain hysteresis as it is observed in our simulations (see also chapter 6). Hysteresis can be explained by either improvement or reduction of the carrier extraction efficiency from the absorber layer to the ETL and HTL. During one of the scans carrier transport is hindered by trapped charge close to the interfaces. From simulating cells with and without accumulated charge (using both negative and positive charge, and different concentrations), we found charge accumulation near the interface to be detrimental to the device performance. Here, we highlight the most important reasons for this reduction in performance.

4.1. Charge polarisation

Figure 4.1a shows the space charge as a function of position inside the device, when positive is trapped in the perovskite layer near the ETL interface. The trapped charge itself is clearly visible in Figure 4.1a as a positive peak of space charge in the perovskite layer. The figure also shows that the space charge in adjacent layers changes in response to the trapped charge: negative charge accumulates in the ETL and the TCO layer. We thus have charge polarisation at the interface.

Figure 4.1b also shows the space charge as a function of position inside the device, but this time when negative is trapped in the perovskite layer near the ETL interface. Again, the trapped charge is clearly visible and the space charge in adjacent layers responds to this: positive charge accumulates in the TCO layer and the negative peak of space charge in the HTL disappears.

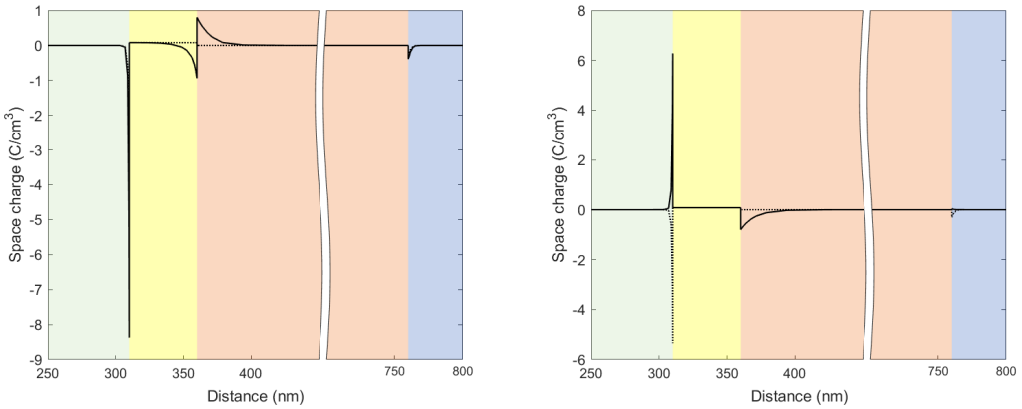

(a) Positive trapped charge.

(b) Negative trapped charge.

Figure 4.1: Distribution of space charge when (a) positive charge is trapped in the perovskite layer close to the ETL or (b) negative charge is trapped in the perovskite layer close to the ETL. For comparison, the space charge distribution in a device without trapped charge is indicated with a dashed line. From left to right: TCO (green) ETL (yellow), perovskite layer (red) and HTL (blue).

Now that we know how the space charge redistributes in response to charge accumulation, let us study

what the impact is on the operation of the device. Figure 4.2 shows the electrostatic potential as a function of position inside the device, corresponding to the space charge distributions from Figure 4.1. As we can see from the figure, accumulation of positive charge leads to a potential barrier close to the ETL (compare the solid profile with the dotted profile). This barrier hinders efficient extraction of electrons from the absorber layer to the ETL. This is of course detrimental to the device performance (see also section 4).

Also accumulation of negative charge is detrimental to the device performance. Figure 4.2 shows that accumulation of negative charge near the interface leads to a potential drop across the ETL (compare the dashed profile with the dotted profile). As a result, the built-in potential across the absorber layer is lowered. In a significant part of the absorber layer the slope of the dashed profile is relatively low (see Figure 4.2). This means that there is a relatively weak electric field. For efficient carrier extraction we actually want a strong electric field inside the absorber layer, pointing from the ETL to HTL. The weak electric field explains why we observe reduced device performance in the presence of negative charge accumulation near the interface.

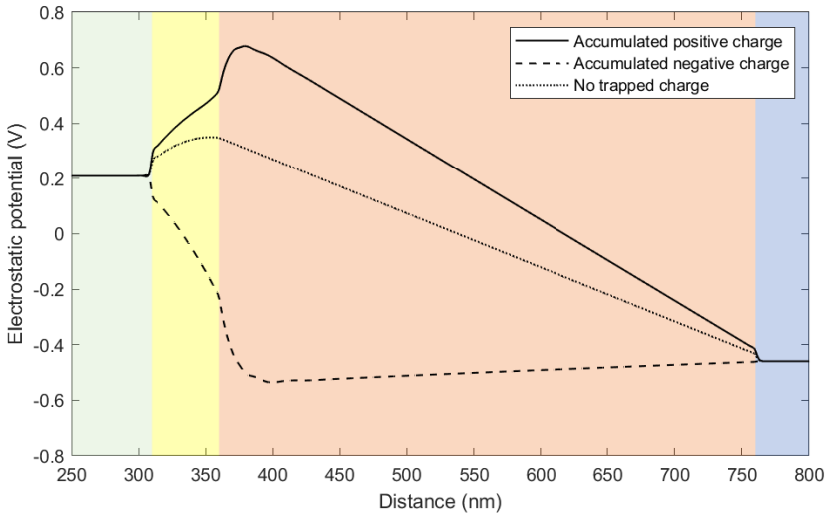

Figure 4.2: Electrostatic potential inside the device in thermal equilibrium when positive, negative or no charge is trapped in the perovskite layer (red) close to the ETL (yellow). The corresponding space charge distributions are shown in Figure 4.1. From left to right: TCO (green) ETL (yellow), perovskite layer (red) and HTL (blue).

In a similar way charge polarisation at the HTL/perovskite interface reduces the performance of the device. The corresponding space charge distributions and electrostatic potential are shown in Appendix B.

4.2. Steady state

In the previous section we have seen that charge polarisation at the interfaces is detrimental to the performance of the device. In this remainder of this chapter, we will illustrate how charge polarisation due to carrier trapping near the interfaces can cause hysteresis in the J-V curve. The key idea is that accumulated charge near the interface, which has been trapped when the device was reverse biased, is released very slowly. Consequently, during the forward scan there is significant charge polarisation and thus reduced performances compared to the reverse scan.

To understand the transient behaviour of PSCs, we first consider the behaviour of a simulated device in steady state. This device contains acceptor-like defects distributed according to the spatial profile shown in Figure 3.4 (chapter 3). All defect state properties are given in Table 3.2 (chapter 3).

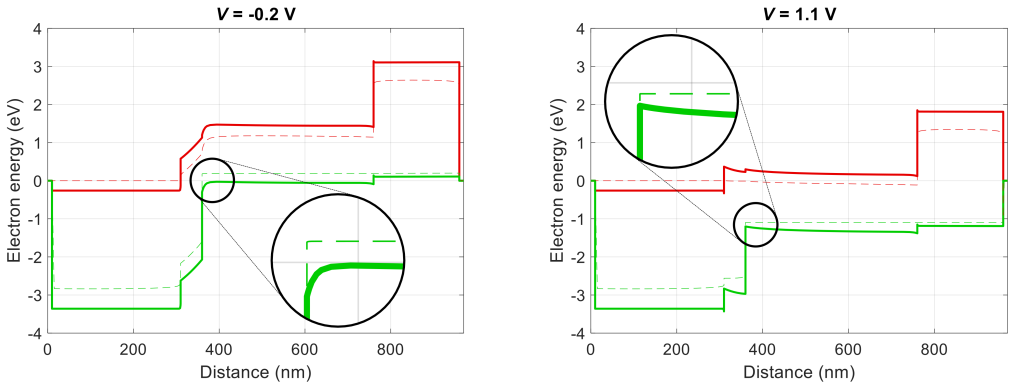

Figure 4.3: Band diagram in steady state when the device is (a) reverse biased ($V = -0.2\,\text{V}$) and (b) forward biased ($V = 1.1\,\text{V}$). The conduction band edge and the valence band edge are denoted with red and green lines respectively. Dashed lines indicate the conduction band (green) and valence band (red) quasi-Fermi levels.

Figure 4.3 shows the steady state band diagrams in reverse bias ($V = -0.2\,\text{V}$) and forward bias ($V = 1.1\,\text{V}$). For now, let us focus on the highlighted region. This region lies inside the perovskite layer, near the ETL. It can be seen in Figure 4.3a that the valence band quasi-Fermi level is closer to the VBE in this region than in the same region in Figure 4.3b. This means that the hole density is much higher in forward bias. This is due to holes being pushed towards the ETL when forward bias is applied. The holes are blocked by the ETL and they accumulate near the interface.
A similar effect can also be observed near the HTL. See chapter 5 for more details.

4.3. Electron trapping by defects

Now that we know that charge accumulates near the interface, let us study its effect on electron trapping by defects. Figure 4.4 shows the concentrations of trapped electrons during the forward and reverse scans. The profiles are shown in reverse bias ($V = -0.2\,\text{V}$), forward bias ($V = 1.1\,\text{V}$) and two biases in between ($V = 0.5\,\text{V}$ and $V = 0.8\,\text{V}$). Remind that the scan starts at $V = 1.1\,\text{V}$ (blue curve in Figure 4.4d), switches scan direction at $V = -0.2\,\text{V}$ (blue and red curve in Figure 4.4a) and ends at $V = 1.1\,\text{V}$ (red curve in Figure 4.4d).

The steady-state profiles are also included in Figure 4.4. Note that steady-state simulations are the long-term response of the system, as mentioned in chapter 3. Although steady state is usually not reached during a scan, it gives us a good indication of the tendency of carrier trapping. That is, the transient profiles follow the steady-state profile: if the profile is below steady state, it will increase and if it is above steady state, it will decrease.

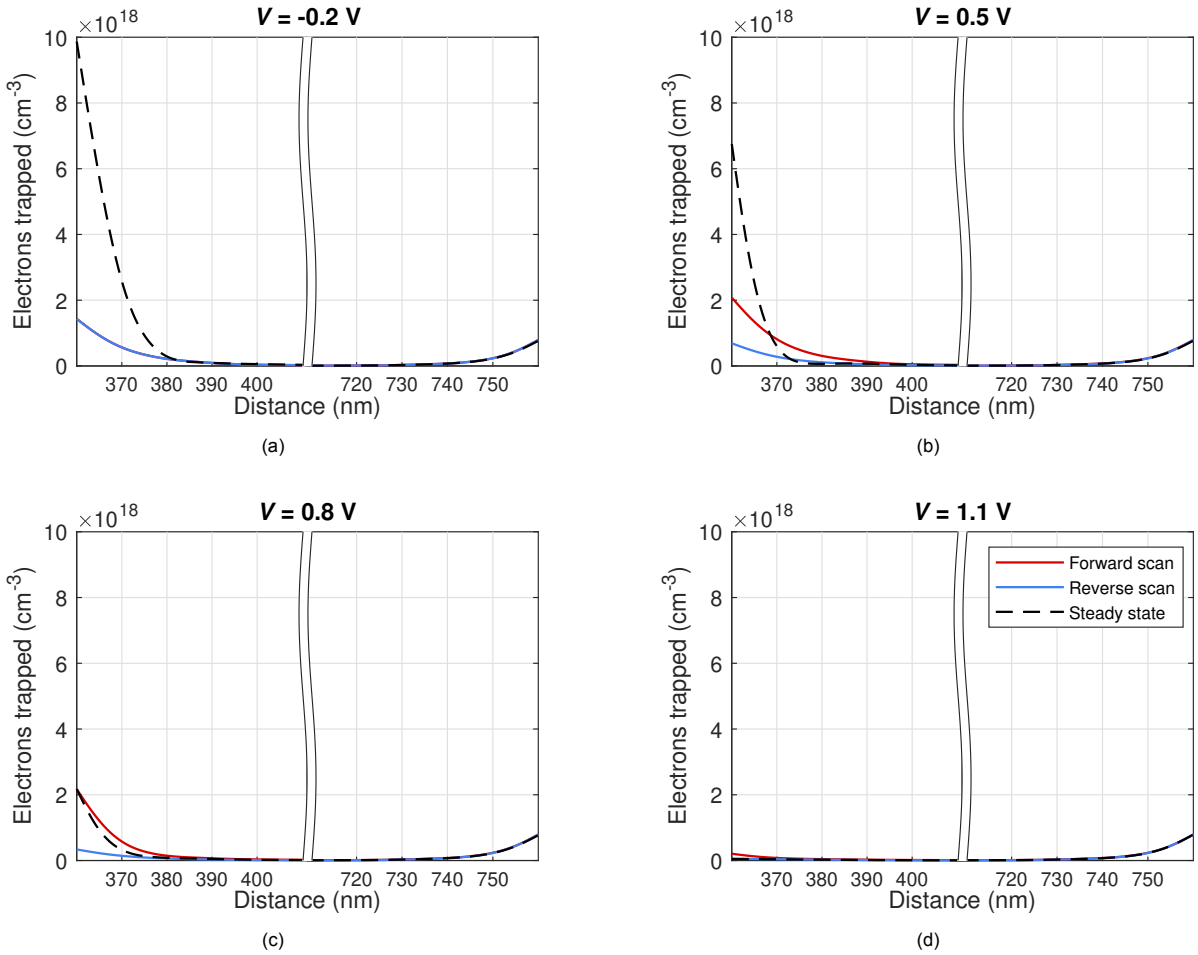

Figure 4.4: Profiles of trapped electrons in the perovskite layer as a function of position. The ETL/perovskite interface is at the left side and the HTL/perovskite interface is at the right side. The red and blue lines denote the profiles during forward and reverse scan respectively. The steady state profile is indicated with a dashed line. Note that the horizontal axis is broken to highlight the differences near the interfaces.

Comparing Figures 4.4a and 4.4d, we notice that much more charge is trapped near the ETL/perovskite interface in reverse bias. This is also illustrated in Figure 4.5: the lower concentration of holes (and higher concentration of electrons) causes a higher concentration of trapped charge in reverse bias.

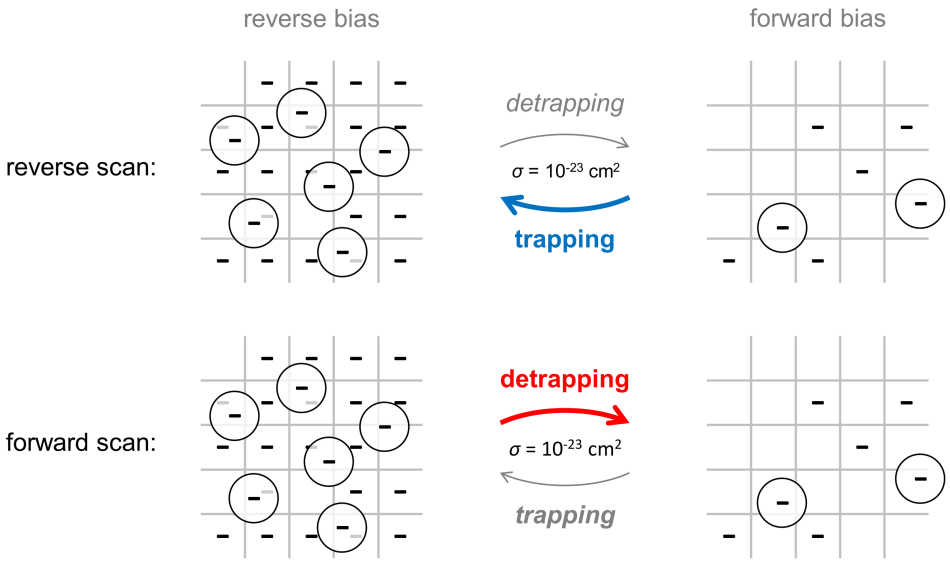

Figure 4.5: Illustration of the carrier trapping in reverse bias and forward bias. A lower concentration of holes (and higher concentration of electrons) cause a higher concentration of trapped charge in reverse bias. During the reverse scan carriers are predominantly trapped and during the forward scan carriers are predominantly detrapped. The low capture cross-section ($\sigma = 10^{-23}\,\mathrm{cm}^{-3}$) makes the process of trapping and detrapping relatively slow.

Looking at figures 4.4b and 4.4c, there is clearly more charge trapped during the forward scan (red curve) than during the reverse scan (blue curve). This is due to a slow capture and release of charge carrier by defects. This is also illustrated in Figure 4.5: the transition between both states (high amount of trapped charge and low amount of trapped charge) requires trapping and detrapping of carriers. These processes are relatively slow due to the low capture cross-section of $\sigma = 10^{-23}\,\mathrm{cm}^2$. A low capture cross-section is really essential for hysteresis to appear, as we will see in chapter 5.

4.3.1. Carrier trapping during the scan

As indicated above, the process of trapping dominates the process of detrapping during the reverse scan. This is due to two effects:

1. The rate of hole capture from the valence band (detrapping electrons) decreases, because the hole density p decreases:

   $$c_{\mathrm{V}}^{p} = \sigma_p v_{\mathrm{th}}^{p} p \qquad \text{(2.17 revisited)}$$

   At the same time the rate of electron capture from the conduction band increases, because the electron density n increases:

   $$c_{\mathrm{C}}^{n} = \sigma_n v_{\mathrm{th}}^{n} n \qquad \text{(2.16 revisited)}$$

2. The valence band quasi-Fermi level increases during the reverse scan (see the band diagrams in Figure 4.3). Capture of electrons becomes more dominant compared to the emission of electrons. This holds for both interaction with the valence band,

   $$\frac{e_{\mathrm{V}}^{n}}{c_{\mathrm{V}}^{n}} = \exp\left(\frac{E_{\mathrm{trap}} - E_{\mathrm{F},p}}{kT}\right) \qquad \text{(2.19 revisited)}$$

   and with the conduction band,

   $$\frac{e_{\mathrm{V}}^{n}}{c_{\mathrm{V}}^{n}} = \exp\left(\frac{E_{\mathrm{trap}} - E_{\mathrm{F},p}}{kT}\right) \qquad \text{(2.19 revisited)}$$

An analogous reasoning explains why detrapping dominates the process of trapping during the forward scan.

Taking a closer look at Figure 4.4a, it can be noticed that by the end of the reverse scan the concentration of trapped charge is still lower than what it would be in steady state. Prior to the forward scan the device is still not in equilibrium and the concentration of trapped charge continues to increase (see

also Figure 4.4b). This increase does not stop until at some point the concentration is higher than the steady state concentration again, after which the traps start emptying. For this simulation that happens when $V \approx 0.65\,\mathrm{V}$.

4.4. Increased recombination

Figure 4.6 shows the trapped electrons (4.6a), electrostatic potential 4.6b, carrier densities (4.6c) and recombination (4.6d) in the perovskite layer for both the reverse and forward scan. These profiles explain how carrier extraction is hindered during the forward scan. Here, we choose to plot at an applied bias of 0.8 V to highlight the differences between the scans as the output currents differ significantly in this part of the J-V curve. In Appendix C more plots for different applied biases can be found.

The higher concentration of trapped charge near the interface (Figure 4.6a) results in the electrostatic potential profile shown in Figure 4.6b (solid line). From the slope of this curve, we conclude that the electric field inside the absorber layer bulk points in the direction of the ETL during the forward scan. This is in contrast to the electric field during the reverse scan, which points towards the HTL instead. Thus, during the forward scan, the electric field does not effectively assist carrier extraction.

Figure 4.6c shows that this leads to much higher carrier densities during the forward scan. Especially the hole density close to the ETL is significantly higher. In Figure 4.6d it can be seen that this results in more recombination. Therefore the forward scan displays a reduced output current compared to the reverse scan.

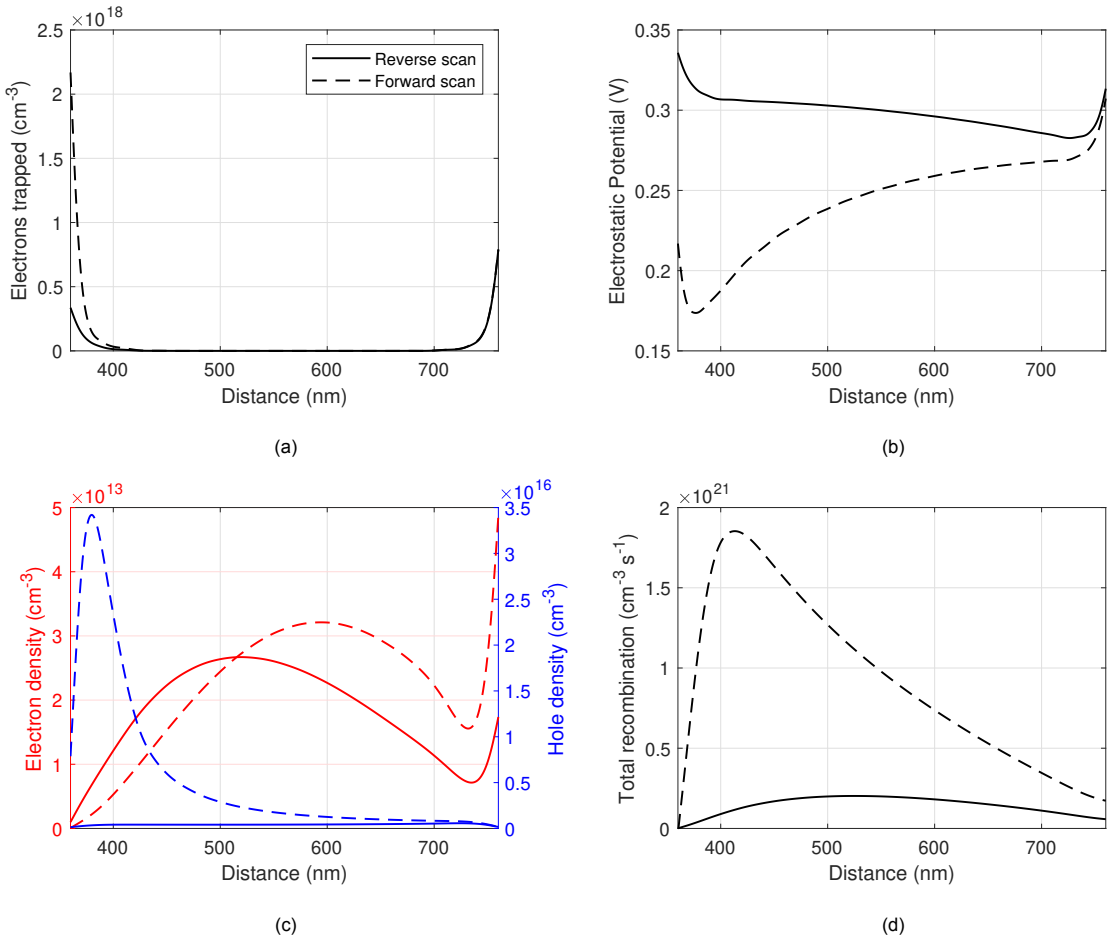

Figure 4.6: Profiles of (a) trapped electrons, (b) electrostatic potential, (c) electron/hole densities and (d) total recombination inside the perovskite absorber layer at an applied bias of 0.8 V. The ETL/perovskite interface is at the left side and the HTL/perovskite interface is at the right side. Each plot shows the profiles during the reverse scan (solid) and the forward scan (dashed).

5

Exploring the energy domain

To analyse the role of defect energy, we set up simulations where defects with a specific defect energy are embedded in the perovskite layer. The defects are uniformly distributed over the entire absorber layer. To highlight the effect of hysteresis we choose a relatively high defect density of $10^{17}\,\mathrm{cm}^{-3}$ and a typical scan rate of $0.1\,\mathrm{V\,s}^{-1}$. To study the effect of defect density and capture cross-section, we follow a similar approach but using different capture cross-sections (between 10^{-28} and $10^{-20}\,\mathrm{cm}^2$) and defect densities (between 10^{15} and $10^{18}\,\mathrm{cm}^{-2}$). In Figure 5.1 the Hysteresis Index of each simulated cell is plotted as a function of their activation energy for $N_\mathrm{t} = 10^{17}\,\mathrm{cm}^{-3}$.

In he figure we highlighted two regions. During a simulation $E_{\mathrm{F},p}$ always lies in the region shaded with light blue and $E_{\mathrm{F},n}$ always lies in the region shaded with dark blue. Figure 5.2 shows the variation of the quasi-Fermi levels for a device without defect states. We observe that the quasi-Fermi levels move closer to the band edges if the applied bias is increased, especially near the interfaces. This is because increasing the applied bias reduces the electric field in the absorber layer; the extraction of carriers by drift becomes less effective and the carrier densities increase.[1]

Looking at Figure 5.1, we observe that shallow acceptor-like defects close to the conduction band and shallow donor-like defects close to the valence band generate hardly any hysteresis. It stands out that hysteresis is more apparent if the defect energy is close to $E_{\mathrm{F},p}$ (for acceptor-like defects) or close to $E_{\mathrm{F},n}$ (for donor-like defects). We also observe that HI attains its highest values for capture cross-sections around $10^{-24}\,\mathrm{cm}^2$ and that HI becomes very small for much lower or higher capture cross-sections.

[1] The presence of defect states also influences the quasi-Fermi levels through charge trapping (see also section 5.2.1) and trap-assisted recombination. With or without defects, the trend remains that the quasi-Fermi levels move closer to the band edges if the applied bias is increased.

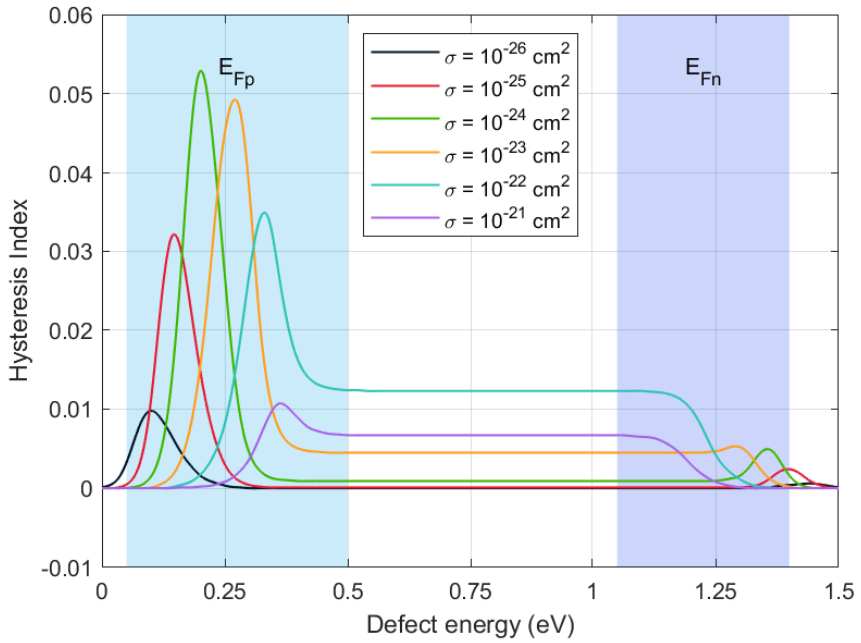

(a) Simulation results with acceptor-like defects.

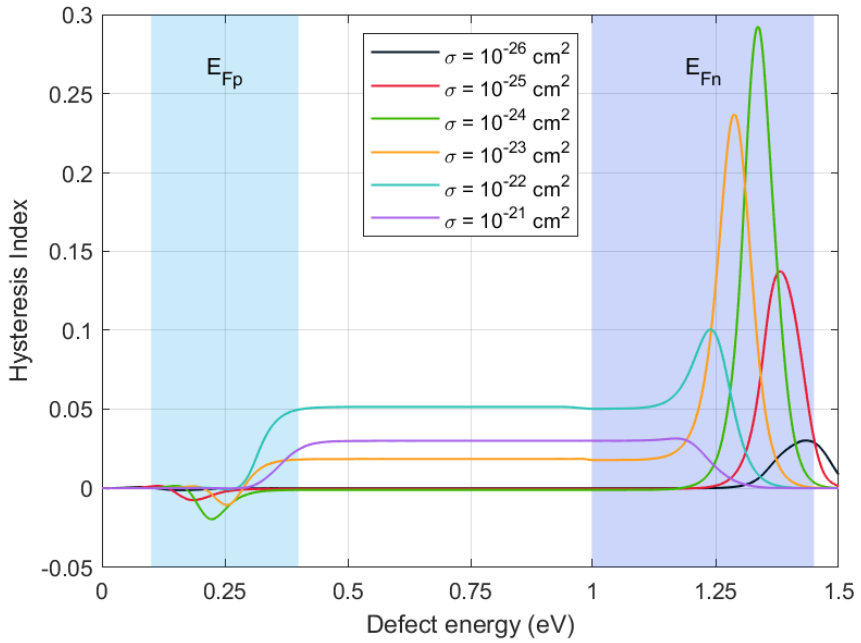

(b) Simulation results with donor-like defects.

Figure 5.1: Simulation results with varied defect energy and capture cross-sections. The defects are uniformly distributed with a defect density of 10^{17} cm^{-3} for all simulations. The scan rate is 0.1 V s^{-1}. Blue areas indicate the energy range in which the valence band quasi-Fermi level ($E_{\mathrm{F},p}$) and conduction band quasi-Fermi level ($E_{\mathrm{F},n}$) are during a scan.

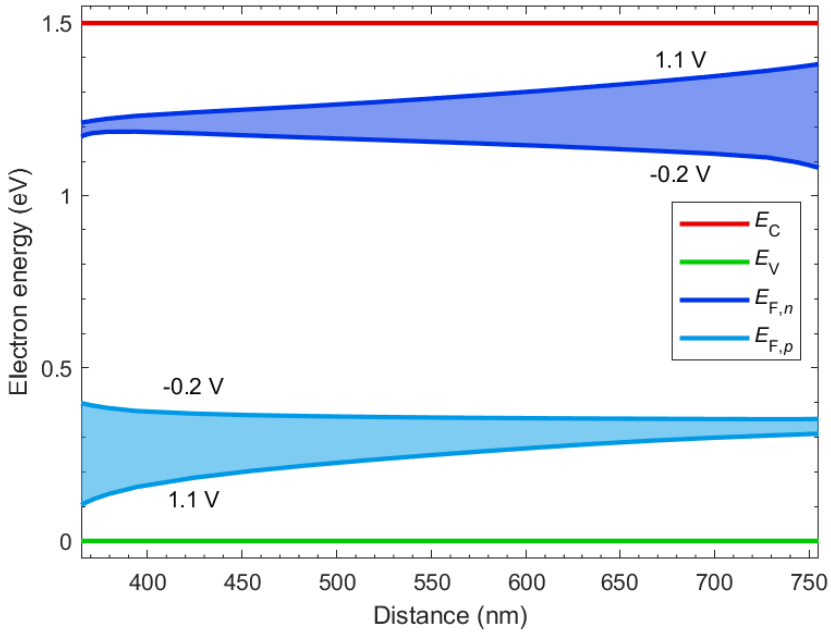

Figure 5.2: Cross section of the perovskite layer showing the quasi-Fermi levels as a function of position in the device, at −0.2 V applied bias and 1.1 V applied bias. Labels indicate which line corresponds to which applied bias (−0.2 V or 1.1 V). The regions in between those lines are shaded because the quasi-Fermi levels lie in these regions when a bias between −0.2 V and 1.1 V is applied. The left side of the figure is the ETL/perovskite interface and the right side is the perovskite/HTL interface.

5.1. Carrier emission and capture

In order to explain the above-mentioned observations, we have to take a closer look at the trap occupation dynamics. Here, we present an explanation of our observations, based on analytical expressions from the theory in section 2.2.

The dynamics describing trap occupation, emission and capture, involves interaction with both the valence and conduction band. Considering all four processes, i.e. capture and emission from both the conduction and the valence band, the trap occupation changes as follows:

$$\frac{\partial f_t}{\partial t} = \underbrace{\sigma_n v_{th}^n n\left((1-f_t) - f_t \exp\left(\frac{E_{trap}-E_{F,n}}{kT}\right)\right)}_{\text{interaction conduction band}} + \underbrace{\sigma_p v_{th}^p p\left((1-f_t)\exp\left(\frac{E_{F,p}-E_{trap}}{kT}\right) - f_t\right)}_{\text{interaction valence band}} \tag{5.1}$$

The trap occupation rate of change is important because it describes how fast charge accumulates and how long it takes to release the charge again. In the end, the typical timescales for trapping and detrapping determine at which scan rate hysteresis occurs.

In steady state, the time derivative vanishes and the trap occupation becomes

$$f_{t,0} = \frac{\sigma_n v_{th}^n n + \sigma_p v_{th}^p p \exp\left(\frac{E_{F,p}-E_{trap}}{kT}\right)}{\sigma_n v_{th}^n n\left(1+\exp\left(\frac{E_{trap}-E_{F,n}}{kT}\right)\right) + \sigma_p v_{th}^p p\left(1+\exp\left(\frac{E_{F,p}-E_{trap}}{kT}\right)\right)} \tag{5.2}$$

The steady state occupation is relevant because hysteresis can only occur if the number of trapped carriers changes significantly during a scan. In Figure 5.3 we illustrate this for acceptor-like defects. If the amount of trapped charge in steady state is significantly higher in reverse bias than in forward bias (5.3a), there is also a large difference in the amount of trapped charge during both scans due to slow trapping and detrapping. On the other hand, if the amount of trapped charge changes only slightly in steady state, the difference in trapped charge during both scans is also small.

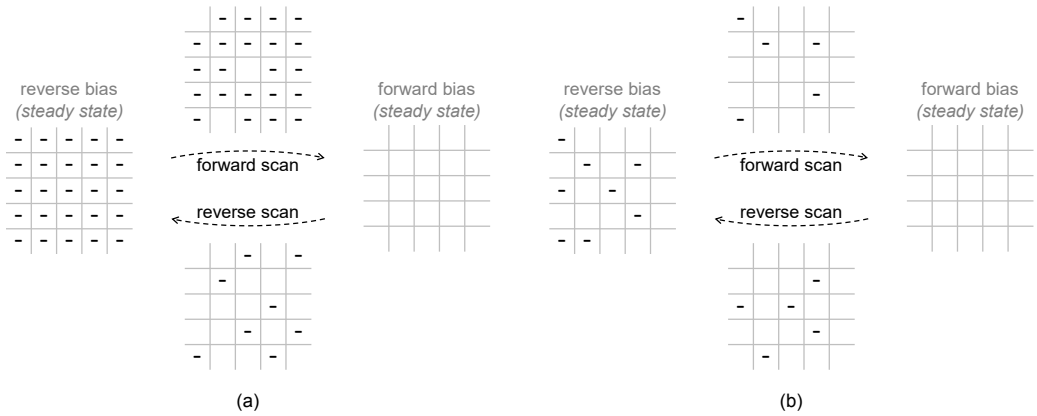

Figure 5.3: Illustration showing the difference between the forward scan and reverse scan. (a) Situation in which there is much more charge trapped in reverse bias than in forward bias. (b) Situation in which there is only slightly more charge trapped in reverse bias than in forward bias.

Hysteresis thus requires a significant change in trap occupation during a scan. But how does this explain the observation that hysteresis is more apparent if the defect energy is close to the quasi-Fermi level (see Figure 5.1)? Let us first elaborate this for acceptor-like defects close to $E_{\mathrm{F},p}$ (i.e. Figure 5.1a).

Figure 5.4 shows the Fermi-Dirac distributions corresponding to the valence band quasi-Fermi level in forward bias (1.1 V) and reverse bias (−0.2 V). Remember that the Fermi-Dirac distribution $f(E)$ gives the (average) occupation of electronic states at an energy E. If we assume there is only electron capture and emission to and from the valence band, thus exchange of electrons between defect states and the electronic states in the conduction band is negligible, equation (5.2) simplifies to the regular Fermi-Dirac distribution (equation (2.1) with $E_{\mathrm{F}} = E_{\mathrm{F},p}$). So under this assumption, Figure 5.4 gives the averge trap occupation f_{t} in forward bias (1.1 V) and reverse bias (−0.2 V).

Only for a small range of energies the occupation f_{t} changes drastically, which is indicated with a blue shade. This explains why we observe extreme hysteresis for acceptor-like defects close to $E_{\mathrm{F},p}$. Extreme hysteresis for donor-like defects close to $E_{\mathrm{F},n}$ arises in an analogous way, but is due to interaction with the conduction band instead of the valence band.

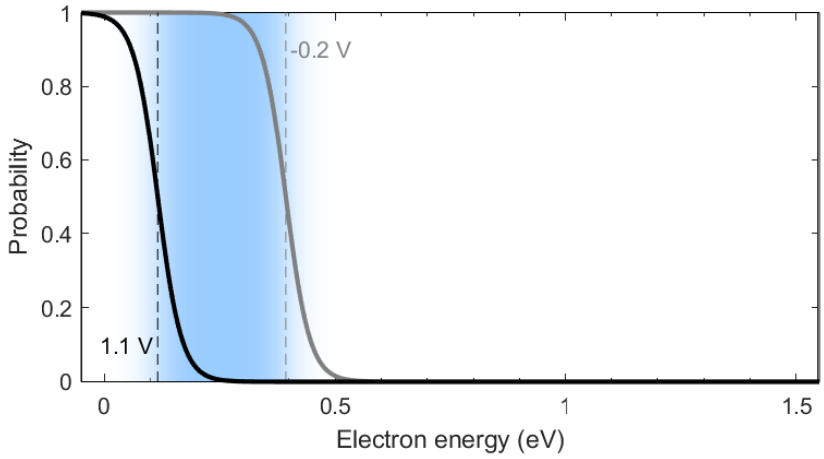

Figure 5.4: Fermi-Dirac distributions corresponding to the valence band in the perovskite layer close to the ETL/perovskite interface in stationary state. The curves are plotted for −0.2 V applied bias (gray) and 1.1 V applied bias (black). The dashed lines indicate the valence band quasi-Fermi level $E_{\mathrm{F},p}$. The blue shaded area shows for which energies the value of the Fermi-Dirac distribution changed significantly.

So far we neglected interaction with the conduction band. As long as the variation of $E_{\mathrm{F},p}$ is large enough and $E_{\mathrm{F},n}$ is not too high, the analysis still holds and the occupation of electronic states in the blue shaded area will indeed change significantly. However, this simplified analysis does not explain why we also observe hysteresis for defect states deeper in the bandgap (see Figure 5.1).

To explain this, consider Figure 5.5. It shows the electron distribution function for the valence band and conduction band. Three regions are indicated: (1) energies below the valence band quasi-Fermi level, (2) energies between both quasi-Fermi levels and (3) energies above the conduction band quasi-Fermi level. The electron distribution function determines the occupation of an electronic state. Electronic states in region 1, sufficiently far away from the valence band quasi-Fermi level, are almost fully occupied by electrons. Similarly electronic states in region 3, sufficiently far away from conduction band the quasi-Fermi level, are almost entirely empty.

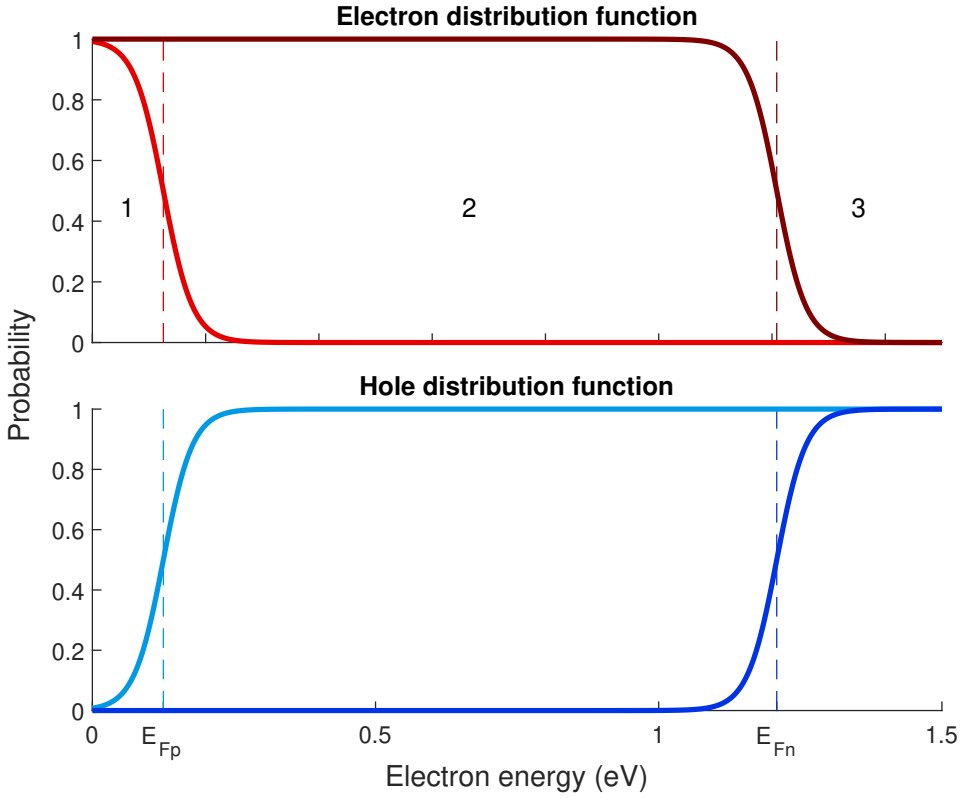

Figure 5.5: Top: Fermi-Dirac distribution function corresponding to the valence band (light red) and conduction band (dark red). Bottom: Distribution functions for holes, i.e. the complementary probability distributions of the Fermi-Dirac distributions in the top graph. The light blue curve corresponds to the valence band and the dark blue curve to the conduction band. Dashed lines indicate the quasi-Fermi levels.

5.1.1. Defects in region 1 and 3

Defects in region 1 and 3 (see Figure 5.5) cause hardly any hysteresis. If the defect energy stays below the valence band quasi-Fermi level the entire time (region 1) or above the conduction band quasi-Fermi level (region 3), the average occupation remains roughly the same during the scan. As a result, there is hardly any difference between the forward and reverse scan.

5.1.2. Defects in region 2

For electronic states in region 2 (see Figure 5.5), there will be net emission of electrons to the valence band, but net capture of electrons from the conduction band. This can also be inferred from equation (5.1). Let us consider a defect in region 2, such that the quasi-Fermi levels and the defect are sufficiently far energetically apart. Then we have $E_{\mathrm{F},p} \ll E_{\mathrm{trap}} \ll E_{\mathrm{F},n}$. Equation (5.2) then reduces to [2]

$$f_{\mathrm{t},0} = \frac{\sigma_n v_{\mathrm{th}}^n n}{\sigma_n v_{\mathrm{th}}^n n + \sigma_p v_{\mathrm{th}}^p p} \tag{5.3}$$

When f_{t} is not too close to 0 or 1, equation (5.1) can be approximated with

$$\frac{\partial f_{\mathrm{t}}}{\partial t} = \sigma_n v_{\mathrm{th}}^n n(1 - f_{\mathrm{t}}) - \sigma_p v_{\mathrm{th}}^p p f_{\mathrm{t}} \tag{5.4}$$

From equation (5.3), it follows that the steady state occupation of defects in region 2 is approximately independent of the defect energy. It follows from equation 5.4 that its rate of change is also roughly independent of the defect energy. We thus expect similar behaviour from all defects in region 2. This explains why we observe the same Hysteresis Index in Figure 5.1 for defect energies in region 2.

5.2. Evaluating trap effectiveness

As explained in the previous sections, a defect with defect energy E_{trap} at a particular location could potentially cause hysteresis if its occupation changes drastically when the applied bias is switched from forward bias to reverse bias or vice versa. To evaluate this, we introduce the quantity Δf_{t}, which is defined as

$$\Delta f_{\mathrm{t}} = \left| f_{\mathrm{t,\ forward\ bias}} - f_{\mathrm{t,\ reverse\ bias}} \right| \tag{5.5}$$

where $f_{\mathrm{t,\ forward\ bias}}$ and $f_{\mathrm{t,\ forward\ bias}}$ are the stationary-state electron occupations of electronic states in forward bias and reverse bias respectively.

If Δf_{t} is close to 1 for a certain defect energy E_{t} and position in the device, we expect that the presence of defects at this energy and position will cause hysteresis in the J-V curve. If Δf_{t} is close to 0, defects at this energy and position will *not* cause hysteresis, because their occupation remains approximately the same during a scan and, consequently, there is no delayed capture/release of charge. This quantity thus gives a good indication of which defects potentially cause hysteresis.

Figure 5.6 shows a plot of Δf_{t} as a function of position and defect energy for a device without defects (only band tails are incorporated in the simulation). The valence band quasi-Fermi level $E_{\mathrm{F},p}$ in reverse bias (−0.2 V) and reverse bias (1.1 V) is indicated in dark blue. The conduction-band quasi-Fermi level $E_{\mathrm{F},n}$ is indicated in light blue. We want to highlight three aspects:

- Δf_{t} is much higher near the interfaces. In the middle of the layer Δf_{t} is lower than 0.6 (regardless the energy), whereas values very close to 1 are attained at the interfaces. This shows that the hysteretic behaviour can be ascribed to defects near the interfaces.
- We observe that Δf_{t} is high for energies between $E_{\mathrm{F},p}$ in reverse bias and $E_{\mathrm{F},p}$ in forward bias. The quantity is also high for energies between $E_{\mathrm{F},n}$ in reverse bias and $E_{\mathrm{F},n}$ in forward bias. Below $E_{\mathrm{F},p}$ and above $E_{\mathrm{F},n}$, the quantity is almost zero. This means that occupation of defects with energy near $E_{\mathrm{F},p}$ or changes drastically during a J-V scan. It explains (again) why we observe high values of the HI for these energies in Figure 5.1.
- In between $E_{\mathrm{F},p}$ and $E_{\mathrm{F},n}$ the values of Δf_{t} are also high near the interfaces. Based on this, one would expect that defects with energy between the two quasi-Fermi levels also cause severe hysteresis. Nonetheless, Figure 5.1 shows that the HI for these defects is considerably lower than for defects in the blue shaded areas (see also 5.1). In section 5.2.1 we explain that this is predominantly due to a ‘negative feedback mechanism’ that limits the amount of trapped charge.

[2] The defect energy E_{trap} must be sufficiently far apart from $E_{\mathrm{F},p}$ and $E_{\mathrm{F},n}$ such that $\sigma_n v_{\mathrm{th}}^n n \gg \sigma_p v_{\mathrm{th}}^p p \exp\left((E_{\mathrm{F},p} - E_{\mathrm{trap}})/(kT)\right)$ and $\exp\left((E_{\mathrm{trap}} - E_{\mathrm{F},n})/(kT)\right) \ll 1$. This is a reasonable assumption when $E_{\mathrm{trap}} - E_{\mathrm{F},p}$ and $E_{\mathrm{F},n} - E_{\mathrm{trap}}$ are a few tenths of an eV

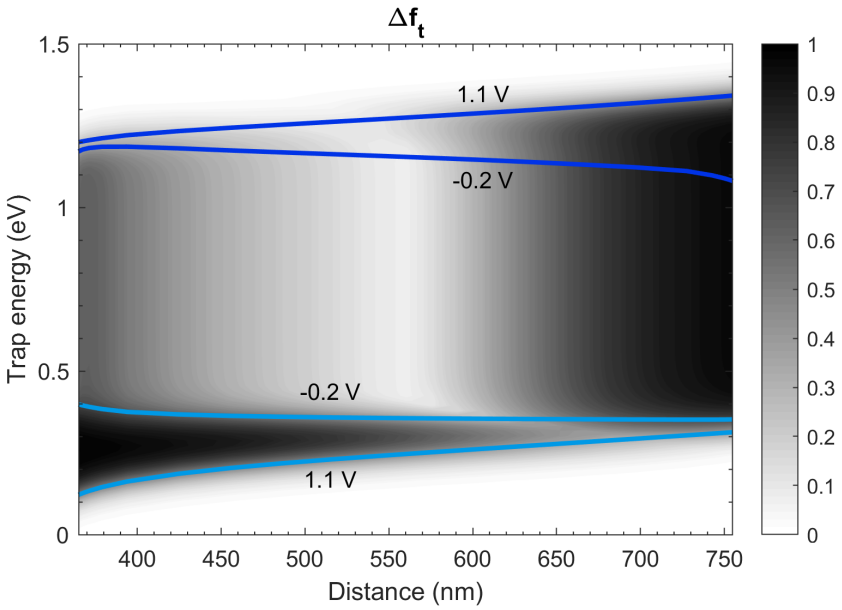

Figure 5.6: Plot of Δf_t as a function of defect energy and position. The quasi-Fermi levels in forward bias (1.1 V) and reverse bias (−0.2 volt) are indicated with light blue ($E_{F,p}$) and dark blue ($E_{F,n}$).

All in all, we conclude from Figure 5.1 and Figure 5.6 that acceptor-like defects near the ETL/perovskite interface with a transition energy near $E_{F,p}$ and donor-like defects near the HTL/perovskite interface with a transition energy near $E_{F,n}$ can cause severe hysteresis. This is because their average occupation changes drastically during a J-V scan.

5.2.1. Negative feedback in charge trapping

As mentioned above, deep defects with a transition energy between $E_{F,p}$ and $E_{F,n}$ cause less severe hysteresis than we expect based on Figure 5.6. A closer analysis of our simulations with donor-like defects showed that only a fraction of these deeper defect states gets occupied in reverse bias. In Figure 5.7 we have illustrated why this occurs. When positive charge is trapped close to the HTL (a), this attracts electrons and repels holes (b). Because of the increased electron density and reduced hole density, trapping of carriers stops (c). This negative feedback limits the amount of trapped charge and consequently the observed hysteresis. Here, we illustrated the feedback mechanism using donor-like defects near the HTL, but a similar reasoning can be applied to acceptor-like defects near the ETL.

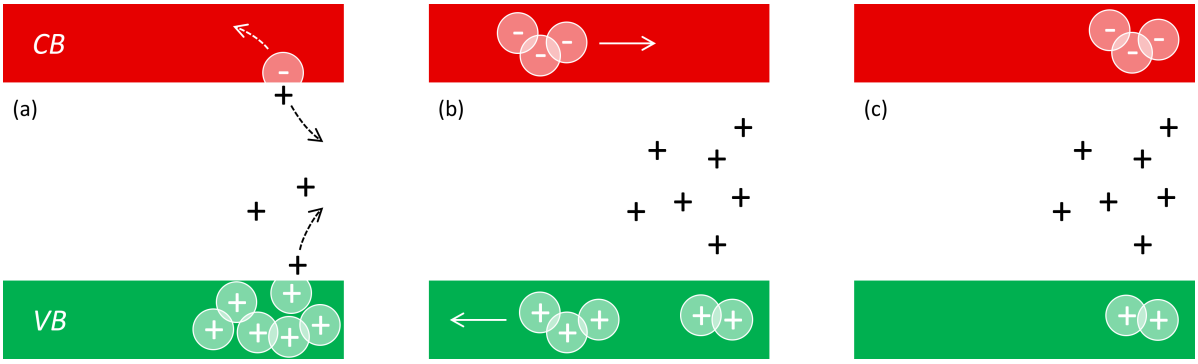

Figure 5.7: Illustration of the negative feedback mechanism that limits charge trapping. (a) An excess of holes and low electron density cause charge trapping by defect states. (b) Trapped charge attracts electrons and repels holes. (c) Because of the increased electron density and reduced hole density, trapping of carriers stops.

5.3. Effect of defect density

Figure 5.8 shows simulation results with varied defect densities. The profiles remain their characteristics upon variation of the defect density. As expected, hysteresis significantly reduces for low defect densities and is almost negligible (< 0.02) for $N_T = 10^{16}\,\mathrm{cm}^{-3}$ and lower. Intensified charge accumulation is the main reason for a higher HI at higher defect densities; efficient carrier extraction is more strongly suppressed during the forward scan at higher defect densities. Besides, SRH recombination increases at higher defect densities. Together the higher accumulation and increased recombination result in a larger difference between the scans and thus stronger hysteresis in the J-V curve.

So far, we have explored the energy domain with uniform defect distributions in the space domain. However, measured bulk defect densities vary from $10^{10}\,\mathrm{cm}^{-3}$ for single crystals to $10^{16}\,\mathrm{cm}^{-3}$ in perovskite thin films [61, 64, 66, 70, 115]. Uniformly distributed defects with densities lower than $10^{16}\,\mathrm{cm}^{-3}$ yield very low values of HI, so bulk defects alone cannot reproduce anomalous hysteresis.

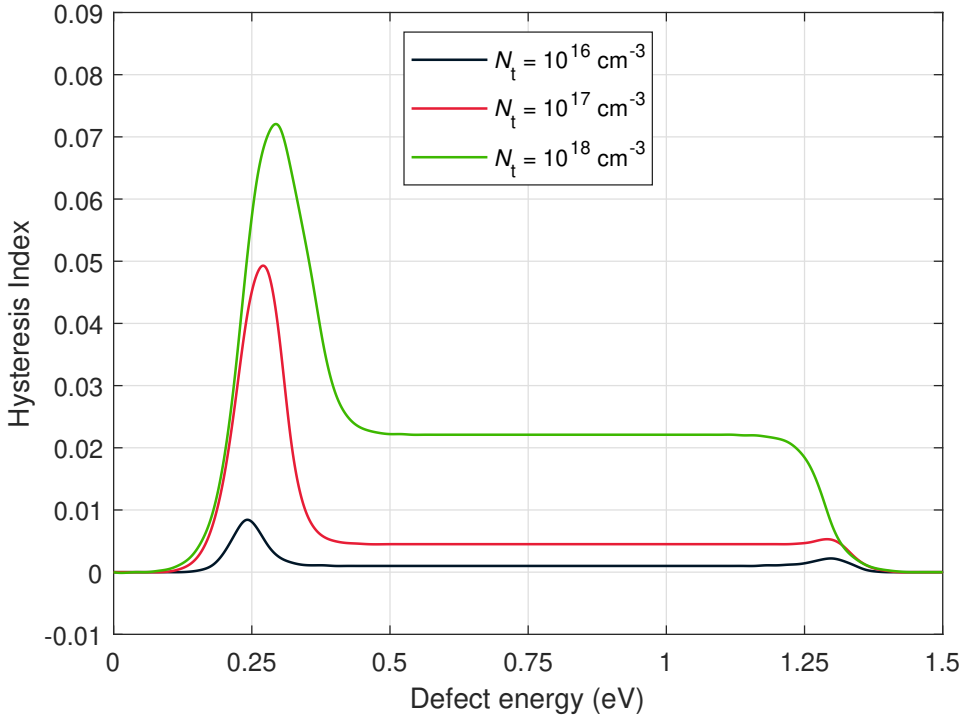

Figure 5.8: Results of simulations with varied defect energy and energy density. The defects are uniformly distributed and the capture cross-section is $10^{-23}\,\mathrm{cm}^2$.

5.4. Band tail states as the origin of hysteresis?

Our next approach to reproduce hysteresis is to vary both the valence and conduction band capture cross-section of the band tail states. We evaluated the Hysteresis Index at a constant scan rate of $0.1\,\mathrm{V\,s}^{-1}$, while the capture cross-sections were varied over a range of values between $10^{-30}\,\mathrm{cm}^2$ and $10^{-10}\,\mathrm{cm}^2$.

We observed some configurations that show light hysteresis and found a strong correlation between the capture cross-section and the scan rate at which hysteresis was observed. For higher capture cross-sections hysteresis is most severe at higher scan rates. Although the scan rate at which the maximum HI occurs depends on the capture cross-section, the maximum value itself seems not to be affected by the capture cross-section. In chapter 6 we provide more insights about such an effect.

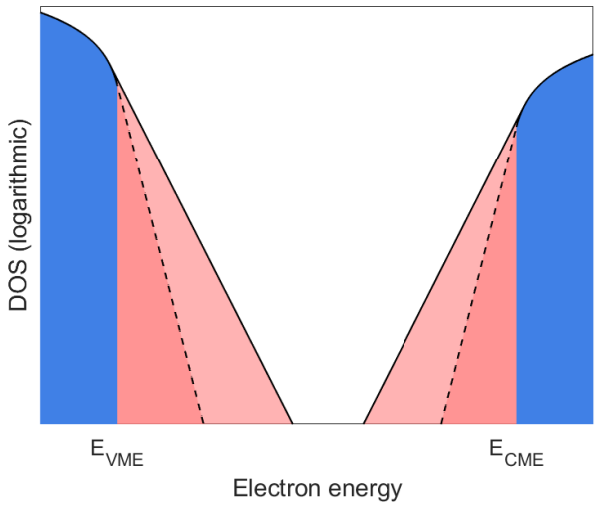

Figure 5.9: Illustration of varying the characteristic energy of band tail states. The valence and conduction band are shown in blue and the tail states are red.

Because none of our first results showed really extreme hysteresis, we decided to also vary the characteristic energy of the band tails as shown in Figure 5.9. The black line in Figure 5.10 shows the Hysteresis Index against the characteristic energy ($W_C = W_V$). The simulated cell displays inverted hysteresis that becomes more severe as the band tail states have higher characteristic energies. The current-voltage hysteresis is a result of charge accumulation at the interface, about which we provide more insights in chapter 4.

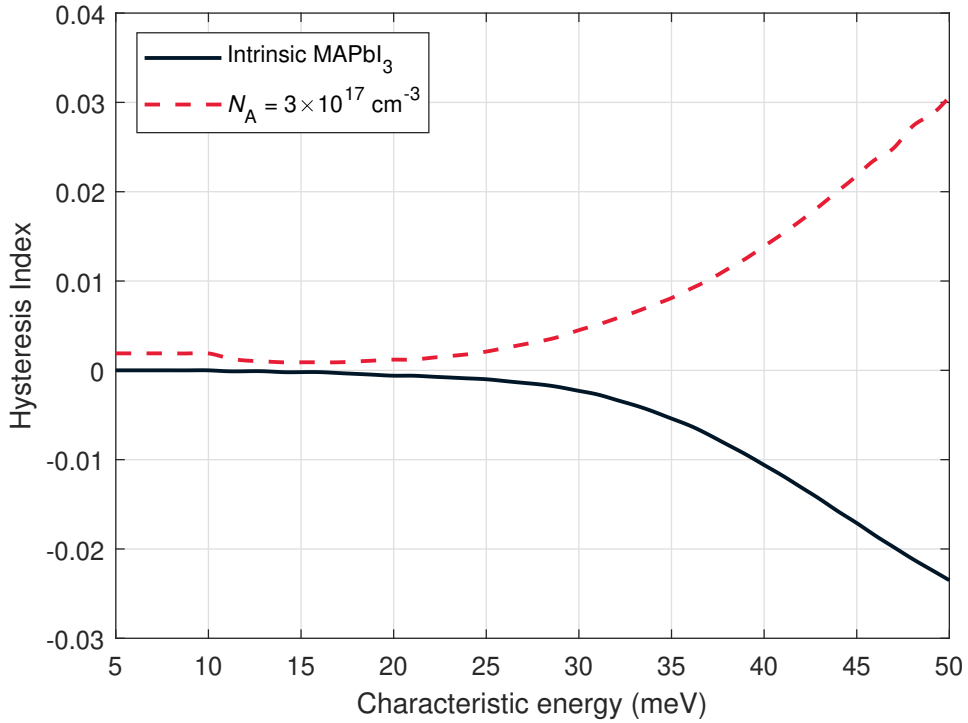

Figure 5.10: Hysteresis Index as a function of characteristic energy ($W_C = W_V$) for a scan rate of 0.1 V s^{-1}. The capture cross-sections are fixed at $\sigma_n = \sigma_p = 10^{-24}$ cm^2.

Whether the accumulated charge improves or degrades the device performance, depends on the band structure of the device (see section 4.1). The position of the Fermi level is therefore an important parameter. Because unintentional doping can change the Fermi level in perovskite material, as men-

tioned in section 2.4, we varied the position of E_F. We simulated p-type perovskite by adding acceptor dopants to the layer and n-type perovskite by adding donor dopants. The doping concentrations were chosen such that for the bulk, in thermal equilibrium:

- $E_F - E_V$ equals 0.1, 0.2 or 0.3 eV (p-type)

or

- $E_C - E_F$ equals 0.1, 0.2 or 0.3 eV (n-type)

The corresponding doping densities are summarised in Table 5.1. For the lighter doped perovskites (i.e. $E_F - E_V = 0.3$ eV, $E_C - E_F = 0.2$ eV and $E_C - E_F = 0.3$ eV) almost no difference with the intrinsic perovskite was observed and therefore they are omitted in subsequent plots.

Table 5.1: Fermi level positions and corresponding doping densities used in for simulations.

Type	$E_F - E_V$ (eV)	$E_C - E_F$ (eV)	N_A (cm^{-3})	N_D (cm^{-3})
p-type	0.1		3×10^{17}	
p-type	0.2		6.5×10^{15}	
p-type	0.3		1.5×10^{14}	
n-type		0.1		3.0×10^{16}
n-type		0.2		6.5×10^{14}
n-type		0.3		1.5×10^{13}

This time the simulated cells show not only inverted, but also normal hysteresis. For intrinsic and n-type perovskite the hysteretic behaviour was generally more inverted-like, while only highly doped p-type perovskite showed normal hysteresis. Figure 5.11 shows the HI as a function of scan rate for different doping concentrations. For lower scan rates, the magnitude of HI increases with increasing scan rate and reduces again when the scan rate is further increased. This is in good agreement with the experimental observations described in section 2.6.1. The increase in HI at very high scan rates ($> 100\,\mathrm{V\,s^{-1}}$) is related to electronic displacement currents.

In Figure 5.10 we observe that severe hysteresis requires wider band tails in terms of larger characteristic energy. But Figure 5.11 shows that even cells with very wide band tails ($W_C = W_V = 50$ meV) display relatively low HI values. The magnitude of HI is below 0.04 at all scan rates, whereas cells with severe hysteresis can have HI values above 0.15 [29]. The low HI values are observed regardless of whether the perovskite is intrinsic, p-type or n-type. We thus conclude that slow trapping and detrapping of carriers by band tail states cannot explain anomalous hysteresis in PSCs.

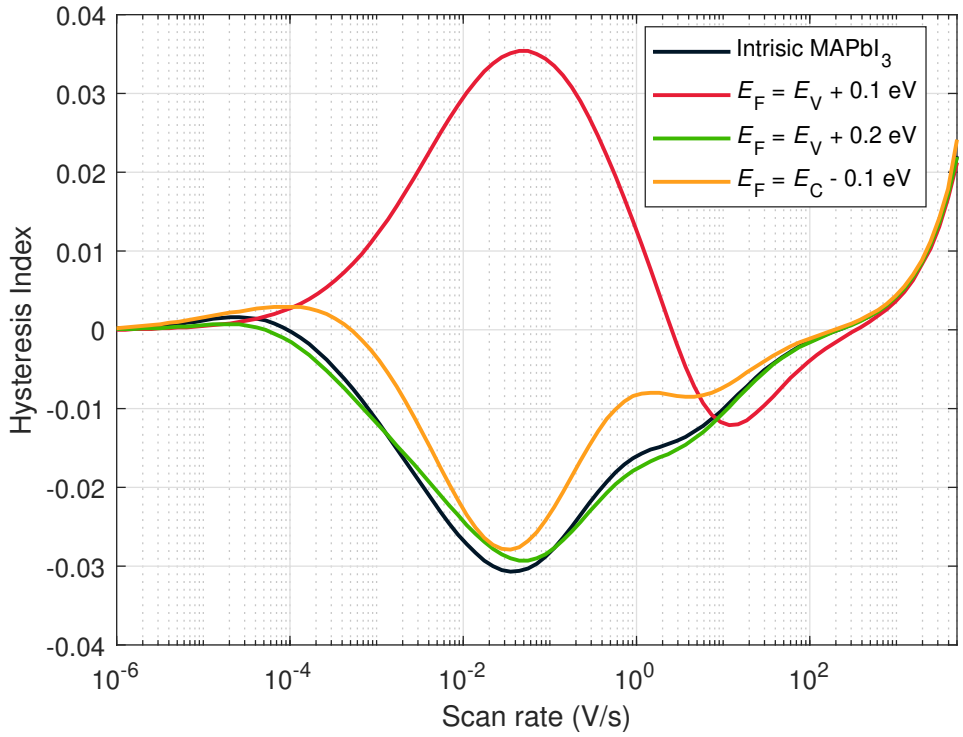

Figure 5.11: Hysteresis Index as a function of scan rate for different doping concentrations. The legend entries give the perovskite bulk Fermi level for a device in thermal equilibrium. The tail states in these simulations have an excessively high characteristic energy $W_C = W_V = 50\,\text{meV}$. The capture cross-sections are fixed at $\sigma_n = \sigma_p = 10^{-25}\,\text{cm}^2$.

6

Realistic model based on interface defects

In this chapter we will elaborate on the response of our model, as described in section 3.4.2 (chapter 3), upon variation of defect distributions, capture cross-sections and scan rate. We discuss the simulated J-V curves and their dependence on scan rate in more detail. Section 6.3 describes the importance of capture cross-sections and we show in section 6.4 that hysteresis can be reduced significantly by reducing the defect density. Section 6.5 provides an analysis of the defect energy, including a discussion about the origin of the defect states that are attributed to hysteresis. Impedance spectra and their connection to hysteresis are discussed in section 6.6.

6.1. The importance of interfaces

Figure 6.1 shows J-V scans for different device architectures and defect distributions. Table 6.1 summarises the parameters used for each simulation. The device in Figure 6.1a has only donor-like defects near the ETL with an average energy $E_{t,0} = 0.25\,\text{eV}$. The device in Figure 6.1b has only acceptor-like defects near the HTL with an average energy $E_{t,0} = 1.3\,\text{eV}$.

Hysteresis is more apparent in Figure 6.1b than in Figure 6.1a, showing a stronger 'S-shaped' kink. In Figure 6.1c the J-V scan of a device with both acceptor-like defects near the ETL and donor-like defects near the HTL. This shows that hysteresis is even stronger if both defects are present in the same device. In a way, the detrimental effect of charge polarisation on both sides of the perovskite layer adds up.

So far, we have seen that our model can reproduce hysteresis in n-i-p architectures. Our model, however, can be easily extended to other device architectures. Figure 6.1d shows the J-V scans for a PSC with p-i-n structure. We used a simple band-to-band tunneling model for the inter-band transfer between the TCO and HTL. The material and device parameters are shown in Table D.1 in Appendix D.

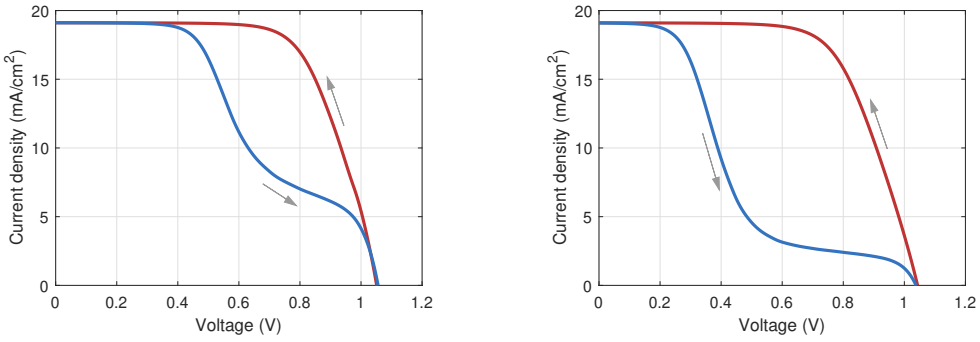

(a) Donor-like defects near ETL.

(b) Acceptor-like defects near HTL

(c) Donor- and acceptor-like defects.

(d) Inverted architecture (n-i-p).

Figure 6.1: J-V scans for different device architectures and defect distributions. The corresponding properties are summarised in Table 6.1. The scan rate is 0.1 V s^{-1} in all cases.

Table 6.1: Properties used for simulations of J-V curves in Figure 6.1. In all cases .

Figure	Architecture	Defect type	$E_{t,0}$ (eV)	$N_{t,ETL}$ (cm^{-3})	$N_{t,HTL}$ (cm^{-3})	σ (cm^2)
6.1a	n-i-p	Acceptor	0.25	10^{19}	0	10^{-24}
6.1b	n-i-p	Donor	1.3	0	1×10^{19}	10^{-24}
6.1c	n-i-p	Acceptor/Donor	0.25 / 1.3	10^{19} / 0	0 / 10^{19}	10^{-24}
6.1d	p-i-n	Acceptor	0.25	3×10^{18}	0	10^{-24}

6.2. Current-voltage curves

Figure 6.2 shows simulated J-V scans for a range of scan rates. The simulation parameters are given in Table 3.2 in chapter 3. Pronounced hysteresis is present at scan rates around 0.1-1 V s^{-1}. For lower scan rates hysteresis diminishes, as both the forward and reverse scan approach the steady state J-V curve. Also for higher scan rates we observe reduced hysteresis. This goes along with improved performance.

The fact that the steady-state J-V curve (dashed line in Figure 6.2) lies much lower than the J-V curves at high scan rates, reflects that the device degrades over a relatively short time (tens to hundreds of seconds) due to slow defects near the interface. Figure 6.2 also shows quite well how hysteresis complicates device characterisation. The long-term PCE (as determined by the steady-state response) cannot be accurately determined using scan rates slower than 0.01 V s^{-1}.

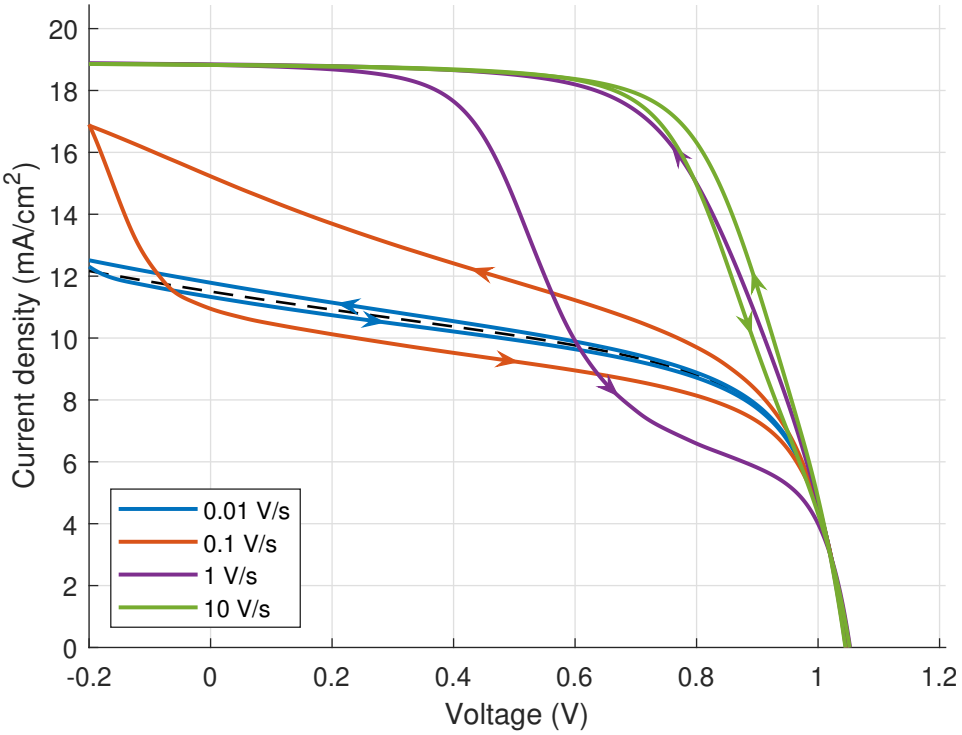

Figure 6.2: Simulation of J-V curves under illumination showing pronounced hysteresis. Arrows denote the scan direction and the scan rates are from 0.01 to 10 V s^{-1}. The dashed line represents the steady-state solution.

It stands out that the forward scan shows a clear 'S-shaped' curve. A bend is present in the forward curve, which is responsible for a poor fill factor. Such 'S-shaped' curves have previously been reported in literature for organic and inorganic solar cells, where their origin was attributed to an energetic barrier for charge extraction at the interface [118].

This particular shape does not quite match the hysteresis as observed in experiments with real devices. Remarkably, our results do not show hysteresis in the open circuit voltage. Such is for example the case in measurements of Snaith et al. [29], Chen et al. [119] and Wei et al. [120]. This was also noted by van Reenen et al. when they modeled hysteresis using ion migration [91]. They suggested that current and voltage hysteresis must be explained by an alternative mechanism.

On the other hand, the precise shape of J-V curves varies vastly across different experiments and also our simulations show a wide variation in shapes, depending on the defect distribution and scan rate. 'S-shapes' are present in some curves measured by Wu et al. and to some extent also in the measurements by Tress et al. [45, 110]. Tress et al. also observed a bump in the J-V curve during the reverse scan, which is not observed in our simulations.

6.3. Capture cross-sections

In Figure 6.3 the Hysteresis Index is shown as a function of scan rate for different capture cross-sections. This clearly shows the observed trend (Figure 6.2) that hysteresis is most pronounced at a particular scan rate and diminishes when the scan rate is either decreased or increased. Further, we observe that varying the capture cross-section shifts the occurrence of hysteresis towards higher or lower scan rates, but does not change the maximum value of HI itself.

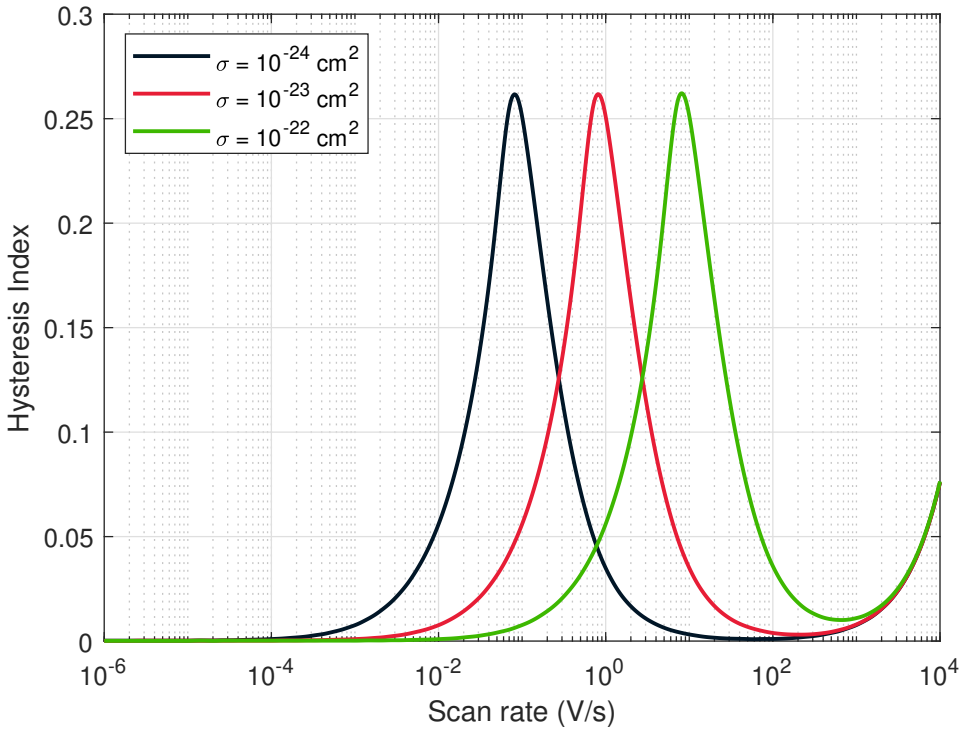

Figure 6.3: Hysteresis Index for device simulations with varied capture cross-section as a function of scan rate.

Furthermore, we investigated what happens if the capture cross-sections differ for electrons and holes. Varying σ_n while keeping σ_p constant (or vice versa) can entirely remove hysteresis in a simulation. This is because the 'limiting' factor is the fastest interaction, i.e. the fastest interaction predominantly determines how rapid defects are filled and emptied. As we have seen before, there is no hysteresis if the process of trapping and detrapping is much faster than the scan itself. For a similar reason, different capture cross-sections can also lead to more extreme hysteresis in simulations.

Capture cross-sections could be different across different devices, depending on the origin of the defect. Based on Figure 6.3, this could explain why hysteresis is observed at different scan rates for different architectures.

6.4. Defect density

To study the effect of defect passivation, we varied the defect density at the ETL/perovskite interface, while keeping the defect density in the bulk and at the HTL/perovskite constant. Figure 6.4 shows the Hysteresis Index as a function of scan rate for different defect densities $N_{t,ETL}$ near the ETL. As expected, hysteresis becomes more severe with increasing defect density and is clearly noticeable for defect densities above ~10^{18} cm^{-3}. Next to this, the range of scan rates for which hysteresis occurs shifts upwards as the density increases.

The trends in figure Figure 6.4 show that hysteresis can be eliminated by reducing the defect density near the interface. We discuss this in more detail in chapter 7.

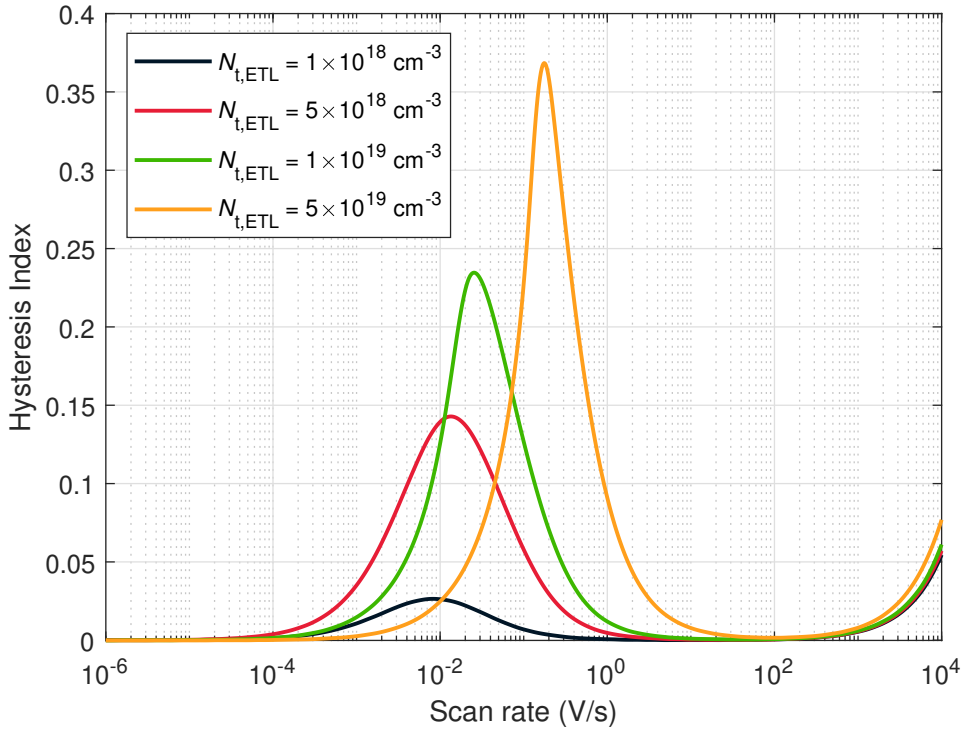

Figure 6.4: Hysteresis Index for device simulations with varied defect density at the ETL/perovskite interface.

6.5. Defect energy

Figure 6.5 shows HI as a function of the average defect energy $E_{t,0}$, all other parameters being equal to those given in Table 3.2. We observe that hysteresis is most apparent for $E_{t,0} = 0.27$ eV and diminishes for lower and higher average defect energies. This confirms the earlier analysis in chapter 5 indicating that, considering acceptor-like defects, only defects with energy close to $E_{F,p}$ cause anomalous hysteresis.

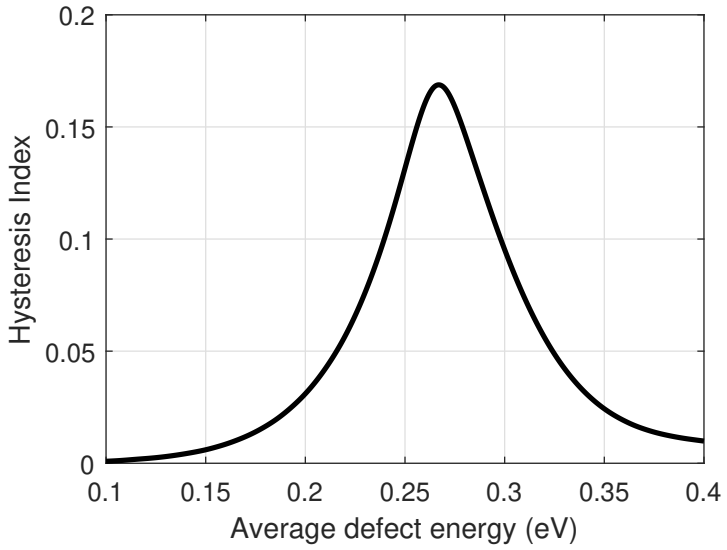

Figure 6.5: Hysteresis Index as a function of average defect energy $E_{t,0}$ for a device with acceptor-like defects near the ETL.

Table 6.2: Defect model parameters used in figures 6.5 and 6.6.

Figure	Defect type	$E_{t,0}$ (eV)	$N_{t,ETL}$ (cm^{-3})	$N_{t,HTL}$ (cm^{-3})
6.5	Acceptor	0.25	10^{19}	1×10^{18}
6.6	Donor	1.3	1×10^{18}	1×10^{19}

Both DFT calculations and measurements indicate that real devices have indeed such electronic defect states.

Duan et al. have identified the defect energy distribution which reveals a deep defect state 0.16 eV above the valence band in the $MAPbI_3$ perovskite using admittance spectroscopy [115]. Similarly, Xue et al. found hole traps using admittance spectroscopy in the energy range 0.16-0.23 eV with a relatively large $N_t = 10^{15} - 10^{16}$ cm^{-3} and a hole carrier capture cross-section $\sigma_p = 10^{-15} - 10^{-16}$ cm^2 s^{-1} [116]. These defects were identified as interface-type defects. Measurements done by Heo et al. revealed defects with an activation energy of 0.27-0.28 eV and defect density of 10^{17} cm^{-3}, slightly deeper than the aforementioned results [117].

Shao et al. found even higher activation energies (0.35-0.40 eV). Their PL measurements clearly verified that the majority of defect states are close to the surface of the $MAPbI_3$ films and that they are most likely electron defects. Moreover, they were only able to passivate these defects by the diffusion of PCBM into the perovskite using thermal annealing. This is in good agreement with our model that defects are not strictly localised at the interface, but that instead the defect density gradually decreases away from the interface.

6.5.1. Origin of defect states

The defect states are possibly attributed to iodine interstitials (often abbreviated as I_i). According to density-functional theory (DFT) calculations an acceptor-like defect with $E_\mathrm{T} = 0.18\,\mathrm{eV}$ above the valence band edge is introduced by such defects [122]. The iodine interstitial is the only one among the native defects (i.e. vacancies, interstitials, and antisites) causing a low-energy defect state. DFT analysis of surface defects also showed that only I_i has a deep carrier-trapping state [123]. The results are also confirmed in another theoretical study, where a defect energy of 0.15 eV above the valence band was found [124].

6.5.2. Donor-like defects near HTL

Based on the analysis in chapter 5, we know that hysteresis can be caused by donor-like defects near the HTL as well. Figure 6.6 shows HI as a function of the average defect energy $E_{\mathrm{t},0}$, but this time for a PSC with donor-like defects. Here, we assumed higher defect densities near the HTL ($N_{\mathrm{t,HTL}} = 10^{19}\,\mathrm{cm}^{-3}$). The corresponding model parameters are summarised in Table 6.2. Hysteresis is most apparent for $E_{\mathrm{t},0} = 1.26\,\mathrm{eV}$. This is in accordance with our earlier analysis in chapter 5 indicating that donor-like defects causing anomalous hysteresis have energies close to $E_{\mathrm{F},n}$. Also note that HI is higher for PSCs with defects near the HTL (the maximum values are 0.17 in Figure 6.5 and 0.41 in Figure 6.6).

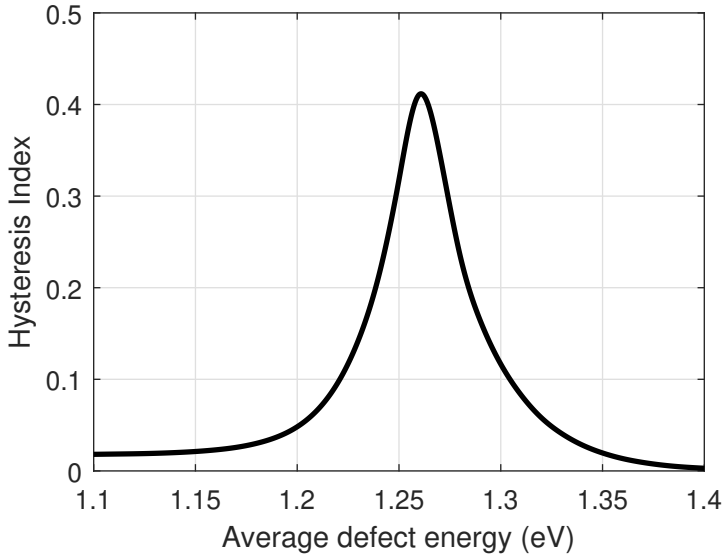

Figure 6.6: Hysteresis Index as a function of average defect energy $E_{\mathrm{t},0}$ for a device with donor-like defects near the HTL.

6.6. Impedance spectra

To study the behaviour in the frequency domain, impedance spectra are calculated from a small-signal AC analysis [114]. The response of the device to small sinusoidal signals superimposed on a DC bias is computed as a function of frequency. The results are shown in Figure 6.7. For comparison we incuded the impedance spectroscopy results from Neukom et al. in Figure 6.8 [27].

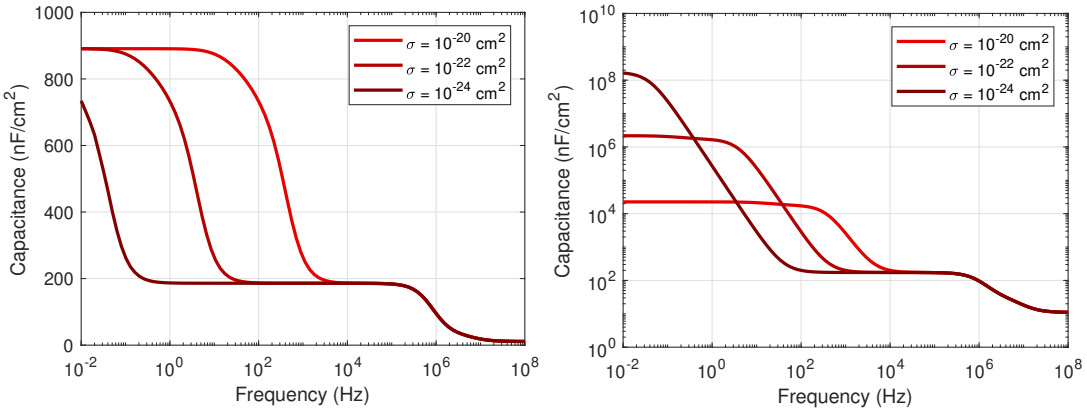

(a) Under dark conditions for different capture cross-sections.

(b) Under illumination for different capture cross-sections.

Figure 6.7: Simulation results of impedance spectra (a) in the dark and (b) under illumination.

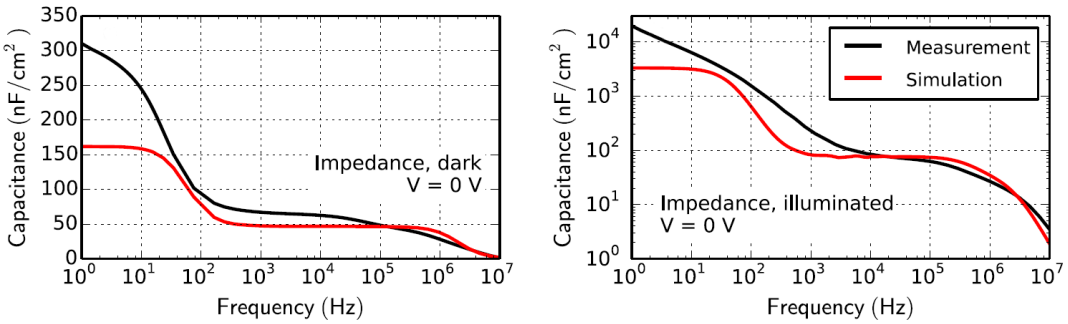

(a) In dark conditions.

(b) Under illumination.

Figure 6.8: Impedance spectra (a) in the dark and (b) under illumination (measured and simulated by Neukom et al.). Adapted from Neukom et al. [27]. Copyright 2019 American Chemical Society.

Figure 6.7a shows the capacitance as a function of frequency under dark conditions. The simulations reproduce the trends of rising capacitance at low frequencies that is also observed by Neukom et al. [27]. The transition frequency depends strongly on the capture cross-sections. We varied the capture cross-sections and observed a clear shift of the transition frequency to higher frequencies with increasing cross-sections. Varying the defect density has a similar effect. Higher defect densities shift the transition frequency to higher frequencies. In addition we observe that the capacitance reaches higher values if the defect density is increased.

Under illumination a dramatic enhancement of the capacitance is observed for low frequencies. This is again consistent with reported results in literature [27, 125]. Based on the timescales, it is likely a manifestation of the *J-V* hysteresis. In this context the term 'capacitance' is actually a bit misleading. Capacitance is normally associated with charge-storage, but Jacobs et al. showed that the giant response can be associated with the quasi-steady-state recombination current of electrons and holes [87]. In our model the oscillating voltage drives the filling and subsequent emptying of defects. When defects are filled, carrier injection to the ETL is suppressed. And when the defects are empty, injection is enhanced. As a consequence of suppressed injection, a larger recombination-induced current flows through the contacts. Because of the delayed carrier (de)trapping, the charge accumulation is out-of-phase with the voltage modulation and a high conductance is observed. The higher capacitance under illumination can thus be understood as a consequence of higher recombination rates.

7 Discussion

There is still debate about the origin of hysteresis in the current-voltage curve. In previous chapters we already discussed the most important explanations (chapter 2) and the governing physical processes (chapter 4 and 5). Here, we provide a broader discussion about the limitations of our model, the origin of hysteresis and strategies for device improvements.

7.1. Model limitations

In this section, we discuss the model limitations.

- The interfaces layers are sharp/flat and layers are homogeneous.
  Our results show that the interfaces play a key role in the device and adding surface roughness to the model could be a valuable improvement.
- The model neglects ion migration.
  So far, the physics of ion migration is not completely understood, but experimental evidence shows that the local ion concentration is dependent on the applied bias. This could affect material properties and the defect densities.
  On the other hand, so far additional models for ion diffusion have not provided a improved picture of hysteretic behaviour compared to our model based on consistent semiconductor theory.
- The spatial distribution of defects (figure 3.4) is modeled using an exponential distribution near the interface. Real distributions show more complex profiles (see figure 2.6 and Ni et al. [70]). The densities depend on the type of charge-transport layers connecting the perovskite [29, 70], but there is a lack of information about how exactly.
  Moreover, the charge-transport materials, TiO_2 and spiro-OMeTAD, contain defect states [115] as well. In our model, the ETL and HTL are assumed to be free of defects. Modeling efforts by Almosni et al., however, show that such defects could also induce hysteresis [97].
- We use the same, relatively low capture cross-sections for all defects (see also section 7.2). Moreover, all defects have the same capture cross-sections for electrons and holes. In chapter 6 we briefly discussed the effect of different capture cross-sections for electrons and holes.

This thesis can be used as a foundation for further research, in which the limitations can be addressed to reveal more insights about the governing physics.

7.2. Defect states in perovskites

There is still a lot to elucidate about the defect states in perovskite materials. There is ambiguity in whether defect states are electron or hole traps [68]. Also capture cross-sections reported by different laboratories often do not agree, if reported at all. For instance, reported values for the capture cross-sections vary from $10^{-21}\,\mathrm{cm}^{-3}$ to $10^{-15}\,\mathrm{cm}^{-3}$ [60, 62, 116, 126]. The main problem is that there are very few reliable techniques for the determination of the capture cross-section of defects. Measuring very slow defects would demand advanced characterization techniques.

The reported capture cross-sections are lower than we have used in this work. We speculate that this is caused defect metastability (see Grasser [127]). Metastable defects can occur in more than one configuration, so the process of trapping could consist of a fast transition followed by a very slow transition.

7.3. Strategies for device improvement

In this section, we discuss possible strategies for device improvements. Some are already used in high-efficiency perovskite solar cells [128].

- Interface passivation can be used to reduce defect density near the interfaces. It is usually applied to reduce SRH recombination. The inclusion of passivating layers is a universal method to improve device performance and stability and a wide variety of materials is reported to be effective as passivator in PSCs [74, 129]. For example fullerene is frequently used to passivate the ETL/perovskite interface and can reduce the number of defects by two orders of magnitude [121]. It is also observed that the hysteresis can be eliminated by surface passivation [130]. Shao et al. and Wojciechowski et al. showed that fullerene passivation eliminates hysteresis by defect passivation at the ETL/perovskite interface [121, 131].
  Next to this, physical passivation can be applied in perovskite-based solar cells to isolate certain functional layers from the outside environment to avoid material degradation [130].

- The carrier selective contacts (ETL and HTL) have a large effect on the current-voltage hysteresis. Utilization of alternative transport layers leads to different magnitudes and timescale of observed hysteresis [44]. This suggests that surface defect states play a key role in the origin of hysteresis, which is also in line with our results from chapter 6 that reducing defect densities eliminates hysteresis. Likewise, Li-treatment of mesoscopic TiO_2 electron transport layer can greatly reduce hysteresis [132]. Heo et al. attributed this to improved charge separation and injection from the perovskite into the ETL, but also noted that it might be further reduced by the reduction of surface defects.

- Addition of potassium iodide or 2-aminoethanesulfonamide hydro-chloride (ASCl) in the perovskite were also found to reduce hysteresis [28, 133]. In both cases the bulk and interfacial defect densities are significantly reduced. The potassium ion is able to prevent the formation of Frenkel defect. Addition of ASCl results in better morphology and improved crystallization.

The PSC based on the material and device parameters in Table 3.2 in chapter 3 has an open circuit voltage $V_{\mathrm{OC}} = 1.01\,\mathrm{V}$, short circuit current $J_{\mathrm{SC}} = 11.4\,\mathrm{A\,cm}^{-2}$ and FF $= 0.58$. Removing all defects yields a significant increase in J_{SC} ($18.8\,\mathrm{A\,cm}^{-2}$) and FF (0.67), whereas V_{OC} remains approximately the same (1.03 V). This shows that reduction of defect densities, for example by the above-mentioned strategies, is important for the development of high-efficiency cells.

If, in addition, we increase the perovskite bandgap to $E_{\mathrm{G}} = 1.6\,\mathrm{eV}$, we observe an improvement of V_{OC} (1.25 V) and FF (0.71), whereas J_{SC} ($18.6\,\mathrm{A\,cm}^{-2}$) decreases only slightly. Application of different perovskite materials (or mixed compounds) with different bandgaps could thus also improve device performance.

For reference, the highest certified efficiency of thin-film PSCs is 25.2 % [128, 134]. This cell has an open circuit voltage of 1.18 V, short circuit current density of $25.1\,\mathrm{mA\,cm}^{-2}$ and FF of 0.85. Moreover, Liu et al. [48] demonstrated that open-circuit voltages exceeding 1.26 V are possible. The lower external parameters in our simulations are probably due to a non-optimized design, use of different materials and the fact that we do not use an advanced optical simulation for advanced light management schemes.

7.4. Ion migration

It is often speculated that ion migration plays a predominant role in hysteresis in PSCs [135]. Until a few years ago, all evidence and modeling efforts consistently supported this idea and simulations [27, 30, 36, 89–91]. A major objection against this hypothesis was that hysteresis can be reduced by changing the interfacial contact materials [95]. However, simulation results based on ion migration show that hysteresis depends heavily on surface recombination and the diffusion length of charge carriers [27, 136].

The measurements by Weber et al. [88] that we described in section 2.7, however, reveal a more fundamental objection against the hypothesis of ion migration. The formation and release of interfacial charges, as measured by Weber et al. cannot be explained by the simplified solid-state electrolyte model[1] alone. In such a model one would expect electrostatic double layers to form on either sides of the perovskite layer. Instead a strong potential drop at the perovskite/ETL interface and a much weaker potential drop towards the perovskite/HTL interface was observed [88]. If ionic migration is indeed responsible for hysteresis, there must be additional mechanisms like chemical binding or complexation of ions at the interfaces.

Moreover, Lee et al. observed average migration lengths no higher than 110-130 nm [36]. This means that iodide ions migrate only approximately 1/3 of the perovskite layer thickness, which suggests that ion migration cannot explain the observed results of Weber et al. [88].

So far, ion migration has been simulated using a drift-diffusion model for mobile ions [27, 30, 91, 95]. In such models a fraction of the ions is mobile and is able to move trough a homogeneous solid-state electrolyte, confined to the perovskite layer. These models have their limitations. Neukom et al. discussed for example that ion migration may be field-dependent and dispersive, and that ions migrate preferably along grain boundaries [27]. Furthermore, ion migration most probably affects other properties of the perovskite material as well. Ions are considerably larger than electrons (10^{-10} m vs. 10^{-18} m) and thus impact the crystal structure, for example through the introduction of iodine vacencies [27]. We therefore believe that a limit should be posed on the local ‘ion concentration’.

[1] So far, ion migration is usually understood and modeled as diffusion of ionic species inside the perovskite layer [27, 30, 91, 95]

8

Conclusions and outlook

We have shown that the remarkable transient behaviour of perovskite solar cells can be explained by charge carrier accumulation due to electronic defect states near the interfaces. We successfully emulated the phenomenon of hysteresis using the drift-diffusion model. Simulations of perovskite solar cells with both n-i-p and p-i-n architectures show that acceptor-like defects near the ETL/perovskite interface with

- defect energy $E_t \approx 0.25\,\text{eV}$ (with respect to VBE)
- capture cross-section $\sigma \approx 10^{-23}\,\text{cm}^2$
- density $N_t > 10^{18}\,\text{cm}^{-3}$

would cause severe hysteresis at commonly used scan rates. Such defect states are possibly attributed to iodine interstitials.

We also found that donor-like defects near the HTL/perovskite interface with defect energy $E_t \approx 0.2\,\text{eV}$ (with respect to CBE) would cause hysteresis in the J-V curve. There is, however, no convincing evidence for the existence of such defect states in perovskite materials. Further research should provide more clarity on this.

All the evidence suggests that the driving force behind current-voltage hysteresis is slow accumulation and release of charge near the perovskite interfaces. So far, this was usually attributed to ion migration in the perovskite material. In this thesis we have shown that the origin could be in interfacial defects with relatively low capture cross-sections. We were able to reproduce hysteresis using realistic defect distributions in the spatial and energetic domain. The relatively low capture cross-section is probably below the limit that we can measure using current techniques. Our results support the claim that interface defects play a crucial role in the formation of hysteresis.

Further, we ruled out the that band tails are the cause of hysteretic behaviour in PSCs. Interestingly, while exploring various defects, we noticed that the work function of the perovskite material could explain why some devices show normal hysteresis and others show inverted hysteresis.

Finally, we studied how the performance of perovskite solar cells can be improved. It was found that reducing the number of defects is crucial for this. Promising strategies are interface passivation (for example by inclusion of a fullerene layer) and utilization of alternative materials for the absorber layer, ETL or HTL.

8.1. Recommendations

It stands out that we observe a clear 'S-shaped' curve in our simulated current-voltage characteristics. Our results do not show hysteresis in the open circuit voltage and the 'S-shape' does not quite match the hysteresis as observed in experiments with real devices. So far, it is not yet understood why. A study of the devices at very high applied biases might reveal more insights. Also calibration with real devices could be fruitful to achieve a closer match between simulations and experiments.

For future device improvements it is essential to reveal the nature of these defect states. So far, DFT calculations performed on perovskites were only for $MAPbI_3$. In order to obtain a broader understanding of perovskites it would be of value to reproduce experimental and computational work for other perovskite compounds as well. Experimentally identifying defects and understanding their properties requires a range of advanced complementary techniques [68]. Recently, important steps have been taken towards a more detailed spatial and energetic profiling of traps states [70]. Still there opportunities for research in the area of understanding properties of defect states in metal halide perovskites.

Further research is also needed to investigate the effect of ion migration on defect states in the bandgap. Ion migration could enhance the observed hysteresis and it would be interesting to study the combined effect with slow carrier trapping near the interfaces.

A

Derivation of the relation between capture and emission rates

Let N_t be the number of trapping centers per unit volume, $c_n(E)$ the average probability per unit time that an electron in the range $\mathrm{d}E$ is captured by an empty trap, $e_n(E)(E)$ the average probability per unit time that an electron is emitted to an empty state in the range $\mathrm{d}E$ by an occupied trap and $N(E)$ the density of states function. For the sake of completeness, we repeat that the Fermi-Dirac distribution function $f(E)$ is defined as:

$$f(E) = \frac{1}{1 + \exp\left(\frac{E - E_\mathrm{F}}{kT}\right)} \tag{A.1}$$

The electron occupation of a trap is denoted by f_t, which is a number between 0 and 1. It is the probability that the trap is occupied by an electron. So $(1 - f_\mathrm{t})N_t$ is the total number of empty traps and $f(E)N(E)\,\mathrm{d}E$ is the number of electrons in the energy range $\mathrm{d}E$. Evidently the rate of capturing electrons from the energy range $\mathrm{d}E$ is

$$(1 - f_\mathrm{t})N_t c_n(E) f(E) N(E)\,\mathrm{d}E \tag{A.2}$$

Similarly, the rate of emitting electrons to the energy range $\mathrm{d}E$ is

$$f_\mathrm{t} N_t e_n(E)(1 - f(E))N(E)\,\mathrm{d}E \tag{A.3}$$

If only this process would be effective, these rates must be equal in the stationary state. It follows that

$$(1 - f_\mathrm{t})N_t c_n(E) f(E) N(E)\,\mathrm{d}E = f_\mathrm{t} N_t e_n(E)(1 - f(E))N(E)\,\mathrm{d}E \tag{A.4}$$

and therefore

$$\frac{e_n(E)}{c_n(E)} = \frac{1 - f_\mathrm{t}}{f_\mathrm{t}} \frac{f(E)}{1 - f(E)} = \exp\left(\frac{E_\mathrm{trap} - E}{kT}\right) \tag{A.5}$$

where we used that

$$1 - f(E) = 1 - \frac{1}{1 + \exp\left(\frac{E - E_\mathrm{F}}{kT}\right)} = \frac{\exp\left(\frac{E - E_\mathrm{F}}{kT}\right)}{1 + \exp\left(\frac{E - E_\mathrm{F}}{kT}\right)} = \exp\left(\frac{E - E_\mathrm{F}}{kT}\right) f(E) \tag{A.6}$$

Because $e_n(E)$ and $c_n(E)$ are assumed to be constant, equation (A.5) also holds in non-equilibrium conditions. In the remainder we will only consider capture of electrons from the conduction band. An expressions for capture of electrons from the valence band can be derived analogously.
Note that in non-equilibrium we have to consider the quasi-Fermi level $E_{\mathrm{F},n}$ instead of E_F and $f(E)$ becomes

$$f(E) = \frac{1}{1 + \exp\left(\frac{E - E_{\mathrm{F},n}}{kT}\right)} \tag{A.7}$$

The total rate of capture c_{C}^{n} for an empty trap from the conduction band is:

$$c_{\mathrm{C}}^{n} = \int_{E_{\mathrm{C}}}^{\infty} c_n(E) f(E) N(E)\,\mathrm{d}E \tag{A.8}$$

Similarly, the total rate of emission to the conduction band for a full trap is obtained by invoking equation (A.5):

$$e_{\mathrm{C}}^{n} = \int_{E_{\mathrm{C}}}^{\infty} \exp\left(\frac{E_{\mathrm{trap}} - E}{kT}\right) c_n(E)(1 - f(E))N(E)\,\mathrm{d}E \tag{A.9}$$

$$= \exp\left(\frac{E_{\mathrm{trap}}}{kT}\right) \int_{E_{\mathrm{C}}}^{\infty} \exp\left(\frac{-E}{kT}\right) c_n(E)(1 - f(E))N(E)\,\mathrm{d}E \tag{A.10}$$

$$= \exp\left(\frac{E_{\mathrm{trap}} - E_{\mathrm{F},n}}{kT}\right) \int_{E_{\mathrm{C}}}^{\infty} c_n(E) f(E) N(E)\,\mathrm{d}E \tag{A.11}$$

where we used equation (A.6) again (with E_{F} replaced by $E_{\mathrm{F},n}$). Combining equation (A.8) and (A.11), we finally find

$$\frac{e_{\mathrm{C}}^{n}}{c_{\mathrm{C}}^{n}} = \exp\left(\frac{E_{\mathrm{trap}} - E_{\mathrm{F},n}}{kT}\right) \tag{A.12}$$

Analogously, we have for capture of electrons from the valence band:

$$\frac{e_{\mathrm{V}}^{n}}{c_{\mathrm{V}}^{n}} = \exp\left(\frac{E_{\mathrm{trap}} - E_{\mathrm{F},p}}{kT}\right) \tag{A.13}$$

B

Charge polarization at the HTL interface

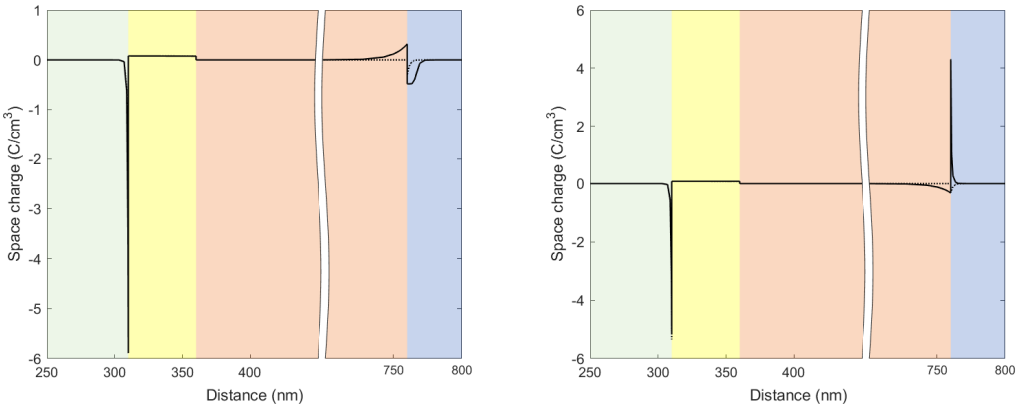

(a) Positive trapped charge.

(b) Negative trapped charge.

Figure B.1: Distribution of space charge when (a) positive charge is trapped in the perovskite layer close to the HTL or (b) negative charge is trapped in the perovskite layer close to the HTL. For comparison, the space charge distribution without trapped charge is indicated with a dashed line.

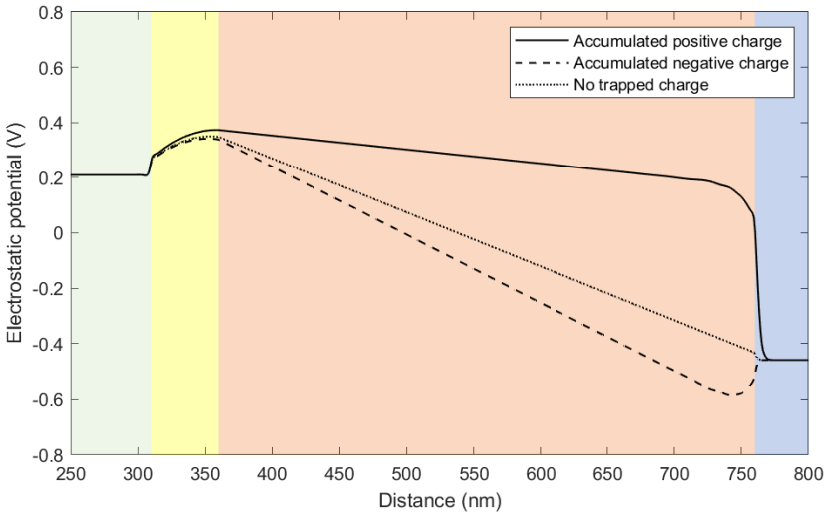

Figure B.2: Electrostatic potential inside the device in thermal equilibrium when positive, negative or no charge is trapped in the perovskite layer (red) close to the HTL (blue). The corresponding space charge distributions are shown in figure B.1.

C

Device plots during scans

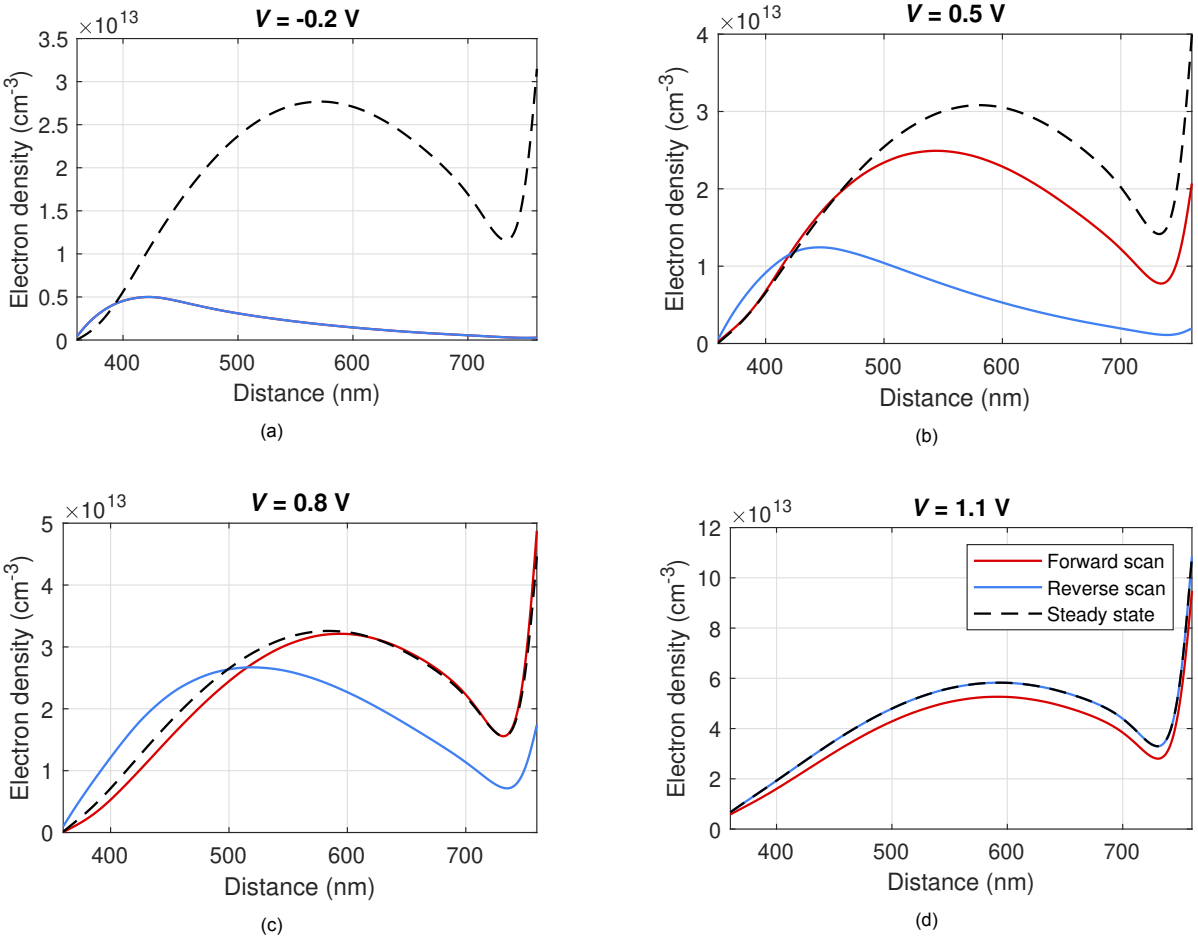

Figure C.1: Profiles of the electron density in the perovskite layer as a function of position. The ETL/perovskite interface is at the left side and the HTL/perovskite interface is at the right side. The red and blue lines denote the profiles during forward and reverse scan respectively. The steady state profile is indicated with a dashed line.

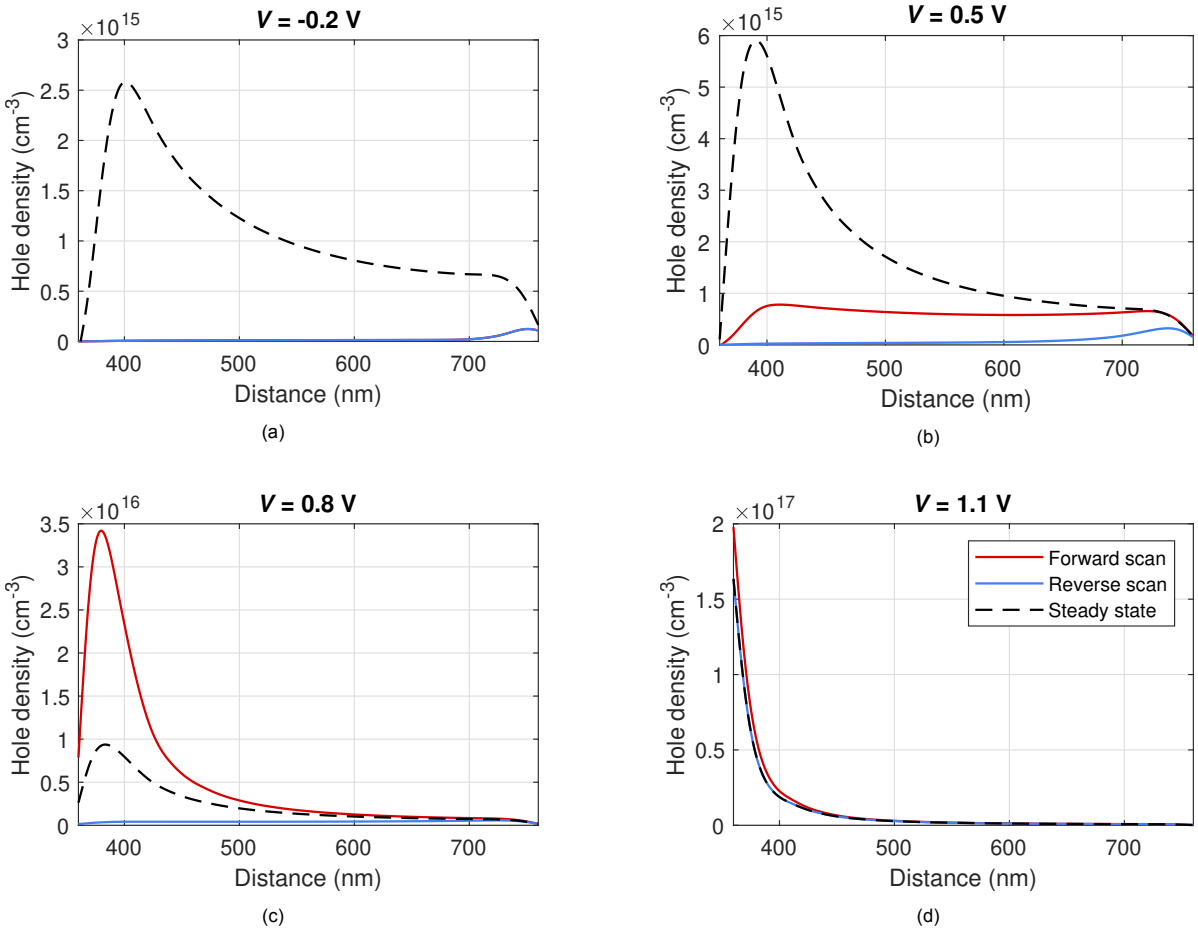

Figure C.2: Profiles of the hole density in the perovskite layer as a function of position. The ETL/perovskite interface is at the left side and the HTL/perovskite interface is at the right side. The red and blue lines denote the profiles during forward and reverse scan respectively. The steady state profile is indicated with a dashed line.

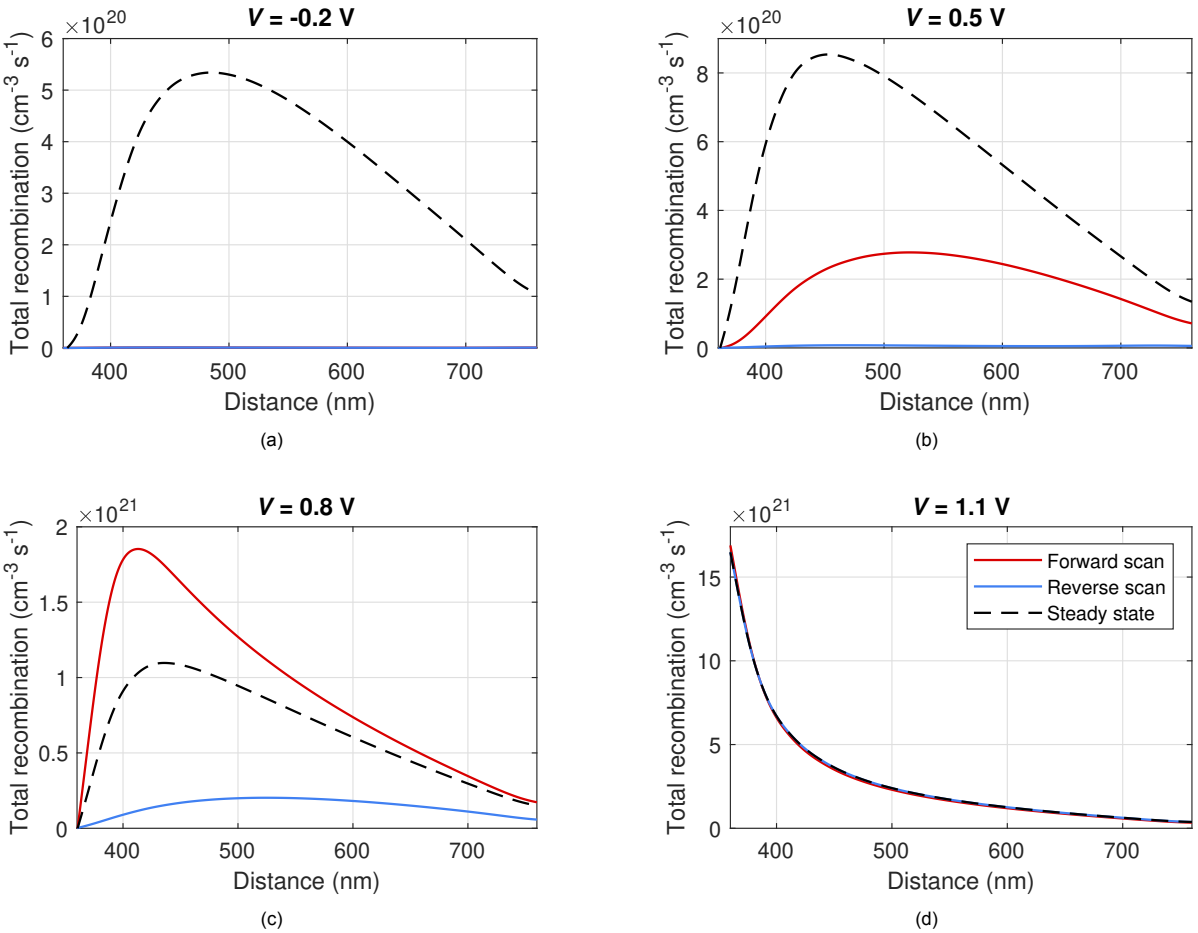

Figure C.3: Profiles of the total recombination in the perovskite layer as a function of position. The ETL/perovskite interface is at the left side and the HTL/perovskite interface is at the right side. The red and blue lines denote the profiles during forward and reverse scan respectively. The steady state profile is indicated with a dashed line.

D

Simulation parameters of p-i-n PSC

Table D.1: Material and device parameters of the inverted PSC. ϵ_r is the relative permittivity, E_G is the bandgap energy, χ is the electron affinity, N_C is the effective density of states of the conduction band, N_V is the effective density of states of the valence band, N_D the concentration of ionized donors, N_A is the concentration of ionized acceptors, μ_n is the electron mobility and μ_p is the hole mobility. Based on Neukom et al. [27].

	ITO	TaTm	$CH_3NH_3PbI_3$	C_{60}
Thickness (nm)	200	50	500	50
ε_r	3.5	3	30	3.9
E_G (eV)	3.1	1.79	1.62	1.92
χ (eV)	4.7	3.59	3.82	3.85
N_C (cm^{-3})	4.12×10^{18}	1×10^{21}	2×10^{18}	1×10^{21}
N_V (cm^{-3})	1.7×10^{19}	1×10^{21}	2×10^{19}	1×10^{21}
N_D (cm^{-3})	1×10^{20}	0	0	1.5×10^{18}
N_A (cm^{-3})	0	7×10^{18}	0	0
μ_n ($cm^2\,V^{-1}\,s^{-1}$)	160	1.5×10^{-3}	0.7	8.9×10^{-4}
μ_p ($cm^2\,V^{-1}\,s^{-1}$)	40	1.5×10^{-3}	0.4	8.9×10^{-4}

Bibliography

[1] Martin A Green, Anita Ho-Baillie, and Henry J Snaith. The emergence of perovskite solar cells. *Nature photonics*, 8(7):506, 2014.

[2] Patrick Tonui, Saheed O Oseni, Gaurav Sharma, Qingfenq Yan, and Genene Tessema Mola. Perovskites photovoltaic solar cells: An overview of current status. *Renewable and Sustainable Energy Reviews*, 91:1025–1044, 2018.

[3] Shuxia Tao, Ines Schmidt, Geert Brocks, Junke Jiang, Ionut Tranca, Klaus Meerholz, and Selina Olthof. Absolute energy level positions in tin-and lead-based halide perovskites. *Nature communications*, 10(1):1–10, 2019.

[4] NREL. Best research-cell efficiency chart, 2019.

[5] Nature Energy. Perovskites take steps to industrialization. *Nature Energy*, 5(1), 2020. doi:10.1038/s41560-020-0552-6.

[6] Arno HM Smets, Klaus Jäger, Olindo Isabella, René ACMM Swaaij, and Miro Zeman. *Solar Energy: The physics and engineering of photovoltaic conversion, technologies and systems*. UIT Cambridge, 2015.

[7] Albert Einstein. Über einen die erzeugung und verwandlung des lichtes betreffenden heuristischen gesichtspunkt. *Annalen der physik*, 322(6):132–148, 1905.

[8] Jan Czochralski. Ein neues verfahren zur messung der kristallisationsgeschwindigkeit der metalle. *Zeitschrift für physikalische Chemie*, 92(1):219–221, 1918.

[9] Daryl M Chapin, CS Fuller, and GL Pearson. A new silicon p-n junction photocell for converting solar radiation into electrical power. *Journal of Applied Physics*, 25(5):676–677, 1954.

[10] JC Arnett, LA Schaffer, JP Rumberg, and REL Tolbert. Design, installation and performance of the arco solar one-megawatt power plant. *pvse*, pages 314–320, 1984.

[11] Michael Grätzel. Dye-sensitized solar cells. *Journal of photochemistry and photobiology C: Photochemistry Reviews*, 4(2):145–153, 2003.

[12] Fraunhofer ISE. Photovoltaics report, 2020. URL `https://www.ise.fraunhofer.de/content/dam/ise/de/documents/publications/studies/Photovoltaics-Report.pdf`.

[13] Richard M Swanson. A vision for crystalline silicon photovoltaics. *Progress in photovoltaics: Research and Applications*, 14(5):443–453, 2006.

[14] George Alexandru Nemnes, Cristina Besleaga, Andrei Gabriel Tomulescu, Alexandra Palici, Lucian Pintilie, Andrei Manolescu, and Ioana Pintilie. How measurement protocols influence the dynamic jv characteristics of perovskite solar cells: Theory and experiment. *Solar Energy*, 173: 976–983, 2018.

[15] Sven Rühle. Tabulated values of the shockley–queisser limit for single junction solar cells. *Solar Energy*, 130:139–147, 2016.

[16] William Shockley and Hans J Queisser. Detailed balance limit of efficiency of p-n junction solar cells. *Journal of applied physics*, 32(3):510–519, 1961.

[17] IEA. World energy outlook 2019, 2019. URL `https://www.iea.org/reports/world-energy-outlook-2019`.

[18] IEA. Renewables 2019, 2019. URL https://www.iea.org/reports/renewables-2019.

[19] Shahriar Shafiee and Erkan Topal. When will fossil fuel reserves be diminished? *Energy policy*, 37(1):181–189, 2009.

[20] John Cook, Naomi Oreskes, Peter T Doran, William RL Anderegg, Bart Verheggen, Ed W Maibach, J Stuart Carlton, Stephan Lewandowsky, Andrew G Skuce, Sarah A Green, et al. Consensus on consensus: a synthesis of consensus estimates on human-caused global warming. *Environmental Research Letters*, 11(4):048002, 2016.

[21] Department of Economic United Nations and Population Division Social Affairs. World population prospects 2019: Highlights, 2019.

[22] Akihiro Kojima, Kenjiro Teshima, Yasuo Shirai, and Tsutomu Miyasaka. Novel photoelectrochemical cell with mesoscopic electrodes sensitized by lead-halide compounds (2). In *Proc. 210th ECS Meeting*, page 1, 2006.

[23] Akihiro Kojima, Kenjiro Teshima, Yasuo Shirai, and Tsutomu Miyasaka. Organometal halide perovskites as visible-light sensitizers for photovoltaic cells. *Journal of the American Chemical Society*, 131(17):6050–6051, 2009.

[24] Thibault Lemercier, Lara Perrin, Emilie Planès, Solenn Berson, and Lionel Flandin. A comparison of the structure and properties of opaque and semi-transparent nip/pin-type scalable perovskite solar cells. *Energies*, 13(15):3794, 2020.

[25] Donald A Neamen. *Semiconductor physics and devices: basic principles*. New York, NY: McGraw-Hill„ 2012.

[26] Simon M Sze and Kwok K Ng. *Physics of semiconductor devices*. John wiley & sons, 2006.

[27] Martin T Neukom, Andreas Schiller, Simon Züfle, Evelyne Knapp, Jorge Ávila, Daniel Pérez-del Rey, Chris Dreessen, Kassio Zanoni, Michele Sessolo, Henk J Bolink, et al. Consistent device simulation model describing perovskite solar cells in steady-state, transient and frequency domain. *ACS applied materials & interfaces*, 2019.

[28] Bo Chen, Mengjin Yang, Shashank Priya, and Kai Zhu. Origin of j–v hysteresis in perovskite solar cells. *The journal of physical chemistry letters*, 7(5):905–917, 2016.

[29] Henry J Snaith, Antonio Abate, James M Ball, Giles E Eperon, Tomas Leijtens, Nakita K Noel, Samuel D Stranks, Jacob Tse-Wei Wang, Konrad Wojciechowski, and Wei Zhang. Anomalous hysteresis in perovskite solar cells. *J. Phys. Chem. Lett*, 5(9):1511–1515, 2014.

[30] Daniel Walter, Andreas Fell, Yiliang Wu, The Duong, Chog Barugkin, Nandi Wu, Thomas White, and Klaus Weber. Transient photovoltage in perovskite solar cells: Interaction of trap-mediated recombination and migration of multiple ionic species. *The Journal of Physical Chemistry C*, 122 (21):11270–11281, 2018.

[31] Wei Chen, Xingtian Yin, Meidan Que, Haixia Xie, Jie Liu, Chenhui Yang, Yuxiao Guo, Yutao Wu, and Wenxiu Que. A comparative study of planar and mesoporous perovskite solar cells with printable carbon electrodes. *Journal of Power Sources*, 412:118–124, 2019.

[32] Taofeeq Ibn-Mohammed, SCL Koh, IM Reaney, Adolf Acquaye, G Schileo, KB Mustapha, and Rick Greenough. Perovskite solar cells: An integrated hybrid lifecycle assessment and review in comparison with other photovoltaic technologies. *Renewable and Sustainable Energy Reviews*, 80:1321–1344, 2017.

[33] Saida Laalioui, Kawtar Belrhiti Alaoui, Houda Ait Dads, Kassem El Assali, Badr Ikken, and Abdelkader Outzourhit. Progress in perovskite based solar cells: scientific and engineering state of the art. *REVIEWS ON ADVANCED MATERIALS SCIENCE*, 59(1):10–25, 2020.

[34] Taame Abraha Berhe, Wei-Nien Su, Ching-Hsiang Chen, Chun-Jern Pan, Ju-Hsiang Cheng, Hung-Ming Chen, Meng-Che Tsai, Liang-Yih Chen, Amare Aregahegn Dubale, and Bing-Joe Hwang. Organometal halide perovskite solar cells: degradation and stability. *Energy & Environmental Science*, 9(2):323–356, 2016.

[35] David P McMeekin, Golnaz Sadoughi, Waqaas Rehman, Giles E Eperon, Michael Saliba, Maximilian T Hörantner, Amir Haghighirad, Nobuya Sakai, Lars Korte, Bernd Rech, et al. A mixed-cation lead mixed-halide perovskite absorber for tandem solar cells. *Science*, 351(6269):151–155, 2016.

[36] Heejae Lee, Sofia Gaiaschi, Patrick Chapon, Arthur Marronnier, Heeryung Lee, Jean-Charles Vanel, Denis Tondelier, Jean-Eric Bourée, Yvan Bonnassieux, and Bernard Geffroy. Direct experimental evidence of halide ionic migration under bias in ch3nh3pbi3–x cl x-based perovskite solar cells using gd-oes analysis. *ACS Energy Letters*, 2(4):943–949, 2017.

[37] Giulia Grancini, C Roldán-Carmona, Iwan Zimmermann, E Mosconi, X Lee, D Martineau, S Narbey, Frédéric Oswald, F De Angelis, Michael Graetzel, et al. One-year stable perovskite solar cells by 2d/3d interface engineering. *Nature communications*, 8(1):1–8, 2017.

[38] Sai Ma, Yang Bai, Hao Wang, Huachao Zai, Jiafeng Wu, Liang Li, Sisi Xiang, Na Liu, Lang Liu, Cheng Zhu, et al. 1000 h operational lifetime perovskite solar cells by ambient melting encapsulation. *Advanced Energy Materials*, 10(9):1902472, 2020.

[39] Jian Gong, Seth B Darling, and Fengqi You. Perovskite photovoltaics: life-cycle assessment of energy and environmental impacts. *Energy & Environmental Science*, 8(7):1953–1968, 2015.

[40] Seon Joo Lee, Seong Sik Shin, Young Chan Kim, Dasom Kim, Tae Kyu Ahn, Jun Hong Noh, Jangwon Seo, and Sang Il Seok. Fabrication of efficient formamidinium tin iodide perovskite solar cells through snf2–pyrazine complex. *Journal of the American Chemical Society*, 138(12): 3974–3977, 2016.

[41] Aslihan Babayigit, Dinh Duy Thanh, Anitha Ethirajan, Jean Manca, Marc Muller, Hans-Gerd Boyen, and Bert Conings. Assessing the toxicity of pb-and sn-based perovskite solar cells in model organism danio rerio. *Scientific reports*, 6(1):1–11, 2016.

[42] Aslihan Babayigit, Anitha Ethirajan, Marc Muller, and Bert Conings. Toxicity of organometal halide perovskite solar cells. *Nature materials*, 15(3):247, 2016.

[43] Naveen Kumar Elumalai and Ashraf Uddin. Hysteresis in organic-inorganic hybrid perovskite solar cells. *Solar Energy Materials and Solar Cells*, 157:476–509, 2016.

[44] Eva Lisa Unger, Eric T Hoke, Colin D Bailie, William H Nguyen, Andrea Ruth Bowring, T Heumüller, Mark Greyson Christoforo, and Michael D McGehee. Hysteresis and transient behavior in current–voltage measurements of hybrid-perovskite absorber solar cells. *Energy & Environmental Science*, 7(11):3690–3698, 2014.

[45] Wolfgang Tress, Nevena Marinova, Thomas Moehl, Shaik Mohammad Zakeeruddin, Mohammad Khaja Nazeeruddin, and Michael Grätzel. Understanding the rate-dependent j-v hysteresis, slow time component, and aging in ch3nh3pbi3 perovskite solar cells: the role of a compensated electric field. *Energy & Environmental Science*, 8(3):995–1004, 2015.

[46] Pietro P Altermatt. Models for numerical device simulations of crystalline silicon solar cells—a review. *Journal of computational electronics*, 10(3):314, 2011.

[47] Man Yue, Jie Su, Peng Zhao, Zhenhua Lin, Jincheng Zhang, Jingjing Chang, and Yue Hao. Optimizing the performance of cspbi 3-based perovskite solar cells via doping a zno electron transport layer coupled with interface engineering. *Nano-Micro Letters*, 11(1):91, 2019.

[48] Zhifa Liu, Lisa Krückemeier, Benedikt Krogmeier, Benjamin Klingebiel, José A Márquez, Sergiu Levcenko, Senol Öz, Sanjay Mathur, Uwe Rau, Thomas Unold, et al. Open-circuit voltages exceeding 1.26 v in planar methylammonium lead iodide perovskite solar cells. *ACS Energy Letters*, 4(1):110–117, 2018.

[49] Tao Wang, Peng Wang, Kun Ding, and Qi Liang. Numerical simulation of carrier transporting layer free planar perovskite cells. *Optik*, 179:1019–1026, 2019.

[50] W Van Roosbroeck. Theory of the flow of electrons and holes in germanium and other semiconductors. *The Bell System Technical Journal*, 29(4):560–607, 1950.

[51] Daniel Abou-Ras, Thomas Kirchartz, and Uwe Rau. *Advanced characterization techniques for thin film solar cells*. John Wiley & Sons, 2016.

[52] WTRW Shockley and WT Read Jr. Statistics of the recombinations of holes and electrons. *Physical review*, 87(5):835, 1952.

[53] Valerio Sarritzu, Nicola Sestu, Daniela Marongiu, Xueqing Chang, Qingqian Wang, Sofia Masi, Silvia Colella, Aurora Rizzo, Agnieszka Gocalinska, Emanuele Pelucchi, et al. Direct or indirect bandgap in hybrid lead halide perovskites? *Advanced Optical Materials*, 6(10):1701254, 2018.

[54] Andreas Paulke, Samuel D Stranks, Juliane Kniepert, Jona Kurpiers, Christian M Wolff, Natalie Schön, Henry J Snaith, Thomas JK Brenner, and Dieter Neher. Charge carrier recombination dynamics in perovskite and polymer solar cells. *Applied Physics Letters*, 108(11):113505, 2016.

[55] Xie Zhang, Jimmy-Xuan Shen, Wennie Wang, and Chris G Van de Walle. First-principles analysis of radiative recombination in lead-halide perovskites. *ACS Energy Letters*, 3(10):2329–2334, 2018.

[56] Florian Staub, Uwe Rau, and Thomas Kirchartz. Statistics of the auger recombination of electrons and holes via defect levels in the band gap—application to lead-halide perovskites. *ACS omega*, 3(7):8009–8016, 2018.

[57] Johannes M Richter, Mojtaba Abdi-Jalebi, Aditya Sadhanala, Maxim Tabachnyk, Jasmine PH Rivett, Luis M Pazos-Outón, Karl C Gödel, Michael Price, Felix Deschler, and Richard H Friend. Enhancing photoluminescence yields in lead halide perovskites by photon recycling and light out-coupling. *Nature communications*, 7(1):1–8, 2016.

[58] Jimmy-Xuan Shen, Xie Zhang, Suvadip Das, Emmanouil Kioupakis, and Chris G Van de Walle. Unexpectedly strong auger recombination in halide perovskites. *Advanced Energy Materials*, 8 (30):1801027, 2018.

[59] Giovanni Landi, Heinz Christoph Neitzert, Carlo Barone, Costantino Mauro, Felix Lang, Steve Albrecht, Bernd Rech, and Sergio Pagano. Correlation between electronic defect states distribution and device performance of perovskite solar cells. *Advanced Science*, 4(10):1700183, 2017.

[60] Artem Musiienko, Pavel Moravec, Roman Grill, Petr Praus, Igor Vasylchenko, Jakub Pekarek, Jeremy Tisdale, Katarina Ridzonova, Eduard Belas, Lucie Landová, et al. Deep levels, charge transport and mixed conductivity in organometallic halide perovskites. *Energy & Environmental Science*, 12(4):1413–1425, 2019.

[61] Sung Heo, Gabseok Seo, Yonghui Lee, Dongwook Lee, Minsu Seol, Jooho Lee, Jong-Bong Park, Kihong Kim, Dong-Jin Yun, Yong Su Kim, et al. Deep level trapped defect analysis in ch 3 nh 3 pbi 3 perovskite solar cells by deep level transient spectroscopy. *Energy & Environmental Science*, 10(5):1128–1133, 2017.

[62] John W Rosenberg, Matshisa J Legodi, Yevgeny Rakita, David Cahen, and Mmantsae Diale. Laplace current deep level transient spectroscopy measurements of defect states in methylammonium lead bromide single crystals. *Journal of Applied Physics*, 122(14):145701, 2017.

[63] Stefaan De Wolf, Jakub Holovsky, Soo-Jin Moon, Philipp Löper, Bjoern Niesen, Martin Ledinsky, Franz-Josef Haug, Jun-Ho Yum, and Christophe Ballif. Organometallic halide perovskites: sharp optical absorption edge and its relation to photovoltaic performance. *The journal of physical chemistry letters*, 5(6):1035–1039, 2014.

[64] Andreas Baumann, Stefan Väth, Philipp Rieder, Michael C Heiber, Kristofer Tvingstedt, and Vladimir Dyakonov. Identification of trap states in perovskite solar cells. *The journal of physical chemistry letters*, 6(12):2350–2354, 2015.

[65] Wan-Jian Yin, Tingting Shi, and Yanfa Yan. Unusual defect physics in ch3nh3pbi3 perovskite solar cell absorber. *Applied Physics Letters*, 104(6):063903, 2014.

[66] Dong Shi, Valerio Adinolfi, Riccardo Comin, Mingjian Yuan, Erkki Alarousu, Andrei Buin, Yin Chen, Sjoerd Hoogland, Alexander Rothenberger, Khabiboulakh Katsiev, et al. Low trap-state density and long carrier diffusion in organolead trihalide perovskite single crystals. *Science*, 347 (6221):519–522, 2015.

[67] Adam D Wright, Rebecca L Milot, Giles E Eperon, Henry J Snaith, Michael B Johnston, and Laura M Herz. Band-tail recombination in hybrid lead iodide perovskite. *Advanced Functional Materials*, 27(29):1700860, 2017.

[68] James M Ball and Annamaria Petrozza. Defects in perovskite-halides and their effects in solar cells. *Nature Energy*, 1(11):1–13, 2016.

[69] Dane W deQuilettes, Kyle Frohna, David Emin, Thomas Kirchartz, Vladimir Bulovic, David S Ginger, and Samuel D Stranks. Charge-carrier recombination in halide perovskites: Focus review. *Chemical reviews*, 119(20):11007–11019, 2019.

[70] Zhenyi Ni, Chunxiong Bao, Ye Liu, Qi Jiang, Wu-Qiang Wu, Shangshang Chen, Xuezeng Dai, Bo Chen, Barry Hartweg, Zhengshan Yu, et al. Resolving spatial and energetic distributions of trap states in metal halide perovskite solar cells. *Science*, 367(6484):1352–1358, 2020.

[71] Jennifer T Heath, J David Cohen, and William N Shafarman. Bulk and metastable defects in cuin 1- x ga x se 2 thin films using drive-level capacitance profiling. *Journal of Applied Physics*, 95 (3):1000–1010, 2004.

[72] Wan-Jian Yin, Tingting Shi, and Yanfa Yan. Unique properties of halide perovskites as possible origins of the superior solar cell performance. *Advanced Materials*, 26(27):4653–4658, 2014.

[73] Michael L Agiorgousis, Yi-Yang Sun, Hao Zeng, and Shengbai Zhang. Strong covalency-induced recombination centers in perovskite solar cell material ch3nh3pbi3. *Journal of the American Chemical Society*, 136(41):14570–14575, 2014.

[74] Pengjun Zhao, Byeong Jo Kim, and Hyun Suk Jung. Passivation in perovskite solar cells: A review. *Materials today energy*, 7:267–286, 2018.

[75] Dale J Igram. *A Topological Explanation of the Urbach Tail*. PhD thesis, Ohio University, 2016.

[76] John F Wager. Real-and reciprocal-space attributes of band tail states. *AIP Advances*, 7(12): 125321, 2017.

[77] Morrel H Cohen, M-Y Chou, EN Economou, S John, and CM Soukoulis. Band tails, path integrals, instantons, polarons, and all that. *IBM Journal of Research and Development*, 32(1):82–92, 1988.

[78] Y Pan, F Inam, M Zhang, and DA Drabold. Atomistic origin of urbach tails in amorphous silicon. *Physical review letters*, 100(20):206403, 2008.

[79] Franz Urbach. The long-wavelength edge of photographic sensitivity and of the electronic absorption of solids. *Physical Review*, 92(5):1324, 1953.

[80] Sajeev John, Costas Soukoulis, Morrel H Cohen, and EN Economou. Theory of electron band tails and the urbach optical-absorption edge. *Physical review letters*, 57(14):1777, 1986.

[81] Martin Ledinsky, Tereza Schönfeldová, Jakub Holovský, Erkan Aydin, Zdeňka Hájková, Lucie Landová, Neda Neyková, Antonín Fejfar, and Stefaan De Wolf. Temperature dependence of the urbach energy in lead iodide perovskites. *The journal of physical chemistry letters*, 10(6): 1368–1373, 2019.

[82] Aditya Sadhanala, Felix Deschler, Tudor H Thomas, Siân E Dutton, Karl C Goedel, Fabian C Hanusch, May L Lai, Ullrich Steiner, Thomas Bein, Pablo Docampo, et al. Preparation of single-phase films of ch3nh3pb (i1–x br x) 3 with sharp optical band edges. *The journal of physical chemistry letters*, 5(15):2501–2505, 2014.

[83] Yaoguang Rong, Yue Hu, Sandheep Ravishankar, Huawei Liu, Xiaomeng Hou, Yusong Sheng, Anyi Mei, Qifei Wang, Daiyu Li, Mi Xu, et al. Tunable hysteresis effect for perovskite solar cells. *Energy & Environmental Science*, 10(11):2383–2391, 2017.

[84] Giles E Eperon, Giuseppe M Paternò, Rebecca J Sutton, Andrea Zampetti, Amir Abbas Haghighirad, Franco Cacialli, and Henry J Snaith. Inorganic caesium lead iodide perovskite solar cells. *Journal of Materials Chemistry A*, 3(39):19688–19695, 2015.

[85] Hui-Seon Kim and Nam-Gyu Park. Parameters affecting i–v hysteresis of ch3nh3pbi3 perovskite solar cells: effects of perovskite crystal size and mesoporous tio2 layer. *The journal of physical chemistry letters*, 5(17):2927–2934, 2014.

[86] Amalie Dualeh, Thomas Moehl, Nicolas Tétreault, Joël Teuscher, Peng Gao, Mohammad Khaja Nazeeruddin, and Michael Grätzel. Impedance spectroscopic analysis of lead iodide perovskite-sensitized solid-state solar cells. *ACS nano*, 8(1):362–373, 2014.

[87] Daniel A Jacobs, Heping Shen, Florian Pfeffer, Jun Peng, Thomas P White, Fiona J Beck, and Kylie R Catchpole. The two faces of capacitance: new interpretations for electrical impedance measurements of perovskite solar cells and their relation to hysteresis. *Journal of Applied Physics*, 124(22):225702, 2018.

[88] Stefan AL Weber, Ilka M Hermes, Silver-Hamill Turren-Cruz, Christopher Gort, Victor W Bergmann, Laurent Gilson, Anders Hagfeldt, Michael Graetzel, Wolfgang Tress, and Rüdiger Berger. How the formation of interfacial charge causes hysteresis in perovskite solar cells. *Energy & Environmental Science*, 11(9):2404–2413, 2018.

[89] Junichiro Mizusaki, Kimiyasu Arai, and Kazuo Fueki. Ionic conduction of the perovskite-type halides. *Solid State Ionics*, 11(3):203–211, 1983.

[90] Christopher Eames, Jarvist M Frost, Piers RF Barnes, Brian C O'regan, Aron Walsh, and M Saiful Islam. Ionic transport in hybrid lead iodide perovskite solar cells. *Nature communications*, 6(1): 1–8, 2015.

[91] Stephan van Reenen, Martijn Kemerink, and Henry J Snaith. Modeling anomalous hysteresis in perovskite solar cells. *The journal of physical chemistry letters*, 6(19):3808–3814, 2015.

[92] J Beilsten-Edmands, GE Eperon, RD Johnson, HJ Snaith, and PG Radaelli. Non-ferroelectric nature of the conductance hysteresis in ch3nh3pbi3 perovskite-based photovoltaic devices. *Applied Physics Letters*, 106(17):173502, 2015.

[93] Ajay Kumar Jena, Hsin-Wei Chen, Atsushi Kogo, Yoshitaka Sanehira, Masashi Ikegami, and Tsutomu Miyasaka. The interface between fto and the tio2 compact layer can be one of the origins to hysteresis in planar heterojunction perovskite solar cells. *ACS applied materials & interfaces*, 7(18):9817–9823, 2015.

[94] Rafael S Sanchez, Victoria Gonzalez-Pedro, Jin-Wook Lee, Nam-Gyu Park, Yong Soo Kang, Ivan Mora-Sero, and Juan Bisquert. Slow dynamic processes in lead halide perovskite solar cells. characteristic times and hysteresis. *The journal of physical chemistry letters*, 5(13):2357–2363, 2014.

[95] Philip Calado, Andrew M Telford, Daniel Bryant, Xiaoe Li, Jenny Nelson, Brian C O'Regan, and Piers RF Barnes. Evidence for ion migration in hybrid perovskite solar cells with minimal hysteresis. *Nature communications*, 7(1):1–10, 2016.

[96] Jin-Wook Lee, Seul-Gi Kim, Sang-Hoon Bae, Do-Kyoung Lee, Oliver Lin, Yang Yang, and Nam-Gyu Park. The interplay between trap density and hysteresis in planar heterojunction perovskite solar cells. *Nano letters*, 17(7):4270–4276, 2017.

[97] Samy Almosni, Ludmila Cojocaru, Debin Li, Satoshi Uchida, Takaya Kubo, and Hiroshi Segawa. Tunneling-assisted trapping as one of the possible mechanisms for the origin of hysteresis in perovskite solar cells. *Energy Technology*, 5(10):1767–1774, 2017.

[98] Stephen A Campbell, H-S Kim, David C Gilmer, Boyong He, Tiezhong Ma, and Wayne L Gladfelter. Titanium dioxide (tio 2)-based gate insulators. *IBM journal of research and development*, 43(3):383–392, 1999.

[99] Albrecht Poglitsch and Daniel Weber. Dynamic disorder in methylammoniumtrihalogenoplumbates (ii) observed by millimeter-wave spectroscopy. *The Journal of chemical physics*, 87 (11):6373–6378, 1987.

[100] Dmitry Poplavskyy and Jenny Nelson. Nondispersive hole transport in amorphous films of methoxy-spirofluorene-arylamine organic compound. *Journal of Applied Physics*, 93(1):341–346, 2003.

[101] Chu-Chen Chueh, Chang-Zhi Li, and Alex K-Y Jen. Recent progress and perspective in solution-processed interfacial materials for efficient and stable polymer and organometal perovskite solar cells. *Energy & Environmental Science*, 8(4):1160–1189, 2015.

[102] Dianyi Liu and Timothy L Kelly. Perovskite solar cells with a planar heterojunction structure prepared using room-temperature solution processing techniques. *Nature photonics*, 8(2):133–138, 2014.

[103] Feng Liu, Jun Zhu, Junfeng Wei, Yi Li, Mei Lv, Shangfeng Yang, Bing Zhang, Jianxi Yao, and Songyuan Dai. Numerical simulation: toward the design of high-efficiency planar perovskite solar cells. *Applied Physics Letters*, 104(25):253508, 2014.

[104] Mingkui Wang, Carole Grätzel, Soo-Jin Moon, Robin Humphry-Baker, Nathalie Rossier-Iten, Shaik M Zakeeruddin, and Michael Grätzel. Surface design in solid-state dye sensitized solar cells: effects of zwitterionic co-adsorbents on photovoltaic performance. *Advanced Functional Materials*, 19(13):2163–2172, 2009.

[105] Meredith CK Sellers and Edmund G Seebauer. Manipulation of polycrystalline tio2 carrier concentration via electrically active native defects. *Journal of Vacuum Science & Technology A: Vacuum, Surfaces, and Films*, 29(6):061503, 2011.

[106] Jorge García-Cañadas, Francisco Fabregat-Santiago, Henk J Bolink, Emilio Palomares, Germà Garcia-Belmonte, and Juan Bisquert. Determination of electron and hole energy levels in mesoporous nanocrystalline tio2 solid-state dye solar cell. *Synthetic metals*, 156(14-15):944–948, 2006.

[107] Samuel D Stranks, Giles E Eperon, Giulia Grancini, Christopher Menelaou, Marcelo JP Alcocer, Tomas Leijtens, Laura M Herz, Annamaria Petrozza, and Henry J Snaith. Electron-hole diffusion lengths exceeding 1 micrometer in an organometal trihalide perovskite absorber. *Science*, 342 (6156):341–344, 2013.

[108] Henry J Snaith and Michael Grätzel. Enhanced charge mobility in a molecular hole transporter via addition of redox inactive ionic dopant: Implication to dye-sensitized solar cells. *Applied physics letters*, 89(26):262114, 2006.

[109] Takashi Minemoto and Masashi Murata. Device modeling of perovskite solar cells based on structural similarity with thin film inorganic semiconductor solar cells. *Journal of applied physics*, 116(5):054505, 2014.

[110] Yiliang Wu, Heping Shen, Daniel Walter, Daniel Jacobs, The Duong, Jun Peng, Liangcong Jiang, Yi-Bing Cheng, and Klaus Weber. On the origin of hysteresis in perovskite solar cells. *Advanced Functional Materials*, 26(37):6807–6813, 2016.

[111] Aaesha Alnuaimi, Ibraheem Almansouri, and Ammar Nayfeh. Effect of mobility and band structure of hole transport layer in planar heterojunction perovskite solar cells using 2d tcad simulation. *Journal of Computational Electronics*, 15(3):1110–1118, 2016.

[112] Urs Aeberhard, Martin Neukom, Andreas Schiller, Simon Zuefle, Sandra Jenatsch, Balthasar Bluelle, Stephane Altazin, Lidia Stepanova, Evelyne Knapp, Christoph Kirsch, et al. Computational device optimization and parameter extraction for perovskite-based solar cells. In *Physics, Simulation, and Photonic Engineering of Photovoltaic Devices IX*, volume 11275, page 112750B. International Society for Optics and Photonics, 2020.

[113] Laura M Herz. Charge-carrier mobilities in metal halide perovskites: fundamental mechanisms and limits. *ACS Energy Letters*, 2(7):1539–1548, 2017.

[114] Inc. Synopsys. *Sentaurus Device User Guide version K-2015.06*, 2015.

[115] Hsin-Sheng Duan, Huanping Zhou, Qi Chen, Pengyu Sun, Song Luo, Tze-Bin Song, Brion Bob, and Yang Yang. The identification and characterization of defect states in hybrid organic–inorganic perovskite photovoltaics. *Physical chemistry chemical physics*, 17(1):112–116, 2015.

[116] Juanjuan Xue, Xiaobo Hu, YiXin Guo, Guoen Weng, Jinchun Jiang, Shaoqiang Chen, Ziqiang Zhu, and Junhao Chu. Diagnosis of electrically active defects in ch 3 nh 3 pbi 3 perovskite solar cells via admittance spectroscopy measurements. *Applied Optics*, 59(2):552–557, 2020.

[117] Jin Hyuck Heo, Dae Ho Song, Hye Ji Han, Seong Yeon Kim, Jun Ho Kim, Dasom Kim, Hee Won Shin, Tae Kyu Ahn, Christoph Wolf, Tae-Woo Lee, et al. Planar ch3nh3pbi3 perovskite solar cells with constant 17.2% average power conversion efficiency irrespective of the scan rate. *Advanced materials*, 27(22):3424–3430, 2015.

[118] Antonio Abate, Michael Saliba, Derek J Hollman, Samuel D Stranks, Konrad Wojciechowski, Roberto Avolio, Giulia Grancini, Annamaria Petrozza, and Henry J Snaith. Supramolecular halogen bond passivation of organic–inorganic halide perovskite solar cells. *Nano letters*, 14(6): 3247–3254, 2014.

[119] Hsin-Wei Chen, Nobuya Sakai, Masashi Ikegami, and Tsutomu Miyasaka. Emergence of hysteresis and transient ferroelectric response in organo-lead halide perovskite solar cells. *The journal of physical chemistry letters*, 6(1):164–169, 2015.

[120] Jing Wei, Yicheng Zhao, Heng Li, Guobao Li, Jinlong Pan, Dongsheng Xu, Qing Zhao, and Dapeng Yu. Hysteresis analysis based on the ferroelectric effect in hybrid perovskite solar cells. *The journal of physical chemistry letters*, 5(21):3937–3945, 2014.

[121] Yuchuan Shao, Zhengguo Xiao, Cheng Bi, Yongbo Yuan, and Jinsong Huang. Origin and elimination of photocurrent hysteresis by fullerene passivation in ch 3 nh 3 pbi 3 planar heterojunction solar cells. *Nature communications*, 5(1):1–7, 2014.

[122] Mao Hua Du. Efficient carrier transport in halide perovskites: theoretical perspectives. *Journal of Materials Chemistry A*, 2(24):9091–9098, 2014.

[123] Hiroki Uratani and Koichi Yamashita. Charge carrier trapping at surface defects of perovskite solar cell absorbers: a first-principles study. *The journal of physical chemistry letters*, 8(4):742–746, 2017.

[124] Edoardo Mosconi, Daniele Meggiolaro, Henry J Snaith, Samuel D Stranks, and Filippo De Angelis. Light-induced annihilation of frenkel defects in organo-lead halide perovskites. *Energy & Environmental Science*, 9(10):3180–3187, 2016.

[125] Emilio J Juarez-Perez, Rafael S Sanchez, Laura Badia, Germá Garcia-Belmonte, Yong Soo Kang, Ivan Mora-Sero, and Juan Bisquert. Photoinduced giant dielectric constant in lead halide perovskite solar cells. *The journal of physical chemistry letters*, 5(13):2390–2394, 2014.

[126] Mara Bruzzi, Naomi Falsini, Nicola Calisi, and Anna Vinattieri. Electrically active defects in polycrystalline and single crystal metal halide perovskite. *Energies*, 13(7):1643, 2020.

[127] Tibor Grasser. Stochastic charge trapping in oxides: From random telegraph noise to bias temperature instabilities. *Microelectronics Reliability*, 52(1):39–70, 2012.

[128] Eui Hyuk Jung, Nam Joong Jeon, Eun Young Park, Chan Su Moon, Tae Joo Shin, Tae-Youl Yang, Jun Hong Noh, and Jangwon Seo. Efficient, stable and scalable perovskite solar cells using poly (3-hexylthiophene). *Nature*, 567(7749):511–515, 2019.

[129] Yi Yang, Cheng Liu, Yong Ding, Zulqarnain Arain, Shiqiang Wang, Xuepeng Liu, Tasawar Hayat, Ahmed Alsaedi, and Songyuan Dai. Eliminating charge accumulation via interfacial dipole for efficient and stable perovskite solar cells. *ACS applied materials & interfaces*, 11(38):34964–34972, 2019.

[130] Qi Jiang, Yang Zhao, Xingwang Zhang, Xiaolei Yang, Yong Chen, Zema Chu, Qiufeng Ye, Xingxing Li, Zhigang Yin, and Jingbi You. Surface passivation of perovskite film for efficient solar cells. *Nature Photonics*, 13(7):460–466, 2019.

[131] Konrad Wojciechowski, Samuel D Stranks, Antonio Abate, Golnaz Sadoughi, Aditya Sadhanala, Nikos Kopidakis, Garry Rumbles, Chang-Zhi Li, Richard H Friend, Alex K-Y Jen, et al. Heterojunction modification for highly efficient organic–inorganic perovskite solar cells. *ACS nano*, 8 (12):12701–12709, 2014.

[132] Jin Hyuck Heo, Myoung Sang You, Min Hyuk Chang, Wenping Yin, Tae Kyu Ahn, Sang-Ju Lee, Shi-Joon Sung, Dae Hwan Kim, and Sang Hyuk Im. Hysteresis-less mesoscopic ch3nh3pbi3 perovskite hybrid solar cells by introduction of li-treated tio2 electrode. *Nano Energy*, 15:530–539, 2015.

[133] Dae-Yong Son, Seul-Gi Kim, Ja-Young Seo, Seon-Hee Lee, Hyunjung Shin, Donghwa Lee, and Nam-Gyu Park. Universal approach toward hysteresis-free perovskite solar cell via defect engineering. *Journal of the American Chemical Society*, 140(4):1358–1364, 2018.

[134] Martin A Green, Ewan D Dunlop, Jochen Hohl-Ebinger, Masahiro Yoshita, Nikos Kopidakis, and Xiaojing Hao. Solar cell efficiency tables (version 56). *Progress in Photovoltaics: Research and Applications*, 28(7):629–638, 2020.

[135] Cheng Li, Antonio Guerrero, Yu Zhong, and Sven Huettner. Origins and mechanisms of hysteresis in organometal halide perovskites. *Journal of Physics: Condensed Matter*, 29(19):193001, 2017.

[136] Martin Thomas Neukom, Simon Züfle, Evelyne Knapp, Mohammed Makha, Roland Hany, and Beat Ruhstaller. Why perovskite solar cells with high efficiency show small iv-curve hysteresis. *Solar Energy Materials and Solar Cells*, 169:159–166, 2017.